The role of hydrodynamic forces in synchronisation and alignment of mammalian motile cilia

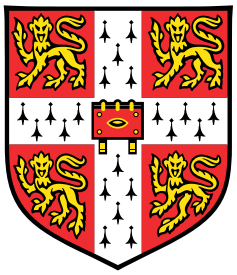

Nicola Pellicciotta

Department of Physics
University of Cambridge

This dissertation is submitted for the degree of
Doctor of Philosophy

Corpus Christi College October 2019

Declaration

This thesis is the result of my own work and includes nothing which is the outcome of work done in collaboration except as declared in the Preface and specified in the text. It is not substantially the same as any that I have submitted, or, is being concurrently submitted for a degree or diploma or other qualification at the University of Cambridge or any other University or similar institution except as declared in the Preface and specified in the text. I further state that no substantial part of my thesis has already been submitted, or, is being concurrently submitted for any such degree, diploma or other qualification at the University of Cambridge or any other University or similar institution except as declared in the Preface and specified in the text. It does not exceed the prescribed word limit for the relevant Degree Committee

Nicola Pellicciotta
October 2019

Abstract

Fluid flow generated by a ciliated epithelium is a fascinating evidence of collective behaviour in nature. In many organs and eukaryotic organisms, thousands of microscale whip-like structures called 'motile cilia' beat aligned at the same frequency and in a coordinated fashion. This dynamics, known as 'metachronal wave', has fundamental physiological roles in microorganisms and many organs of vertebrates. In the airways, the coordinated beatings of motile cilia generate a fluid flow that pushes mucus to the pharynx, and so protects the lungs from inhaled contaminants. The failure of this collective dynamics can precipitate or exacerbate severe infections and chronic inflammatory conditions such as cystic fibrosis (CF), primary ciliary dyskinesia (PCD) or asthma. In the brain, the multiciliated ependymal cells cover all the ventricles. Their cilia beat in a coordinated fashion to ensure the cerebrospinal fluid circulation necessary for brain homoeostasis, toxin washout and orientation of the migration of newborn neurons. Despite the fundamental role in nature, the mechanism underpinning such collective behaviour is still unknown.

A recent hypothesis, supported by simulations, experiments with microorganisms and with cilia models, proposed that hydrodynamic interactions between cilia could provide a physical mechanism for their coordination. In contrast, others have proposed a role of the cytoskeletal elastic coupling between cilia. While previous works mainly focused on algae and protists, investigating the conditions that are required for the emergence of the metachronal wave in mammalian tissues can provide important progress in the diagnosis and treatment of human medical diseases. Specifically, I tackled this broad topic by studying the hydrodynamic forces necessary for the synchronisation and alignment of motile cilia from brain and airways. This question was addressed experimentally by measuring cilia motility during treatment with oscillatory and constant external fluid flows. We found that synchronisation and alignment of mammalian cilia in the brain is achieved with flows of similar magnitude of the ones generated by cilia themselves. Our results suggest that hydrodynamic forces between cilia are sufficient for the emergence of their collective behaviour.

The first chapter provides basic knowledge on motile cilia structure and functions in microorganisms and humans. Additionally, I introduce the reader to the open questions related to the coordination of a pair and a carpet of cilia, with specific attention on previous works on mammals. This first chapter is followed by a description of a novel microfluidic device that I developed to grow *in vitro* airway and brain cells and apply controlled viscous forces.

In Chapter 3, I describe how we have investigated cilia synchronisation of mammalian cilia. Applying external oscillatory flow on brain cells, we studied the susceptibility of cilia motility to hydrodynamic forces similar to the ones generated by cilia themselves. We found that cells with few cilia (up to five) can be entrained at flows comparable to the cilia-driven flows reported in vivo. We suggest that hydrodynamic forces between mammalian cilia are sufficiently strong to be the mechanism underpinning frequency synchronisation.

In the second part of my thesis, I looked into the hydrodynamic shear forces needed to align permanently the cilia direction of beating. We tackled this problem by using *in vitro* cultures of mouse brain and human airway cells grown in custom flow channels. We found that cilia from mouse brain do not lock their beating direction after *ciliogenesis*, but can respond and align to physiological shear stress found *in vivo* at any time, in contrast with was previously believed. Moreover, we suggest that cilia alignment depends on the density of cilia, in agreement with a hydrodynamic screening effect of the external flow by the nearby cilia that we aim to investigate in the future. These results are described in Chapter 4. Successively in Chapter 5, I report our approach to study whether physiological shear stress can induce cilia alignment in airway cell cultures. The current hypothesis is that these cilia may also be able to align with external hydrodynamic forces - however, experimental evidence is still needed. There is a lack of experiments on this topic mainly because airway cells are cultured in an air-liquid interface, and so shear stress has to be applied with airflows. We developed novel setups for applying long term shear stress with air and fluid flow on this system, leaving further experiments for the future.

Acknowledgements

I want to acknowledge all the people who helped to realise this work. First of all, I want to thank my supervisor Pietro Cicuta, who guided me with excellent advice in the last four years. I am very happy to have an advisor who always believed in my scientific ideas and allowed me to learn so much. Many sincere thanks to all my cilia-groupmates Luigi Feriani, Evelyn Hamilton and Maurizio Chioccioli, for all the useful discussion from fluid dynamics to Matlab programming. Other special thanks to Jurij Kotar, who developed almost all the fantastic equipment that I have used and taught me so much about everything, from electronics to machining. I am very grateful to Nathalie Spassky, Marion Faucourt, Phil Barry and Frank McCaughan for the productive collaborations. Without their trust and efforts, I never would be able to accomplish this work. A big thank you to all the people from the lab, in particular to Sho, Alessio, Cornelius, Roberta, Viola, Omar and Ryan, for the stimulating discussions and fun that we had in and out the lab. I want to thanks my family: mamma, papa' and Chiara, who always supported me from miles away. Finally, very special thanks to my future wife, Barbara, who has been my light in every single moment of the past years.

For my grandparents Nonna Uberta e Nonno Emilio that now keep an eye on me from the sky.

Table of contents

Nomenclature **xv**

1 Introduction **1**
1.1 Motile cilia . . . 1
1.2 Functions of motile cilia in mammals . . . 5
1.2.1 Cilia in the airways. . . . 5
1.2.2 Cilia in the nervous system . . . 8
1.3 Motile cilia synchronisation . . . 9
1.3.1 Synchronisation in model cilia . . . 11
1.3.2 Synchronisation of flagella in microorganisms . . . 13
1.3.3 Cilia coordination in mammalian tissues: open questions . . . 17
1.4 Cilia alignment in mammals . . . 18
1.4.1 Planar Cell Polarity pathway . . . 19
1.4.2 Role of hydrodynamic forces in cilia alignment . . . 21
1.5 Research questions . . . 24

2 Transwell-chip: a novel device for applying shear flow to cells at ALI **27**
2.1 Fabrication of the Transwell-chip . . . 30
2.2 Protocols of cell culture in Transwell-chip . . . 32
2.2.1 Differentiation of ependymal cells . . . 32
2.2.2 Differentiation of airway cells . . . 33
2.3 Measuring the shear stress in microfluidic channels . . . 35
2.4 Novel setups to apply shear stress on airway and brain cells . . . 37
2.4.1 Constant shear flow setup . . . 38
2.4.2 Oscillatory fluid flow setup . . . 41
2.4.3 Air Shear Stress setup . . . 42
2.5 Conclusions . . . 43

3 Hydrodynamic entrainment of mammalian cilia in the brain 45
3.1 Experimental setup and methods . . . 47
3.1.1 Image acquisition and analysis . . . 47
3.1.2 Cytochalasin-D treatment for actin depolymerisation . . . 50
3.2 Entrainment of multiciliated cells with external flow . . . 50
3.3 Entrainment depends on the number of cilia . . . 52
3.4 Hydrodynamic screening affects the entrainment of motile cilia . . . 54
3.4.1 CBF increases with the number of cilia per cell . . . 57
3.5 Estimation of the flow generated by cilia within a cell . . . 61
3.6 Discussion and conclusions . . . 65

4 Investigating the role of external flows and viscosity in the alignment of cilia in the brain 69
4.1 Introduction . . . 69
4.2 Methods . . . 70
4.2.1 Cell culture and flow treatment . . . 70
4.2.2 Image acquisition procedure . . . 72
4.2.3 Image analysis . . . 72
4.3 Cilia alignment with external flows . . . 74
4.3.1 Alignment of ependymal cilia is independent from days in culture. . . 74
4.3.2 Cilia-driven flow and alignment depend on local cell density. . . . 77
4.3.3 New insights in cilia response to fluid flow the and future works . . 79
4.4 Frequency and orientation spatial coordination do not increase with global alignment. . . . 80
4.4.1 Spatial correlation of the cilia beating directions . . . 80
4.4.2 Spatial coordination of ciliary beating frequency . . . 82
4.5 Effects of medium viscosity during cell differentiation . . . 84
4.5.1 Experimental procedure and protocols. . . . 87
4.5.2 CBF and cilia orientation correlation length decrease with medium viscosity . . . 87

5 Investigating airway cilia alignment with external flows 89
5.1 Cilia response to prolonged air shear stress . . . 91
5.2 Cilia response to fluid shear stress . . . 94
5.3 Conclusion and future works . . . 96

6 Conclusions **99**
6.1 Open questions and outlooks 101

Appendix A Toward detection of lung cancer specific biomakers in exhaled breath with Transwell-chip **103**
A.0.1 Deregulation of SOX2 leads to dysplastic phenotype in Transwell-chips. 105
A.0.2 Prospectives 105

Appendix B Supplementary considerations on cilia entrainment with hydrodynamic forces **107**
B.1 Entrainment of a two state oscillator in viscous liquid and the effect of interciliary dissipation 107
B.1.1 The effect of intraciliary dissipation on cilia entrainment 108
B.2 Considerations on the role of steric interactions in ciliary beating frequency and entrainment 109
B.3 Hydrodynamic simulations of cilia bundles 112

References **117**

Publications list

Some chapters of this thesis are partly reproduced from the the following research articles

1. **Synchronization of mammalian motile cilia from the brain with hydrodynamic forces.** N. Pellicciotta, E. Hamilton, J. Kotar, M. Faucourt N. Spassky, P. Cicuta, *bioRxiv*, 2019, https://doi.org/10.1101/668459.

2. **Motile cilia hydrodynamics: Entrainment versus synchronisation when coupling through flow.** E. Hamilton, N. Pellicciotta, L. Feriani, P. Cicuta, *Philosophical Transactions of the Royal Society B*, 375.1792, (2020), 20190152.

Nomenclature

Acronyms / Abbreviations

AC Alternate current

ALI Air liquid interface

ASL Airways surface liquid

BF Bright field videos

CBF Ciliary beating frequency

CF Cystic fibrosis

CSF Celebro spinal fluid

CSN Central nervous system

DDM Differential Dynamic Microscopy

DIV Days *in vitro*

DMEM Dulbecco's Modified Eagle's Medium

DMSO Dimethyl sulfoxide

FBS Fetal bovine serum

FFT Fourier transform

FL Fluorescence microscopy videos

FOV Field of view

fps Frames per second

hAEC Human airways epithelial cell

ID Internal diameter

IER Impenetrable Effective Rod

mAEC Mouse airways epithelial cell

MC Methyl cellulose

MMC Mucociliary clearence

MT Microtubules

MWs Metachronal waves

NA Numerical aperture

NCS Neural stem cell

OD Outside diameter

PBS Phosphate buffered saline

PCD Primary ciliary dyskinesia

PCL Periciliary layer

PCP Planar Cell Polarity

PDMS Polydimethylsiloxane

PID Proportional integral derivative

PIV Particle image velocimetry

RFT Resistive force theory

SEM Scanning electron microscope

SOX2 sex-determining region Y-box 2

STED Stimulated emission depletion microscopy

TEM Transmission electron microscope

Chapter 1

Introduction

1.1 Motile cilia

A conserved structure across the eukaryotic species

Motile cilia are whip-like cell organelles that protrude from the apical cell membrane and exhibit regular bending waves able to produce fluid flow in a broad range of eukaryotic organisms [1]. Cilia length and number per cell can vary across species. For example, human sperm cells are propelled by a single motile cilium of 70μm (or flagellum in this case) while multiciliated cells in mammals can have from 30 to more than 300 cilia per cell with a length between 7 and 13μm [2], Figure 1.1. By contrast, the internal molecular structure and diameter of the cilium are remarkably conserved among all the organisms. Single cilium has a diameter of about 200 nm, and its structure can be divided into subcompartments that include a basal body, transition zone, axoneme, ciliary membrane and the ciliary tip [3], Figure 1.2a.

The axoneme is the skeleton of the cilium, and it is composed of microtubule bundles enclosed in the ciliary membrane (an extension of the cell membrane) [5]. The internal structure of the axoneme determines the cilium function. Primary cilia have an axoneme composed of nine peripheral doublet microtubules (9+0) and are immotile. In many organs, they act as fluid flow transducers [6] through mechanisms still in debate [7]. By contrast, motile cilia have an axoneme composed of two central single microtubules (with some exceptions, such as nodal cilia [8]) surrounded by the nine doublets held together by crosslinks [5], and move in a wave-like fashion producing fluid flow. The central pair of microtubules has been suggested to be necessary for a planar beating pattern [9].

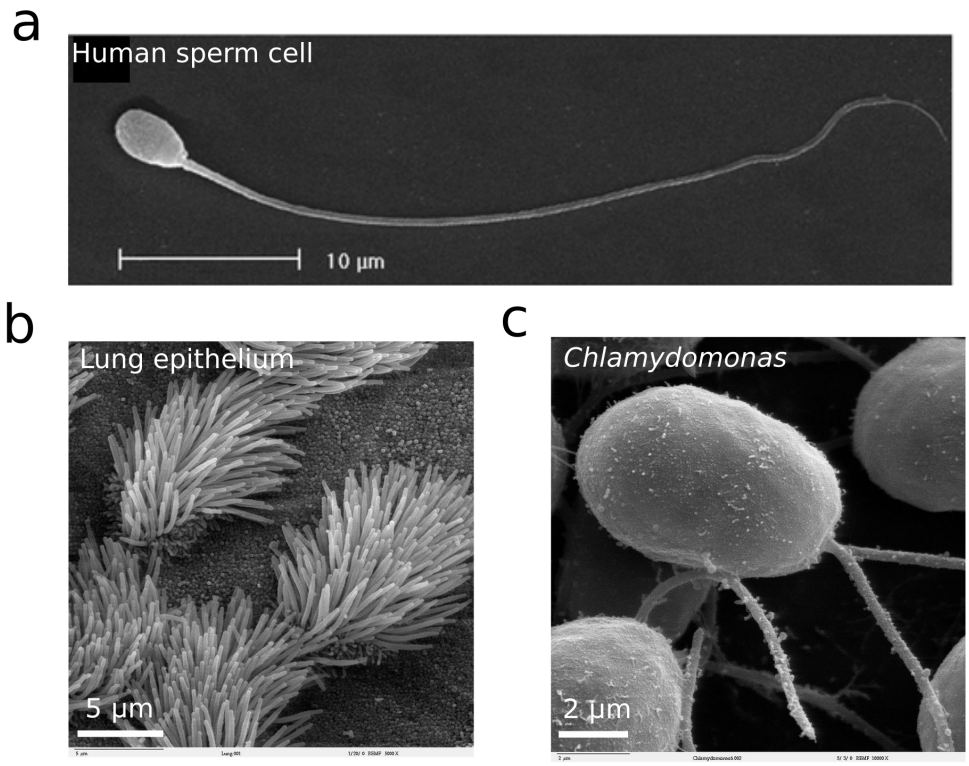

Fig. 1.1 **Scanning electron microscopy images of cells bearing motile cilia**. a) Human sperm cell [4]. b) Bronchial epithelium with multiciliated cells. c) *Chlamydomonas reinhardtii* algae. Figure (a) and (b) from Dartmouth Electron Microscopy Facility, Dartmouth College.

The basal body anchors the cilium to the membrane and apical cell cytoskeleton [10, 11] and is a nucleation point for the generation of the axoneme. It is composed of a modified centriole, which is a subcellular structure responsible for the microtubular organisation. It contains specialised structures, such as striated rootlets and the basal feet. The latter is connected to cytoplasmic microtubules of the cell and oriented in the same direction as the cilium's plane of beating [12, 13].

Motile cilia motion

The motion of a motile cilium can be divided into two phases: (i) a planar "power stroke", where the cilium is extended in order to maximise the entrained fluid and a (ii) "recovery stroke", where the cilium retracts toward the apical surface to minimise interaction with the fluid and returns to the initial position [17], Figure 1.2d. The recovery stroke can often be in a third dimension (out of the plane of the power stroke) depending on the organism [16]. The physical reason for a two-phase process can be found in the equation governing the fluid at

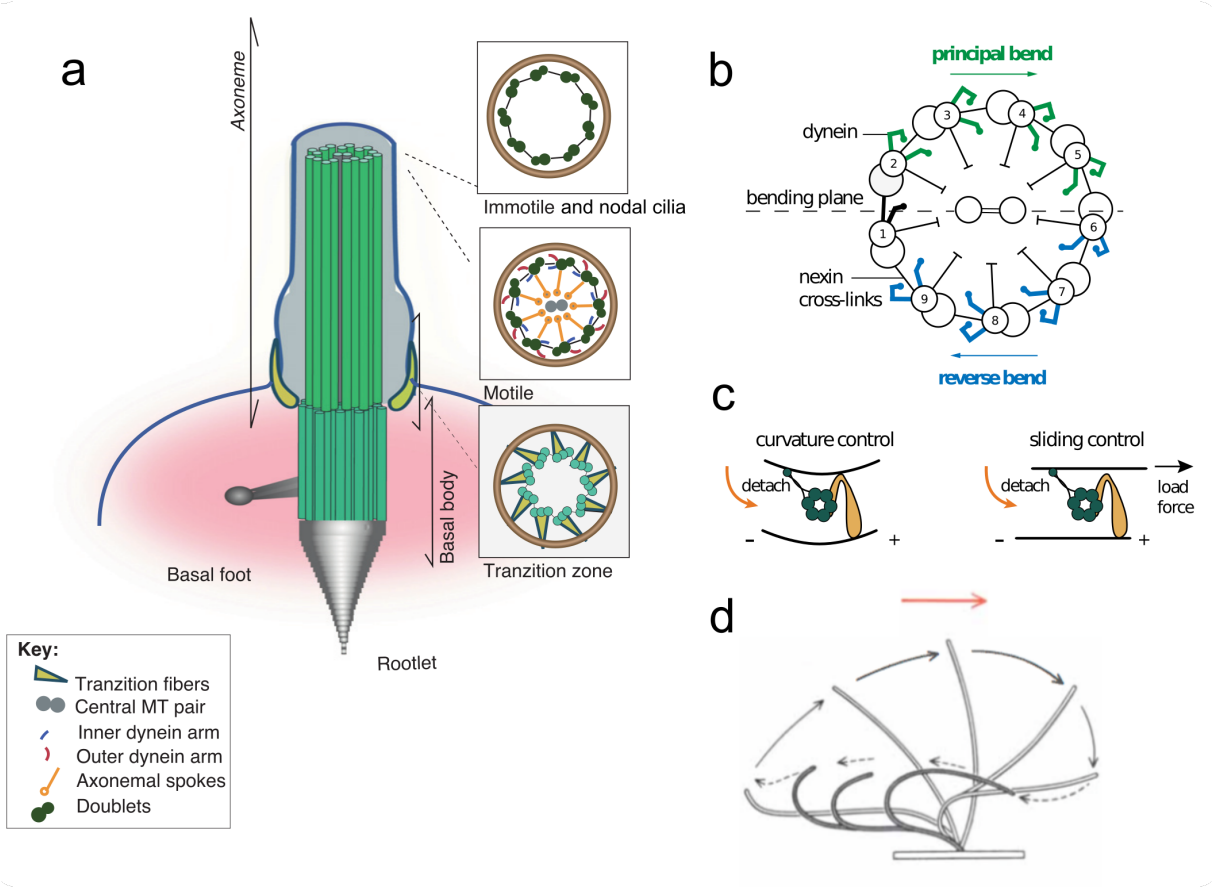

Fig. 1.2 **Cilia structure and motion.** a) the axoneme is the skeleton of the cilium/flagellum, and its internal structure identifies cilium function. In the primary cilia (no motile) and nodal cilia (motile), the axoneme is composed of nine doublets with no dynein arms (9+0). In motile cilia, the axoneme contains nine microtubules (MT) doublets with dynein arms and a central MT pair (9+2). The basal body seeds the growth of the cilium, it contains specialised structures, such as striated rootlets, basal feet and transitional fibres, provides mechanical support to the cilia, anchoring the basal body to the apical cytoskeleton of the cell. Moreover, basal feet are an indicator of cilia beating direction. The distal part of the basal body is called the transition zone, where the outer tubule stops growing. Illustration adapted from [14]. b) Cross-section of a motile cilium axoneme. The activation of the green dyneins causes cilium bending on the right, while activation of the blue motors leads to bending in the opposite direction. c) Illustration of the curvature and sliding control mechanism for mechanical feedback of dyneins: in the curvature model dynein inactivates with increasing curvature, while in the sliding model detachment is controlled by tangential forces. Illustrations b)-c) taken from [15]. d) Illustration of the asymmetric cilium beating pattern cycle. The beat of a typical cilium consists of a straight-armed "power stroke" (white cilia), where the cilium is extended to maximise the entrained fluid, followed by a curling "recovery stroke" (grey cilia), where the cilium retracts toward the apical surface to minimise interaction with the fluid often in a third dimension (out of plane of paper) [16]. The red arrow indicates the direction of the generated fluid flow.

the time and length scale of a cilium. Usually, cilia beat at a frequency of 5 to 100 Hz and are of order 10 μm in length. With these numbers, it can be found that cilia live in low Reynolds number environment ($Re \ll 1$), where viscous forces are much larger than inertial forces. In this situation, non-reciprocal cycles are a necessary condition to generate a net force on the fluid [18, 19].

The motile cilia movement is regulated by a set of molecular motors powered by ATP, the axonemal dyneins [20]. These are large motor proteins anchored at regular intervals along the length of the microtubule doublets. In the presence of ATP, the dynein arms take steps towards the minus end of the neighbouring doublet [21], generating a local sliding force that produces bending movement when the native structure with crosslinks is maintained [22, 23]. Strikingly, dynein activity must be coordinated to avoid a tug of war in the axoneme. For example, axoneme bending in one direction requires dyneins on one side to be active while those on the other to be inactive, Figure 1.2b. This behaviour was recently experimentally visualised for the first time in the swimming sea urchin sperm cells using cryo-electron tomography [24]. It is still unknown how dynein switching is spatiotemporally controlled to achieve the cilia beating pattern [25]. The current hypothesis that dynein coordination is a result of mechanical feedback: the axonemal dyneins generate forces that bend and deform the axoneme, in turn, deformation of the axoneme leads to local stresses and strains that regulate the activation of dyneins themselves [15, 25, 26], Figure 1.2c. The beating of bull sperm was measured to well fit with a sliding control-mechanism, where the build-up of sliding forces on one side of the axoneme induces detachment of the dyneins on the other side, leading to axonemal bending [27], Figure 1.2c.

However, it has been recently observed that the bending waveforms of *Chlamydomonas reinhardtii* flagella, Figure 1.1c, are in agreement with another feedback model, the derivative curvature control mechanism. Here, the time derivative of the doublet curvature regulates the dyneins detachment [15]. This mechanism takes into account also the intrinsic static curvature of the *Chlamydomonas* flagella, that is not present in the sperm flagellum. The resulting scenario is that mechanical feedback mechanisms that control dyneins coordination may operate differently depending on the biological system: sliding control being used in longer axonemes (sperm) and curvature control in shorter ones (mammalian cilia and *Chlamydomonas*). Another important model for dynein coordination is the geometric clutch, where the detachment of dynein is regulated by transverse forces that are present on adjacent doublets when they are curved [26, 15]. Future imaging techniques, in combination with appropriate perturbations, may help to visualise dynein activity and significantly contribute to unveil the mechanism of their coordination in cilia and flagella [24].

1.2 Functions of motile cilia in mammals

Some cells have motile cilia for the purpose of swimming. For example, mammalian sperm cells swim by the movement of a single cilium (or flagellum) [28], *Chlamydomonas reinhardtii* alga is propelled by two motile cilia beating in a breaststroke fashion [29]. The unicellular micro-organism *Paramecium* evolved a dense array of coordinated beating cilia on its surface to move around [30].

On the other hand, motile cilia also cover numerous epithelia in vertebrates with the role of generating a macroscopic flow fundamental for physiological functions [31]. For example, during embryonic development, cilia in the node create a leftward flow that establishes the Left-Right symmetry and the correct neurulation in mammals [8]. In mammals, cilia cover the lumen of the ear-nose-throat sphere, the lungs, the brain ventricles and part of the female and male reproductive tracts [2], Figure 1.3. Defects in ciliary motility cause a range of disease symptoms, including bronchiectasis [32], hydrocephalus [33, 31], ectopic pregnancy [34]. Here, cilia are arranged in dense arrays to optimise fluid generation, and each cell can have from 30 to 300 cilia depending on the organ. These cells are commonly identified as multiciliated cells.

In the female oviduct, the cilia function is to transport the oocyte toward the uterine cavity [34]. Loss of cilia flow can misplace the egg, causing ectopic pregnancies. The percentage of multiciliated cells can vary along the Fallopian tube length (from 30% to 80 %) [35]. Past studies suggest that ovum transport is supported by the sticky glycocalyx proteins present on the tips of cilia [36].

Cilia functions in the airways and central nervous system will be described in the following sections.

1.2.1 Cilia in the airways.

In the system of ears, nose, throat, lungs, the coordinated beating motion of ciliated cells is responsible for the mucociliary clearance: firstly the mucus works as a physical trap for inhaled pathogens, particles and toxic chemicals. Then, motile cilia transport the mucus out of the respiratory system to the pharynx, where it is swallowed [37].

The airway epithelium is composed of three major cell types: (i) secretory, (ii) basal and (iii) ciliated cells. (i) The secretory cells (mainly goblet cells) produce the layer of fluid and

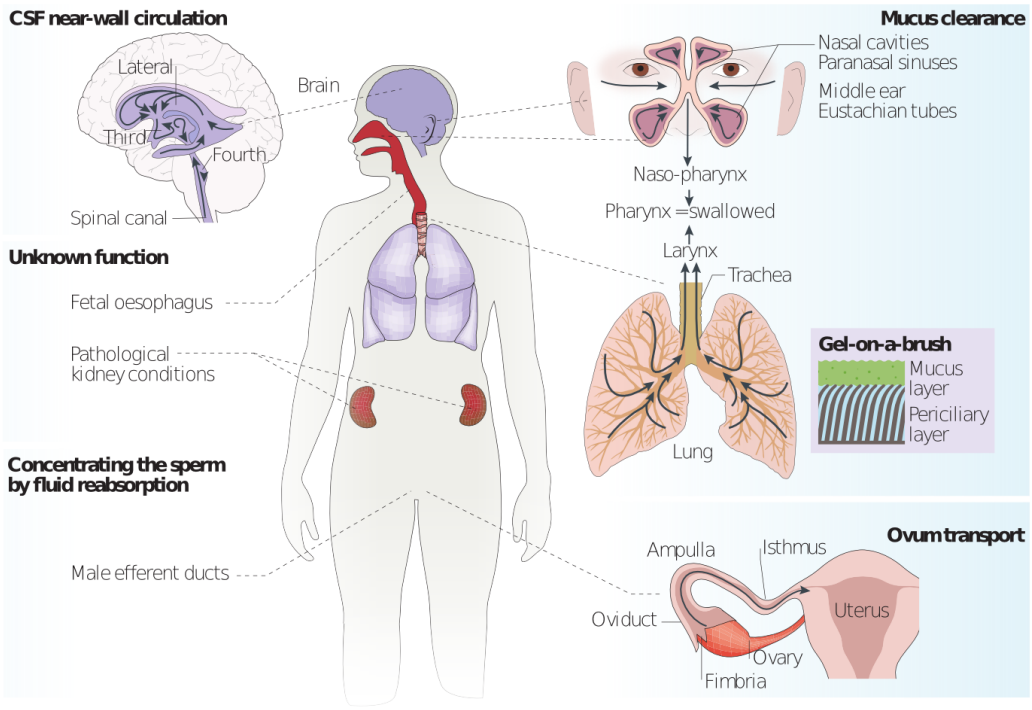

Fig. 1.3 **Functions and distribution of motile cilia in the human body.** Multiciliated ependymal cells are found in the lateral, third and fourth brain ventricles. These contribute to near-wall cerebrospinal fluid (CSF) propulsion. The function of ependymal ciliated cells in the spinal canal is not clear. Cilia in the lungs and ear-nose-throat sphere are fundamental for mucus transport towards the pharynx, where mucus is swallowed. In the female reproductive tract, ciliated cells lead to the efficient transport of the ovum towards the uterine cavity. In male efferent ducts, multiciliated cells resorb testis fluid, and cilia are supposed to generate reflux that permits only sufficiently concentrated sperm to pass. Multiciliated cells have also been observed in the fetal oesophagus and pathological kidney conditions, but their functions are unknown. Illustration from [2].

mucins above the epithelium. (ii) the basal cells are the only ones firmly attached to the basement membrane and function as a site for attachment of more superficial cells. Moreover, they can differentiate into ciliated and secretory cells responding to cell senescence and epithelium injury. (iii) Ciliated cells have up to 300 cilia that are $4-7\mu$m long and can beat at about 8-15 Hz [38], Figure 1.4a.

In the tracheobronchial tree, secretory cells are alternated with ciliated cells in an average ratio around 50:50, with the percentage of ciliated cells decreasing towards the distal end of the bronchioles [40]. Also, the nasal cavity and the ear are similarly covered by ciliated cells and are kept sterile by the cilia sweeping inhaled particles towards the pharynx [41]. In addition to these cell types, other more rare ones have also been identified, such as neuroen-

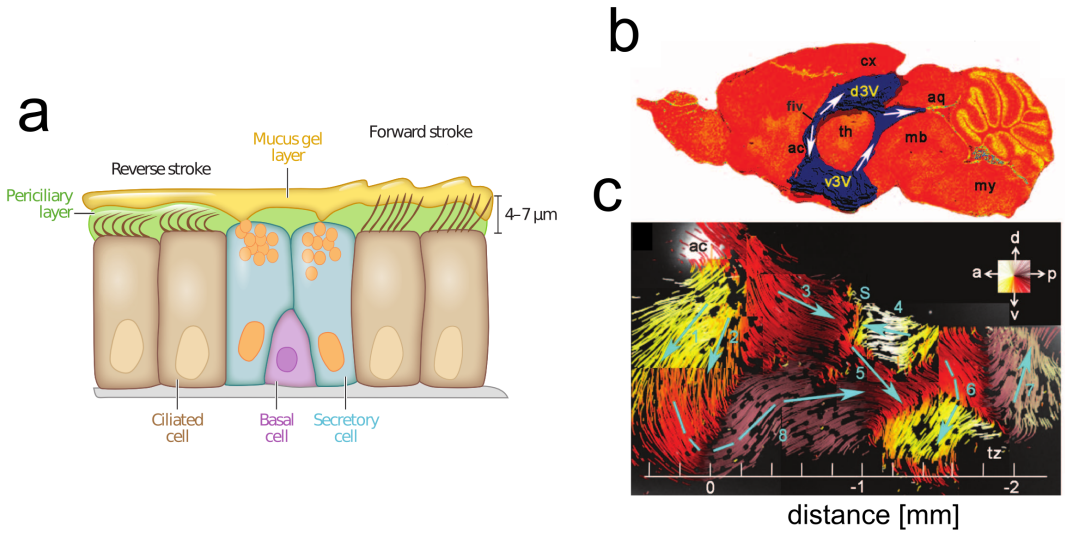

Fig. 1.4 **Cilia in the airways and third brain ventricles.** a) Cilia power and recovery stroke in the mucus and preciliary layer. Secretory cells produce the mucus gel layer that traps inhaled toxicants and infectious agents. During power stroke cilia tips push the mucus layer, and then they recede completely contained in the preciliary layer during recovery stroke [32]. b) Sagittal section of a mouse brain through the third ventricle. CSF is produced in the choroid plexus, flow into the dorsal (d3V) and ventral (v3V) ventricles and then exits through the aqueduct (aq). c) Near-wall flow generated by ependymal ciliated cells in the third ventral ventricle observed with tracer particles. The flow is structured in multiple flow domains and does not follow a defined axis; the reason for this complicated flow network is unknown. Colours indicate the direction of the flow. Figures (b)-(c) taken from [39].

docrine, tuft cells and ionocytes, that are the major source of transcripts for the conductance transmembrane protein affected in cystic fibrosis [42].

The effectiveness of mucociliary clearance relies on two components: the mucus layer that traps pathogens and, behind it, the periciliary layer (PCL), where cilia are immersed and provides a favourable environment for the cilia movement. Recent results [43] suggest that the PCL layer consists of membrane-spanning mucins and large mucopolysaccharides that, tethered to cilia and epithelium surface, form an extracellular mesh. This network prevents the molecules of the above layer of mucus and inhaled particles to penetrate the airway surface. By contrast, the mucus layer is a strongly viscoelastic fluid mainly composed of glycoproteins such as MUC5AC and MUC5AB, and its rheological properties are strongly dependent on its state of hydration [37]. These two layers, together with ciliated cells, provide an effective system for mucus propulsion. During the power stroke, the cilia tips are

extended into the mucus layer and push it on the direction of the stroke. By contrast, on the recovery stroke, the cilia come back to the original position completely embedded in the PCL layer so to minimise back-propulsion of the mucus layer [44], Figure 1.4a.

Motile cilia are key players in various airways diseases [31]. Mucociliary clearance is weakened in diseases involving abnormalities in the ciliary structure functions such as in patients with primary ciliary dyskinesia (PCD). Currently, 37 genes have been associated with PCD; in the majority of the cases, these genes involved mutations in the function of inner, the outer, or both dynein arms [45]. In the airways, PCD is associated with chronic rhinitis/sinusitis, otitis caused by fungi and bacteria infections [46]. Cilia motility can also be impaired in diseases such as Cystic Fibrosis, where the malfunction of Chloride channel lead to dehydration of the airways and consequent PCL collapse. This collapse, in turn, greatly hinders ciliary beat and paves the way to bacterial infections [43, 47].

1.2.2 Cilia in the nervous system

Cerebrospinal fluid (CSF) is a major part of the extracellular fluid of the central nervous system (CNS) and has vital functions for brain health and development. It acts as a cushion for the brain, distributes secreted trophic and metabolic signals throughout the ventricular system and is necessary for brain homeostasis and toxin washout [48]. In the traditional scenario, CSF is continuously secreted in the ventricles by the choroid plexus and flows unidirectionally to be absorbed into venous sinuses across arachnoid villi [49]. The choroid plexus consists of a network of capillaries that are separated from the ventricles by choroid epithelial cells. The blood filters through these cells to become cerebrospinal fluid [49]. The multiciliated ependymal cells covering all the ventricles were thought to sustain the cerebrospinal fluid (CSF) circulation [50, 51]. This hypothesis was supported by experiments with small animals such as rodents, where cilium-defective mutants develop hydrocephalus systematically [33, 31], that is a condition where CSF builds up in the brain ventricles and increases head pressure.

In the last decade, a growing number of works started questioning the pillars of this classical model of CSF circulation and the role of ependymal cilia. According to recent observations, CSF is produced and absorbed in the whole CSF system as a consequence of filtration and reabsorption of water volume through the capillary walls into the surrounding brain tissue. Moreover, by MRI measurements, it was observed that CSF moves in the nervous system in a bidirectional fashion due to the arterial pressure during the heartbeat cycle [49, 52]. These bulk flows were reported to be an order of magnitude higher than the

one created by cilia, questioning the role of motile cilia in sustaining the CSF flow. Recent computational simulations of fluid dynamics in humans nervous system suggest that bulk flow is indeed dictated by the CSF bidirectional flows, while only the microscale near-wall flow is dominated by the action of ependymal cilia [53, 2]. In agreement with these studies, there is medical evidence that ependymal cilia in humans are not so crucial for hydrocephalus phenotype. A significant number of patients with hydrocephalus have been diagnosed as well with immotile, dysmotile, or lacking cilia [54, 55]. In contrast, patients with immotile cilia syndrome had in small percentage slightly enlarged ventricles [31] and others had no enlargement at all [56]. These pieces of evidence suggest that ependymal ciliary dysmotility is not sufficient to cause hydrocephalus in humans but only increases the risk [3]. It is worth noticing that this is in contrast with what happens in smaller animals, where cilia have an essential role in sustaining the CSF circulations in small apertures (such as the ventricular aqueduct) and in avoiding CSF accumulation in the ventricles [33, 31].

Recently, It has been reported that near-wall flow, induced by motile cilia in the third ventricle cavity of mice, rat and pigs, is not unidirectional but highly organised in modules and gives rise to a spatiotemporally regulated network of fluid flows [39], Figure 1.4b-c. The specific function of these complex flow patterns is still unknown in any animal. However, they may be important for substance distribution to targets in this ventricle, such as periventricular hypothalamic nuclei that control circadian rhythms, hormone release, thermoregulation, blood pressure, satiety, and feeding [39, 57]. Alternatively, this flow network may account for preferred routes of communication between different brain regions. Neural stem cells of adult rodents extend in the ventricles a single, non-motile sensory cilium at the centre of rosettes of ependymal cells [58]. In mice, a chemical gradient in the neurogenic region lying beneath the ependymal epithelium has been suggested to rule orientation and migration of new neurones towards the olfactory bulb [59]. These observations indicate the existence of direct biochemical and/or physical regulation of adult neurogenesis by ependymal ciliated cells; however, more experiments are still needed to address this fascinating question [2].

1.3 Motile cilia synchronisation

The synchronisation is a fascinating phenomenon widely observed in nature. For two oscillators synchronisation can be defined when they move at the same frequency and with a phase difference constant in time (‘phase-locked’) [60]. This definition can be generally extended to any individual element with some time periodicity. Across biological systems, synchronisation can be observed, for example, in swarms of fireflies flashing with the same rhythm in

the summer nights [61], the audience of people synchronising their hand-clapping [62], to the cellular level of synchronisation of heart cells that interact to set the normal heart beating [63, 64].

Motile cilia are another example of biological oscillators that exhibit synchronisation. Single cilia/flagella can synchronise to external oscillatory flow [65]. The two flagella of *Chlamydomonas reinhardtii* algae synchronise in a breaststroke fashion to propel the body forward [29]. Motile cilia of multiciliated epithelium have the universal tendency to develop synchronous beating patterns known as metachronal waves (MWs), Figure 1.5. Here, all the cilia are aligned and beat at the same frequency with a spatial modulation in phase [66]. In a two-dimensional cilia carpet, the direction of the spatial phase modulation can be not aligned with the direction of the cilia beating. For this reason, metachronal waves can be distinguished either symplectic, antiplectic, dexioplectic, or laeoplectic, depending to whether the power stroke of their cilia is with, against, to the right of, or to the left of, the direction of movement of the waves [67] . Metachronal waves have been shown to be optimal for generating a stable and uniform flow [68] and have fundamental roles in microorganisms [67, 30, 69, 70]. Moreover, these have been observed in organs of mammals, such as in the airways [71, 72].

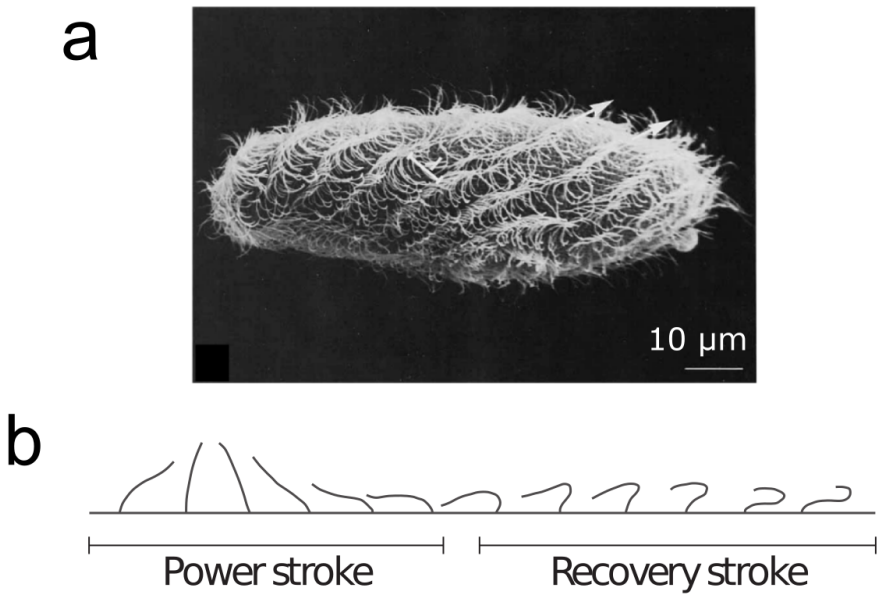

Fig. 1.5 **Motile cilia metachronal wave.** a) SEM image of a fixed *Paramecium* while swimming forward where typical metachronal waves are observable. Bar 10μm, image from [73]. b) Cilia spatial configuration during a metachronal wave.

From the pioneering studies of Huygens in 1665, we know that oscillators with different intrinsic frequencies can reach synchronisation if mechanically coupled [74]. It is the current hypothesis that cilia-driven flow could also itself be the mechanical origin of cilia pair synchronisation and large scale coordination [75, 76]. Cilia are microscopic filaments extended and moving into the fluid, and therefore the fluid will also act as a medium that will mechanically couple every single cilium. So, hydrodynamic interaction between cilia could provide the physical mechanism for their synchronisation and metachronicity, [77]. For the first time in 1949, Rothschild reported synchronisation of eukaryotic flagella through fluid interaction. He observed that bull sperm flagella tend to synchronisation when they swim close to each other [78]. To explain this observation, in 1951, Taylor modelled two hydrodynamically coupled sperm flagella as two infinite and inextensible parallel sheets with prescribed sinusoidal travelling waves. He found out that the condition of minimum viscous dissipation was achieved when the two travelling waves were in phase [77]. However, the minimisation of dissipation was still not enough to deduce the dynamical process of synchronisation.

In the last decades, the hydrodynamic origin of cilia synchronisation has been supported by simulations of pairs [79] and arrays of cilia [68, 80, 81], experiments with cilia models [82–84] and with ciliated microorganisms from the genus *Paramecium* [70, 30], *Chlamydomonas* [29] and *Volvox* [85, 69, 86].

However, recent experiments with *Chlamydomonas* algae showed that flagellar synchronisation is disrupted when the internal elastic fibre connecting the basal bodies apparatus is affected [65, 87, 88]. The importance of inner coupling in this organism was also supported by recent theoretical studies [89, 90]. This scenario enlightens the possibility that cilia coordination be achieved in nature in different ways, thus leaving unclear what could be the underpinning mechanism in other systems such as mammalian tissues. In this section, I will review some of the theoretical and the experimental works aimed to understand the mechanisms of cilia coordination.

1.3.1 Synchronisation in model cilia

Minimal models of hydrodynamically interacting oscillators have the potential to give useful insight into the emergence of cilia pair synchronisation [91, 79] and metachronal wave formation [75, 68, 80, 81]. Under certain conditions, hydrodynamic interactions alone can induce phase-locking of cilia models such as rotating paddles [92], light-driven microrotors

[84], or colloids driven in optical tweezers [83, 82, 93].

In our group, such problems have been investigated in the last ten years using microscopic beads controlled via optical tweezers [83]. For cilia that are distant more than few microns, as for the microorganisms *Paramecium*, *Volvox* and *Chlamydomonas*, past works have reported that the flow field generated by a single cilium is very similar to the one created by a sphere in the cilium centre of drag [94, 85, 83]. Therefore, the degrees of freedom of the complex cilium shapes and activity can be captured by a driving potential acting on the sphere. The main advantage of this approach is that it greatly simplifies the calculation of drag forces, both those acting on the individual object and the force induced by one object on another [95, 96]. Using this approximation, they investigated the synchronisation of two one-dimensional free-phase oscillators ('rowers'), driven by two optical traps that alternatively switch on and off according to the bead positions, see Figure 1.6a. The potential of the optical trap acts as driving potential and can be tuned to mimic the power and recovery strokes of a cilium [82, 93]. Each rower is phase-free: in the absence of hydrodynamic interactions, the driving potential sets the oscillation frequency of each rower. However, the phase of the oscillation can be changed by the hydrodynamic interactions with the neighbour rowers. When a cilium beats, its centre of drag moves along a given orbit, that can be either in two o three dimensions. Thus, a second way to model a cilium is hence to prescribe the particle to move along an orbit [83]. This model is known as 'rotor'. Here, the phase is set by orbit shape and by the driving force acting on the particle, which represents the force provided by the cilium, in the direction tangent to the path. The orbit can be made flexible by allowing the particle to deviate from the circular path in the radial direction, and a harmonic restoring force of controlled stiffness tends to keep the particle on the predefined path [83]. In this way, the circular trajectory breaks the time-reversal symmetry required for the synchronisation [97, 90]. In both these models, a regime was found (in terms of size of the oscillator and amplitude of the motion) over which hydrodynamic synchronisation occurs, Figure 1.6b. It is worth noticing that biological cilia are well within this predicted regime [83].

The emergence of metachronal waves in cilia models has been investigated with simulations including hydrodynamic interactions. For example, chains of rowers [98, 99] and rotors [81] can show metachronicity under particular conditions. Another category of cilia models is actively-driven semiflexible filaments. Each filament is driven by internal forces to reproduce the beat of a real cilium (power and recovery stroke) and can react to the flow produced by a nearby beating filament. Such filaments, when arranged in 1D and 2D arrays,

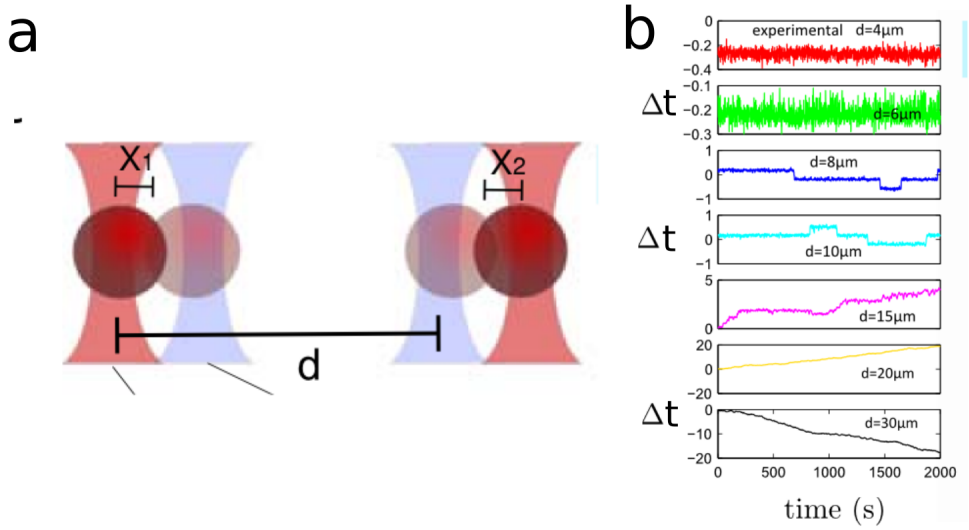

Fig. 1.6 **Hydrodynamic synchronisation of two rowers.** a) Setup of two rowers. Beads driven by optical tweezers with fixed amplitude but free in phase. The optical trap alternates between two positions using a "geometrical switch" triggered by the position of the bead. b) The switch time difference Δt over oscillations periods of the two rowers at different distance d. Phase locking is observed for values of $d < 15\mu m$, where Δt is always less than one. Beads radius used in these experiments is $a = 1.5\mu m$; the amplitude of oscillations is $1\mu m$.

also have the tendency to have metachronal coordination [75, 80, 68].

Overall, experiments and simulations with minimal models suggest that hydrodynamic interactions are sufficient for pair flagella synchronisation of *Chlamydomonas* and metachronal wave formation observed in dense arrays of cilia. Whether the behaviour of minimal models can match real biological cilia can be only confirmed by experiments. Particularly useful insights into new mechanisms have been provided by experiments on flagellated microorganisms.

1.3.2 Synchronisation of flagella in microorganisms

The synchronisation and metachronal wave formation has been extensively studied in model organisms such as algae and unicellular eukaryotes for their easy manipulation and growth conditions [67]. The *Chlamydomonas* alga model, that has been used for decades to study cilium structure and function [100], it has been recently adopted to investigate also flagellar synchronisation. This alga swims forward when the two flagella/cilia beat in phase in a cyclic

pattern resembling a “breaststroke” motion, Figure 1.7a, making it a perfect experimental candidate to investigate pair flagellar synchronisation.

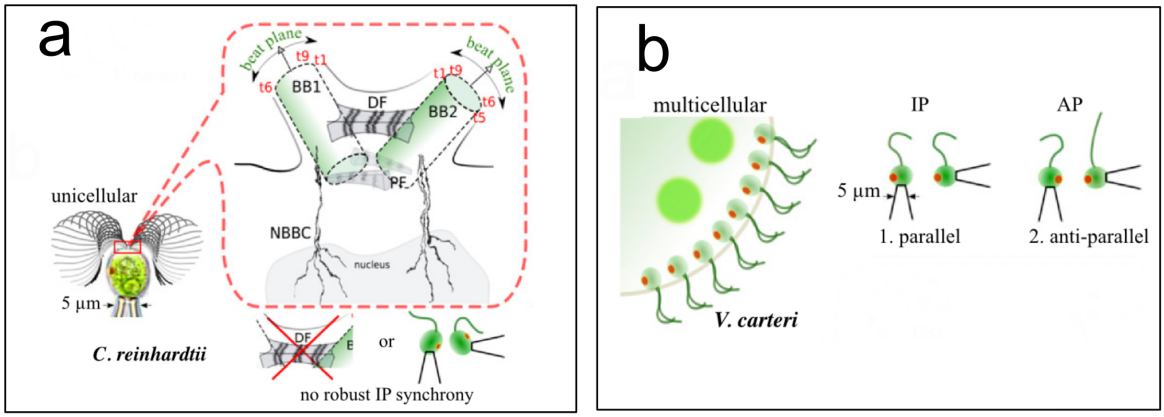

Fig. 1.7 **Flagellar synchronisation in microorganisms.** (a) *Chlamydomonas* swims with two flagella beating in phase but oriented in the opposite direction, similar to a breaststroke style. The robust inphase synchronisation is lost in algae mutant with depleted inner coupling (distal fibre DF) and in pairs of nearby unfilagellated cells held with micropipettes. In the red insert are shown the two flagellar basal bodies (BB) connected by the distal fibre (DF) inside the cell body. b) *Volvox* colony is composed of thousands of biflagellated somatic cells that move coordinately in a metachronal fashion. In an isolated somatic cell, flagella beat inphase along the same direction. Isolated flagella from two somatic cells synchronise either in antiphase (AP) or inphase (IP) depending on their relative orientation. The illustration is taken from [87].

Is *Chlamydomonas* flagella synchronisation achieved by hydrodynamics or basal coupling?

In the dark, when phototactic reorientations do not occur, the flagella of *Chlamydomonas* exhibits stochastic switches between synchronous and asynchronous state. When flagella start beating at a different frequency, the cell is able to change direction. This behaviour leads the alga to move in a run-and-tumble motion that resembles bacteria chemotactic strategy [101]. The synchrony state of the swimming alga was reported to be consistent with hydrodynamic coupling [29]. Further observations were made using micropipettes to hold the algae in place. For example, flagella synchrony spontaneously develops as flagella regrow, with increasing phase-locked periods consistent with an inter-flagellar coupling that grows linearly with flagellar length. This consideration supports the view that flagellar synchronisation is purely mechanical and not through a biochemical state of the cell [102].

In addition to direct hydrodynamic interactions, flagella synchronisation of a freely swimming *Chlamydomonas* could also be induced by cell body rocking movements. Phase slips between the two flagella can alter the balance of hydrodynamic drag on the cell body, producing a rotation of the cell that promotes subsequent re-synchrony of flagella [103, 104]. The same authors suggested that residual motion of elastically-clamped cells on micropipette would still allow synchronisation through cell rocking and lead to misinterpretations of previous studies.

Nevertheless, a series of recent experiments proposed that flagellar synchronisation of this alga is instead mechanically driven by the elastic coupling through the cytoskeleton. Algae deficient of the internal fibre coupling cilia basal bodies were observed to display significant different synchronisation from the wild type [88]. Quaranta *et al*. studied the phase-locking between an external oscillatory flow and *Chlamydomonas* flagella. They measured that the required hydrodynamic forces for phase locking are over an order of magnitude larger than the ones between flagella, [65]. Moreover, Wan *et al.* demonstrated the insufficiency of hydrodynamic coupling in an evolutionarily range of unicellular algal species bearing multiple flagella, including the *Chlamydomonas* alga. These authors suggested precise flagellar coordination through elastic fibres of the basal apparatus [87], Figure 1.7a.

Flagellar synchronisation of *Chlamydomonas* through basal coupling has also been recently studied using a description of the beating flagellum as a limit-cycle oscillator, which was calibrated and tested against experimental data [105]. This representation of a cilium has been successfully used to describe flagellar synchronisation of the algae with an external flow [106]. Markedly, this model also predicts that stable flagellar in-phase synchronisation requires symmetry breaking from both flagellar waveform compliance and basal coupling between flagella [107]. This hypothesis was also supported by others [89]. Whether hydrodynamic forces could act together with elastic forces though basal coupling to achieve flagellar synchronisation is still unclear and requires further investigations.

Organism-dependent mechanisms of synchronisation.

A different possible scenario arises from recent studies on the colonial alga *Volvox carteri*. This colonial organism is composed of thousands of biflagellate somatic cells embedded in a spherical extracellular matrix of radius $R \approx 200\mu$m that have flagella beating in a metachronal fashion to move around [108, 69], Figure 1.7b. The emergence and defects agreed semiquantitatively with minimal elastohydrodynamic models [69, 86].

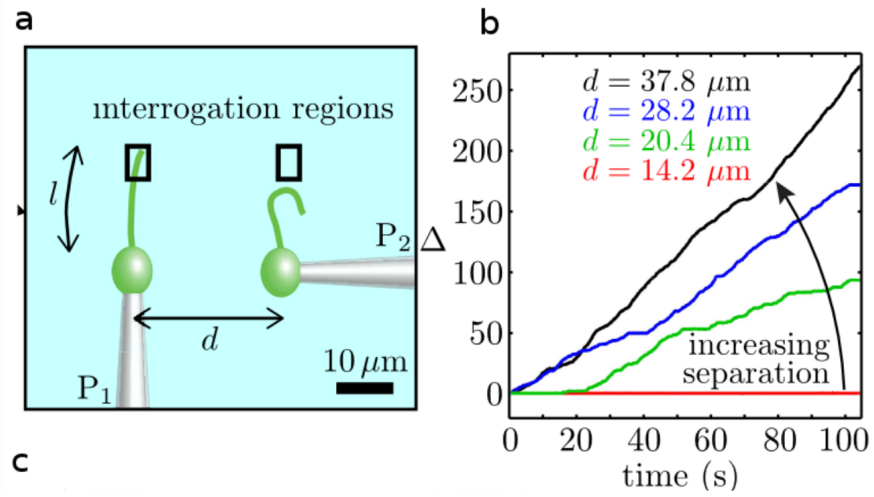

Fig. 1.8 **Hydrodynamic synchronisation of isolated flagella from *Volvox*.** a) Schematic setup of two cells of *Volvox Carteri* that are hold with micropipettes at a controllable distance d. b) The phase difference Δ between the two cilia over time is shown at different separation distance d. For $d = 14.2\mu m$ the two cilia are phase locked.

In a fascinating experiment, Goldstein's group demonstrated that isolated flagella of different somatic *Volvox* cells could synchronise their motions through direct hydrodynamic interactions. The authors studied two somatic cells held with micropipettes, where each cell had only one flagellum with a distinct intrinsic beating frequency, Figure 1.8a. Flagellar synchronisation of these two flagella was studied by high-speed imaging as a function of their separation and orientation [85]. They measured stable in phase synchronisation when the two isolated flagella were beating in the same direction, while anti-phase synchronisation when one of the two flagella was reversed [87], Figure 1.8b. These experiments showed indubitably that for *Volvox* colony the flow generated by a beating flagellum is sufficient to synchronise the beating of other nearby flagella, without any physical connection or chemical signalling.

By contrast, flagella from micropipette-held *Chlamydomonas* algae showed synchronisation states markedly different from the wild type flagellar synchronisation, Figure 1.7a-b. Synchronisation states were unstable and alternated between in-phase and anti-phase even if the flagella pairs were oriented as in the wild-type configuration. These observations guided the conclusion that flagellar synchronisation of *Chlamydomonas* cannot be reconciled with hydrodynamic theory, as opposed to the *Volvox* somatic cell. It was suggested that this difference could arise from the fact that *Volvox* somatic cell has a reduced hydrodynamic screening by a smaller cell body than the *Chlamydomonas* alga. Another possible reason could be the disposition of basal bodies, that is different in the two organisms [87]. Moreover, differently

from *Chlamydomonas* breaststroke, somatic cells of *Volvox* swim in colony performing metachronal waves, so these organisms may have involved hydrodynamic interactions in their swimming strategy in a different way. Despite the numerous works on this topic, the key factors underpinning the difference between these ciliated organisms is still unknown.

1.3.3 Cilia coordination in mammalian tissues: open questions

Theoretical and experimental works on cilia synchronisation and metachronal waves (MWs) emergence have been mostly restricted to micro-organisms because more suitable for systematic studies of flagella and flows that they create. However, such systems can not reproduce many characteristics of mammalian ciliated tissues, and there is no guarantee that the same results can be shared between these biological systems. For example, in microorganisms as *Paramecium* [17, 30] and *Volvox* [86, 69]. In contrast, cilia are often distant more than a few microns, while mammalian cilia in multiciliated epithelia are significantly packed within a cell [2], with up to 300 cilia for a cell of few microns. Here cilia density is higher than the range explored by previous works on cilia synchronisation, and steric interactions between cilia are also possible. Moreover, some mammalian ciliated cells beat in a non-Newtonian medium, and so the elastic modulus of the fluid may play an important role for the synchronisation [109]. In the airways, cilia are also tethered by mucins that provide further mechanical coupling between them [43]. Nevertheless, motile cilia in mammalian cells are (inevitably) coupled to some extent through the cilia-driven flow, but are also structurally connected through the actin mesh that links all cilia of the same cell at the base elastically [11, 10, 110]. Even on the scale across confluent cells, the epithelium could transmit forces elastically, and in principle, these connections could lead to synchronisation [110, 90].

Another related point concerns the emergence of metachronal coordination in mammalian ciliated tissues. Although metachronal waves (MWs) are reported to be optimal for fluid propulsion [68] and fundamental for swimming of few microorganisms, it is not clear whether this coordinated behaviour always emerges in ciliated organs of mammals and has any physiological function. In airways, metachronal waves were reported to be restricted to patches of few cells and to have varying directions of wave propagation [71, 72]. No works are reporting MWs in other mammalian ciliated organs such as fallopian tubes and brain ventricles. Indeed many factors can impede or alter the development of cilia coordination over large-scale (respect to the cell size). For example, the patchiness of ciliated cells in the tissue, as reported in [111]. Percentage of ciliated cells in fallopian tubes can vary from 30% to 80% [35]. In the airways, patches of ciliated cells and secretory cells alternate with a 1:1 ratio. Their heterogeneity is suggested to be optimal for mucus clearance [112], but it is not

known whether this can impair MWs formation. Another important factor is cilia beating direction orientation on the large-scale. In the brain, the complex network of cilia orientation [39] may prevent the development of large scale coordination. In cultures of airway cells, where ciliated cells are not aligned along a common axis [113], small scale coordination is present, and MWs were not observed [114].

Even though the cilia structure seems to be conserved in nature, it seems difficult to draw conclusions on cilia coordination of mammalian systems using only studies on microorganisms. As highlighted in the previous section, microorganisms seem to have developed different mechanisms for cilia/flagella synchronisation: hydrodynamic forces are not enough for the synchronisation of some algae [88, 65, 87]. In contrast, in other microorganisms, hydrodynamic coupling seems still the basic mechanism of coordination [85, 87]. Differences between how cilia respond to flow may be hidden by the lack of knowledge of how molecular motors in the cilium respond to forces and drive cilia motion [15], or how basal bodies are arranged in the cell cytoskeleton [87]. Given these organism-dependent mechanisms, experimental studies on specific mammalian systems are now particularly valuable to understand the physiological role of cilia coordination and how these relate to cilia diseases. One should first ensure experimentally that hydrodynamic forces between mammalian cilia are sufficient for synchronisation. One possible approach is to study the response of cilia to external flow [65]. Then, further works investigating the role of cilia patchiness, orientation and intracilia noise in the emergence of MWs are needed to represent more realistically mammalian tissues. A combined effort from both biologists and physicists is essential to tackle the difficulties involved in dealing with these systems that often require invasive techniques and complex protocols of cell culture.

1.4 Cilia alignment in mammals

The cilia within each cell need to be aligned along one direction to create flow over a scale much larger than the cell size. Global cilia alignment requires cells to polarise along one axis and break the planar symmetry of the epithelium. But how polarity is established in any ciliated epithelia is not known [13]. In the airway, the coordinated beating of motile cilia is essential for mucus transport and airway clearance. Random cilia orientation is a cause of respiratory tract diseases, and it has been characterised as another type of Primary ciliary dyskinesia (PCD) [115], where the mucus transport is blocked, leading to bronchiectasis and chronic sinusitis [31, 32].

Lack of cilia alignment can also be a cause of mortality after trachea transplant. In some airway diseases that involve a large part of the trachea, such as tumour or stenosis, trachea transplant could be a solution [116]. In recent clinical trials, tissue-engineered scaffolds with recipient's cultured cells have been implanted in patients with successful results to treat significant tracheal defects [117]. However, some long term analysis resulted in numerous complications, such as migration, dislodgement, material degradation/failure, chronic bacterial infections [118]. One of the reasons is that cells grown *in vitro* in the scaffolds do not entirely mimic the properties of the *in vivo* system [119]. For example, these cells suffer from a tissue-level misalignment of beating cilia that causes respiratory tract diseases and eventually death [120].

Despite the fundamental importance in human health, the mechanism underpinning mammalian cilia alignment is not clear. A possible candidate is a biological signal pathway called Planar Cell Polarity PCP. This pathway has been identified in many fundamental processes when epithelial cells acquire a polarity that orients them along an axis within the plane of the sheet [121, 122]. Other studies highlight the importance of external flow and the flow generated by the cilia themselves. Overall, an interplay between the PCP pathway and hydrodynamic forces between cilia have been suggested to play an important role in the alignment of the planes of ciliary beating [80, 123–125]. In this section, we first introduce the PCP in *Drosophila* fly and mammals, then we describe its interplay with hydrodynamic forces in the establishment of mammalian cilia orientation.

1.4.1 Planar Cell Polarity pathway

PCP in *Drosophila*

PCP pathway was first identified in the *Drosophila* wing epithelium as a regulator of the coordinated orientation of external hairs [126]. This signalling mechanism is orchestrated by several proteins that migrate asymmetrically inside the cell and are able to transmit their polarisation to neighbours cells. Specifically, these proteins were named and identified according to loss-of-function phenotypes, which displayed irregular cellular hair orientation on the pupal wing: frizzled (Fz), dishevelled (Dsh), prickle (Pk), strabismus(Stmb)/ Van Gogh (Vang), flammingo (Fmi), diego (Dg). During the early stage of hair development, PCP proteins are mainly located around the adherent junctions of the cell membrane. At later stages, Fz, Dsh and Dgo are located at the distal edge of the cell, while Vang and Pk are concentrated on the apical edge of the wing [127], Figure 1.9. Then, this localisation is thought to control the activation of PCP signal cascade initiated by Fz and Dhs. The end

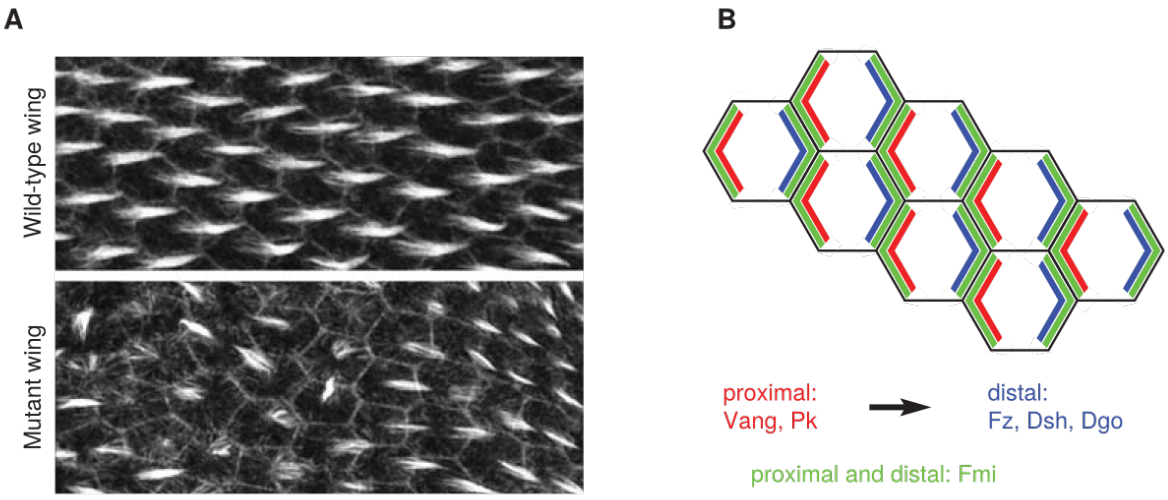

Fig. 1.9 **Planar Cell Polarity in *Drosophila* pupal wing.** a) Images of a wild type (top panel) and PCP mutant in *Drosophila* pupal wing showing disruption of hairs orientation. Actin staining in white to show hairs. b) Asymmetric distribution of PCP core proteins in the fly wing epithelium. Vang and Pk are on the proximal side while Fz, Dsh and Dgo are on the distal side of each cell. Figures from [121]

of this downstream is the activation of Rho A GTPase that is associated with cytoskeletal regulation and so hairs formation and orientation. The bridge between Dhs and RhoA is still not clear [122].

Between PCP proteins, we can differentiate cell autonomously and non-autonomously acting factors. Clone-mutations of Dsh, Pk, Fmi or Dgo protein lead to disruption of hairs orientation in the mutant cells, but not within adjacent wild type cells. By contrast, mutations of Fz or Vang disrupt hair orientations within the mutant and the adjacent cells. For these reasons, the latter proteins are named cell non-autonomously factors. This evidence suggests that Dsh, Pk, Fmi and Dgo do not send signals to the neighbour cells and they are involved only in the interpretation of the PCP signals for the establishment of PCP polarisation. By contrast, Fz and Vang are likely to be involved in the signalling between cells and propagation of the PCP establishment [128]. The genetic studies of PCP mutants in *Drosophila* led to a possible mechanism of the PCP pathway. First, a gradient of Fz is induced by an unknown cue and mechanism. Then each cell is able to compare the absolute value of Fz (or Vang) with the neighbour cells using the non-autonomous proteins (Dsh, Pk, Fmi or Dgo) and so polarise in the direction of the gradient. In this way, each cell can sense its location in relation to the activity gradient and to its neighbours. In *Drosophila*, recent results suggest that the initial cue is given by three Wnt pathway proteins that are well known to interact

with Fz. However, the complete theory of PCP mechanism is outside my aims, and I refer to a recent review for a better understanding [121].

PCP in multicilated cells

Subsequent works in vertebrates determined that homologous PCP proteins are evolutionary conserved. In mammals, PCP-dependent processes include neural tube closure, fur patterning, hair bundle orientation in the inner ear, neuronal migration, and axon guidance [129, 130]. PCP pathway has also been reported to contribute to multiple levels of planar polarisation of multiciliated cells. Specifically, rotational polarity (the alignment of ciliary basal bodies within each cell) and global tissue-level polarity (polarity coordination among all cells across a tissue). PCP proteins such as Dvl or Pk are important for the cell autonomously rotational polarity and reinforce asymmetry and built the structural polarity of the cell. In contrast, transmembrane PCP proteins such as Vangl, Fzd, Fmi or Celsr2, seem to be involved in the tissue-level communication and polarity [131]. In the ependymal ciliated cells, PCP proteins also seem to be involved in the translational polarity, that is the position of the basal bodies within the cell [130].

How polarity information is communicated between PCP proteins and ciliary basal bodies is still under investigation. Recent results suggest that the cell cytoskeleton has a key role [130, 10]. In multiciliated cells, an apical actin network and microtubule filaments connect adjacent basal bodies, ensuring cilia regular spacing, locally coordinating their rotational polarity and protecting them from shear stress [110, 10, 11]. In PCP protein mutants, the subapical actin mesh is disrupted, suggesting an important interconnection between the PCP pathway and the establishment of this cytoskeletal network [132].

1.4.2 Role of hydrodynamic forces in cilia alignment

The PCP pathway is undoubtedly important for cilia orientation. However, past works have shown that cilia of multiciliated cells are also responsive to external hydrodynamic forces, and align their beating directions when physiologically relevant fluid flow is applied during development, Figure 1.10a-e. Specifically, this was demonstrated first in the ciliated larval skin of *Xenopus* [123] and then in mouse brain [125]. The current view is that cilia alignment happens in a two steps process: (i) first a long-range signal breaks the initial symmetry and starts to bias the direction of young cilia [124], (ii) cilia-driven flow enhances the initial polarisation bias and provides a positive-feedback mechanism for the orientation refinement

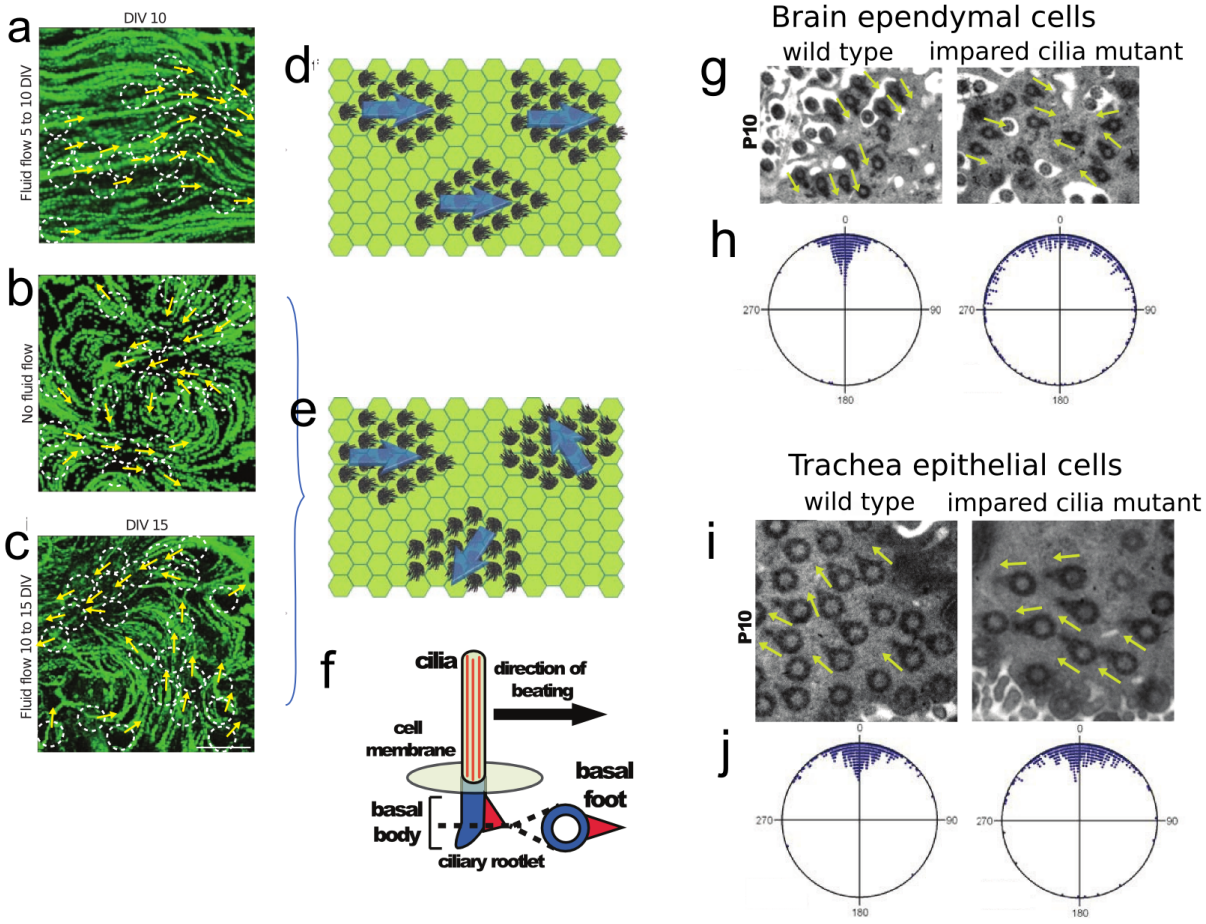

Fig. 1.10 **(a-e) Motile cilia of ependymal cells align with the external flow in a time-dependent manner. (g-l) Cilia motility is important for the alignment of basal bodies in brain ependymal cilia but not in trachea epithelial cells.** a) External flow aligns ciliary beating in ependymal cultures during the early stage of ciliogenesis; flow applied during 5-10 days in vitro (DIV). b)-c) Cilia-driven flow is randomly oriented on tissue scale when (b) external flow is not applied or when (c) external flow is applied but in a later stage of ciliogenesis (10-15 DIV). d) Illustrations of long-range ciliary beating orientation and e) local ciliary beating orientation. Figures from [125]. f) Schematics of cilia and basal foot. The basal foot points toward the direction of ciliary beating. g)-i) TEM sections of P10 brain ependymal cells (g) and trachea cells (i). Rotational polarity was disrupted in mutants with impaired cilia (Ktu $-/-$) in the brain ependymal cells but not in the cells from the trachea (postnatal day 10). Yellow arrows show basal feet directions. h) and l) circular plots of deviation angles of the basal feet. Mean angles are pointed to 0 C°. Scale bars: 10 μm in g) and i). Figures from [133].

[125, 123]. Markedly, the mechanism underpinning these two steps was reported not to be universally conserved. Here I will review the cilia alignment processes in *Xenopus* larvae

skin, mouse airways and brain ventricles.

In *Xenopus* larvae skin, the outer non-ciliated epithelial cells provide a directional cue along the tissue axis for the orientation of intercalating ciliated cells through a Planar Cell Polarity (PCP) dependent pathway [124]. The initial polarisation bias could be caused by polarised strains during gastrulation. This idea is supported by recent works showing that mechanical forces can influence PCP orientation by a mechanism dependent on microtubules rearrangement in response to high tissue strain [134]. After this polarisation, while cilia are still growing, the cilia self-generated fluid flow is sufficient in refining the beatings orientation along the tissue axis [123].

In mouse airways, when cilia appear, PCP proteins have already reached their maximum observed asymmetry and basal bodies show significant orientation in the proximal (oral) direction [10], independently on cilia motility [133], Figure 1.10i-l. The polarisation signal that leads this initial orientation is not known [131], although mechanical cues such as fetal breathing flow and strains happening during embryogenesis could be involved [10, 135, 136]. After the initial bias in basal body orientations, it is in debate whether cilia driven flow acts in the process of direction refinement. Short-term air shear stresses induced no orientation of ciliary beating in airway cultures [137]. In mice, when segments of the trachea are transplanted with inverted direction, neither the PCP pathways or cilia orientation aligns with the surrounding regions of normal trachea [138]. These experiments suggest that cilia in the airways are not responsive to flow, however more direct evidence is still missing.

By contrast, in the brain ventricles, when cilia first dock to the cell membrane, they do not have a pre-patterning bias [125, 133] and basal bodies are randomly oriented. In the brain ventricles, the initial cue that breaks planar symmetry is supposed to be mechanical: the pressure gradient that arises from CSF secretion in the choroid plexus and absorption in the foramen of Monroe [139]. CSF secretion is described in Section 1.2.2. This hypothesis is motivated by the fact that randomly oriented ependymal cilia align their beating directions when fluid flow is applied during their growth [125], Figure 1.10a-e. Successively, but still during *ciliogenesis*, cilia direction would be refined by hydrodynamic forces between cilia themselves, similarly to *Xenopus* larvae skin.

In the brain, it seems that PCP proteins are not involved in giving a start cue as in the airway and Xenopus, but to lead the permissive response of basal bodies to hydrodynamic forces and consequent ciliary beating alignment [125]. As evidence, ciliary mutants with impaired beating were reported to have cells with basal bodies pointing in random direc-

tions, showing complete absence of cell alignment, Figure 1.10g-h, although PCP proteins display proper asymmetric distribution [125, 133]. However, PCP protein Vangl2 mutant cultures exposed to flow did not show any preferential beating direction, showing that the PCP pathway is required for the response to flow [125]. Markedly, the interplay between hydrodynamic forces and PCP was measured to happen only in a definite time-frame. After complete *ciliogenesis*, no significant alignment was measured in ependymal culture exposed to shear stress, suggesting that cilia beating directions are locked after complete maturation [125], Figure 1.10a-e.

Overall, the emerging scenario is that cilia alignment is achieved during their growth with an interplay of PCP and hydrodynamic forces with a degree that varies between organs. In the airways, cilia orientation follows the defined axis of the proximal-oral direction, and it seems driven by PCP polarisation [10]. Hydrodynamic forces are thought to only play a role in the orientation refinement [133], although in a recent study cilia did not align with short periods of air shear stress [137]. By contrast, in the brain ventricles, where the cilia flow network is much more complicated and does not have a defined axis set by the tissue [39], hydrodynamic forces rule cilia orientation [125]. How such structurally similar cilia can respond so differently to flow and to the PCP pathway is still unknown.

1.5 Research questions

Cilia alignment and coordination are fundamental for many physiological roles in microorganisms and mammals. However, the mechanism underpinning the emergence of such collective behaviour is still on debate. Previous works mainly focused on algae and protists, highlighting possible organism-dependent mechanisms for cilia coordination. Although cilia structure seems to be conserved in nature, microorganisms seem to have developed different mechanisms for cilia/flagella synchronisation: hydrodynamic forces are not enough for the synchronisation of some algae [88, 65, 87], while in others hydrodynamic coupling seems still the basic mechanism of coordination [85, 87]. Given these organism-dependent mechanisms, experimental studies addressing the role of hydrodynamic forces in synchronisation and alignment of mammalian cilia are now particularly valuable. They can provide significant progress in the diagnosis and treatment of human medical diseases related to the lack of cilia coordination. This thesis mainly focuses on studying mammalian ciliated organs such as brain and airways. The specific research questions that I will address in this thesis can be summarised in:

- Are the hydrodynamic forces between motile cilia sufficient to be the mechanism leading cilia synchronisation in the brain?
- What is the role of external flow and cilia-driven flow in the emergence of collective cilia alignment in the airways and the brain?

The first question will be addressed in Chapter 3, while the second one will be tackled in Chapter 4 and Chapter 5, using respectively brain and airways cell cultures.

Chapter 2

Transwell-chip: a novel device for applying shear flow to cells at ALI

The concept of recreating organ-level functions inside a microfluidic chip has attracted massive interest from pharmaceutical companies and scientists in the last decade [140]. From the combination of bio-engineering and microfluidics, the biological functions of organs, such as blood vessels, muscles, airways, liver, brain, gut, have been mimicked on chips with the potential to markedly transform the drug discovery market by reducing tests on animals and unpredicted drug-induced toxicity [140]. This recent technology was called organ-on-a-chip by Donald Ingber, who developed in 2010 a microfluidic chip able to reconstitute the alveolar-capillary interface of the human lung, including mechanical strains induced by breathing [141].

All cells and tissues in our body are continuously subjected to mechanical forces that are likely to modify cell behaviour [142]. One of the advantages of organ-on-chip technology is that cells can be grown in microfluidic devices that allow to mimic these forces and so recreate a realistic *in vitro* system. For example, vascular endothelial cells are constantly exposed to blood shear stress. When these cells are grown in micro-channels and exposed to external shear stress, they start to elongate in the direction of the fluid flow [143], displaying a morphology similar to the one *in vivo*. Airway epithelia are always exposed to shear and strain stresses caused by breathing: air-liquid two-phase microfluidics was used to mimic lungs breathing. It was found that breathing enhances epithelial and endothelial uptake of nanoparticulates in the airways and stimulates their transport into the below microvascular channel [141].
Most notably for the aim of this thesis, ciliated epithelia in mammals are also exposed to viscous shear stresses coming from internal sources or by nearby cilia. The organ-on-chip

technology promoted the development of many techniques that can be used to study the response of mammalian cilia to flow [137, 123, 125]. For these reasons, I specifically focused on developing a microfluidic device that could be used for applying flow on both brain and airway cells.

A novel organ-on-chip inspired device for brain and airway cells

Airway cell cultures are particularly challenging in microfluidics because they require cells to be grown in the air-liquid interface for a correct differentiation [144]. In the last decade, many lung-on-chip models have been developed that permit to reproduce lung functions and apply shear forces [145, 141, 146, 147, 137]. An example is the already mentioned two-phase microfluidic chip from Wyss Institute [141, 146, 147], Figure 2.1a-b.

Although it is a landmark for the organ-on-chip technology, this device has the big disadvantage that needs constant media perfusion due to the limited nutrients that the small channels can host. Continuous perfusion of media complicates the every-day culture significantly. It requires that the chips are always connected to a source of medium flow, such as a syringe or peristaltic pump. Moreover, constant media perfusion represents a source of experimental noise when studying the effect of shear stress in the defined time-window of cell differentiation. Other two-phase devices for airway cultures are also available commercially; however, these companies often tend to use plastic substrates that largely limit the permeability of fundamental gas such as oxygen and CO_2. A recently developed two-state chip that does not require constant medium perfusion and does not have gas permeability problems is composed of a combination of polystyrene and adhesive components incorporated into a 6-well filter membrane insert [137], Figure 2.1c. This device has been used to apply 24-hour shear stress on airway cells successfully. The disadvantages are a complicated manufacturing process and that cells can not be imaged without disassembling the device. In past works, the shear flow was applied on ependymal cultures grown in wellplates using rotating plates [125, 11] that did not allow homogeneous flow and caused contamination problems on many samples, Figure 2.1d.

Combining the ideas from [146, 137] I developed a novel chip using a Polydimethylsiloxane (PDMS) channel bound to the membrane of a Corning Transwell insert, that I have called Transwell-chip. The manufacturing process is described in Section 2.1. The medium in the basolateral compartment reaches the cells through the pores of the membrane and acts as a nutrient reservoir. This extra-medium allows long-term culture and differentiation without the need for media perfusion. Differently from [137], the top chamber is made of PDMS

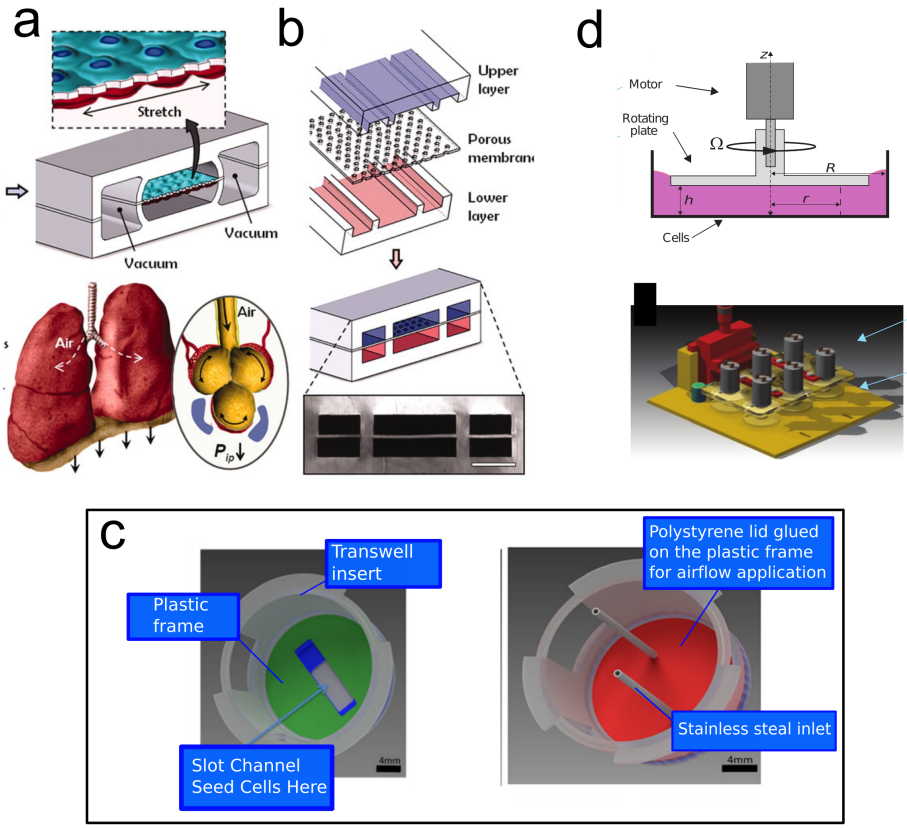

Fig. 2.1 **Devices and setups for shear stress application on ciliated cells of airways and ependyma.** a) The biologically inspired design of a human breathing lung-on-a-chip microdevice. The compartmentalised Polydimethylsiloxane (PDMS) microchannels are used to form an alveolar-capillary barrier on a thin, porous, flexible PDMS membrane. The device recreates physiological breathing movements by applying vacuum to the side chambers and causing mechanical stretching of the PDMS membrane forming the alveolar-capillary barrier. (b) The device is composed of three PDMS layers irreversibly bonded to form two sets of three parallel microchannels separated by a 10 μm-thick PDMS membrane. Scale bar, 200 μm. Figures from [141] (c) Assembly of the device developed by [137] for applying shear stress on ALI cultures. A Polystyrene disc with a channel feature (plastic frame) is attached to a porous polyester membrane (Costar Transwell 0.4 lm Permeable Support) using the silicone adhesive transfer tape. Cells are grown in this open channel. The image is on the left. When cells are ready for airflow shear stress, a polystyrene lid layer is then attached to the frame layer, thus completing the fluidic channel and allowing the perfusion of airflow. (d) Setup for applying physiological-like shear stress on ependymal cultures in wells. Each motor rotates a circular plate dragging the medium in its rotation and creating a shear flow over cells [125]. Illustration of 6 similar units applied to a 6 well-plate.

that offers many advantages for microfluidic cell culture because of its gas permeability, optical transparency, and flexibility. PDMS has been used for the last decades for long term

culture and cell differentiation of many cell types [148, 149]. The culture of airway cells in the Transwell-chip is described in Section 2.2.2. The setups that we use to apply fluid and air shear stress are described in Section 2.3.

2.1 Fabrication of the Transwell-chip

Briefly, Transwell-chip is composed by a Polydimethylsiloxane (PDMS) substrate with channel feature bond to the membrane of a Corning Transwell Insert. We used PDMS prepolymer as glue to bond the PDMS substrate and the porous membrane [150].
Corning Transwell inserts are permeable supports for cell culture with ten μm-thick polyester membranes that are tissue culture treated for optimal cell attachment and growth. We used Transwell inserts with 0.4 μm pore polyester membrane (24 mm diameter) that are commercially available from Sigma (ref number CLS3450), see Figure 2.2c.

The fabrication of a Transwell chip can be divided into three steps:

1. **Fabrication of PDMS substrate with channel feature.** PDMS prepolymer (Sylgar 184 Dow Corning) is mixed with curing agent at a weight ratio of 12:1 and left in a vacuum desiccator for 1 hour to remove bubbles. The mixture is then cast onto an aluminium mould having positive reliefs of the desired channel shape and cured at 60^oC overnight. The channel has 1 mm width, 1 mm height and 12 mm long. The moulds are produced by CNC mill machining, but also soft-lithography can be used. The cured PDMS layer is peeled from the aluminium substrate. Then, holes of 2 mm diameter are punched through the cured PDMS substrates at the end of the channels to obtain a PDMS slab with channel features, Figure 2.2a. The obtained PDMS substrates can be stored in a clean container for months.

2. **Generation of a thin uncured PDMS prepolymer layer.** Uncured PDMS prepolymer (ratio 10:1) is spin-coated on a clean glass rectangular cover slide (25x75mm^2) for 10 s at 500 rotation per minute (rpm), and then at 3000 rpm for 60 s (ramped at 500 rpm/s) to generate a thin layer of uncured PDMS with thickness around 20 μ m [150], Figure 2.2b.

3. **Permanent bonding of the PDMS substrate with the porous membrane of a Transwell insert.** The PDMS substrates with channels are placed onto the PDMS-

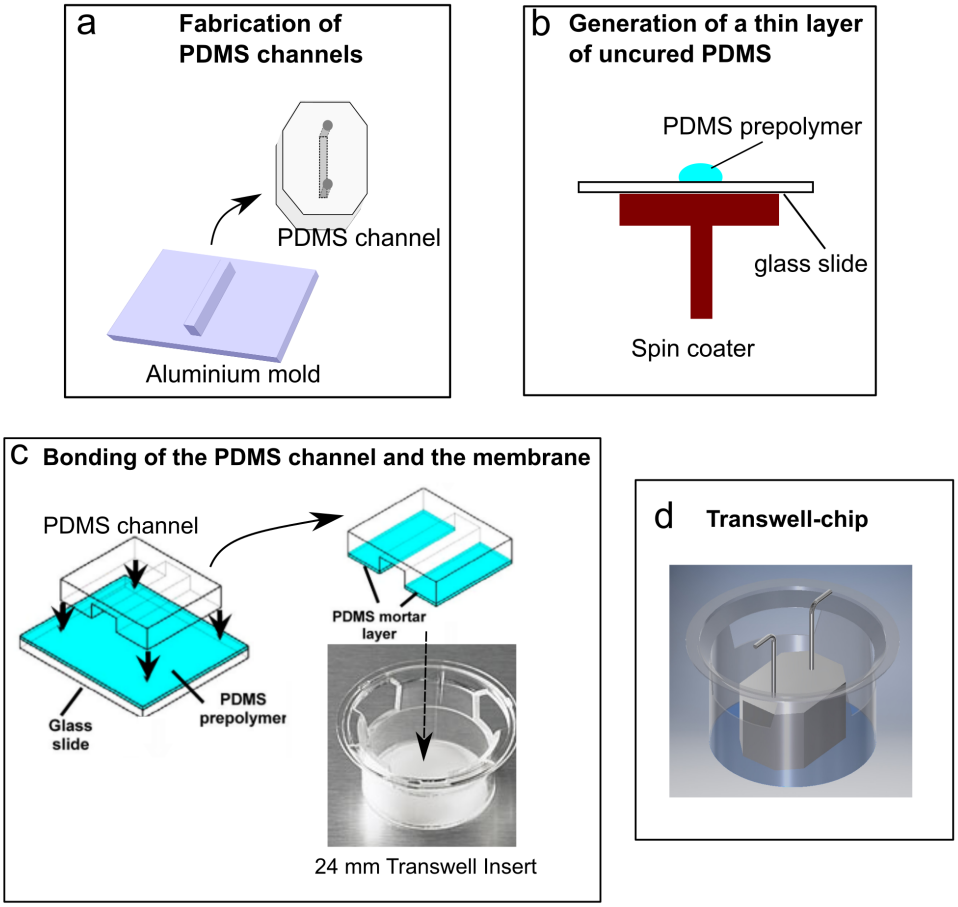

Fig. 2.2 **Devices for shear stress application on ciliated cells of airways and ependyma.** a) Uncured PDMS mixture is cast onto an aluminium mould and cured at 60^{o}C overnight to have PDMS channel slabs. (b) Uncured PDMS prepolymer (ratio 10:1) is spin-coated on a clean glass rectangular cover slide to generate a thin layer of PDMS prepolymer. (c) The PDMS substrates with channels are placed onto the PDMS coated glass slides and allowed to stay in contact for 30 s. This creates a thin mortar layer of PDMS prepolymer on the surface of the PDMS channels. Then each PDMS substrate is gently placed on a Transwell Corning insert. The combined pieces are left to cure at room temperature for at least 2 days in 6 well plates to completely bond. (d) At the end of the process, two short pieces of tubing are placed at the inlet and outlet of the channel. Illustration of the Transwell-chip. Figure c) has been adapted from [150].

coated glass slides and allowed to stay in contact for 30 s, Figure 2.2c. Each PDMS substrate is removed from the coverslip and gently placed at the centre of the 24 mm polyester membrane of a Transwell insert (CLS3450-24EA, Sigma) using tweezers. The combined pieces are left to cure at room temperature for at least 2 days in 6 well plates, Figure 2.2c. Higher curing temperature would result in melting of the glue between the membrane and the insert. After the PDMS and the Transwell inserts are completely bond, two short pieces of tubing (0.50" outside diameter (OD) ,WZ-06419-01 Coleparmer) are placed at the inlet and outlet of the channels to facilitate the entrance of fluid using pipettes (we recommend 100 and 1000ul pipette tips), Figure 2.2d. Before seeding the cells, the complete Transwell chip is sterilised by UV irradiation for 40 minutes.

2.2 Protocols of cell culture in Transwell-chip

2.2.1 Differentiation of ependymal cells

Ependymal cells are isolated from young mice immediately after birth (postnatal day 0, P0) up to three days later (P3) [151]. The cells are first expanded until they reach confluence (around 4 to 5 days) and then subsequently plated in the Transwell-chip in which they differentiate and grow multiple motile cilia (reaching 70,80% ependymal cells within 15 days). All animal studies were performed in accordance with the guidelines of the European Community and French Ministry of Agriculture and were approved by the Ethics committee Charles Darwin (C2EA-05) and "Direction départementale de la protection des populations de Paris" (Approval number Ce5/ 2012/107; APAFiS # 9343) [151, 125].

Differentiating ependymal cells are isolated from mouse brain and grown in flask T-25 as previously described [151] from Spassky's group in Paris. After 3 days, the flasks are tightly closed and sent to Cambridge in a box at room temperature. Upon arrival, flasks are placed in a conventional incubator with fresh medium (Dulbecco's Modified Eagle's Medium (DMEM)/Glutamax with 10% fetal bovine serum (FBS) and 1% penicillin-streptomycin (P/S)). When cells are 70-80% confluent, the flasks are close tightly and shaken overnight on a rocker at 200 rpm outside the incubator. Each flask is wrapped in aluminium foil, and the cap is covered with parafilm to avoid media leaking and contamination. This step is essential to detach other types of cells but ependymal (mainly differentiated oligodendrocytes and neurons). The same day, Transwell chips are sterilised under UV and coated with PLL solution 320μg/ml in milliQ water (SIGMA Poly-L-Lysine Hidrobromide P1524) over-night

in the incubator, then rinsed 3 times with sterile water and left to dry under the hood for 1 hour.

Successively the media is removed from the flask and cells are rinsed with phosphate buffered saline (PBS, calcium and magnesium-free) for 3 times. 1 mL of Trypsin-EDTA solution is added for each T-25 flask for less than 5 min in the incubator, and then 1 ml of complementary FBS is added to neutralise trypsin. Then, cells are centrifuged at 110g for 7 minutes and resuspended in DMEM/Glutamax medium with 10% FBS and 1% P/S at a concentration of 10^7 cells/ml. Cells are seeded in the Transwell-chip inlet using 100ul pipette with the help of tweezers to hold the inlet tubing. The day after, the cells are rinsed with phosphate buffered saline (PBS), and the medium is switched to 1% P/S DMEM medium. Medium is not changed during the period of differentiation. After 15 days, cells are fully differentiated, Figure 2.3e-h.

2.2.2 Differentiation of airway cells

Human and mouse airway stem cells, respectively hAECs and mAECs, can be isolated from fresh human tissues, lung biopsy, and mouse trachea and successively expanded in culture flasks, Figure 2.3a. Differentiation into secretory and ciliated can be induced using air-liquid interface (ALI) culture. The air-liquid interface is achieved by culturing cells on top of a porous membrane. Cell medium is placed below the membrane, while, above the membrane, cells are exposed to air. The nutrients from the cell medium reach the cells through the pores of the membrane. The differentiation process takes between 14 to 45 days from the air-liquid interface establishment, respectively for mice and human airway epithelial cells [152]. Standard air-liquid interface culture is summarised in [153]. For the culture of airway cells in Transwell-chip, we adapted the protocol from [147].

Already isolated primary hAECs are obtained from commercial suppliers (Epithelix, Switzerland). Mouse stem cells or human airways cell line KT were provided by F. McCaughan's lab [154, 155].

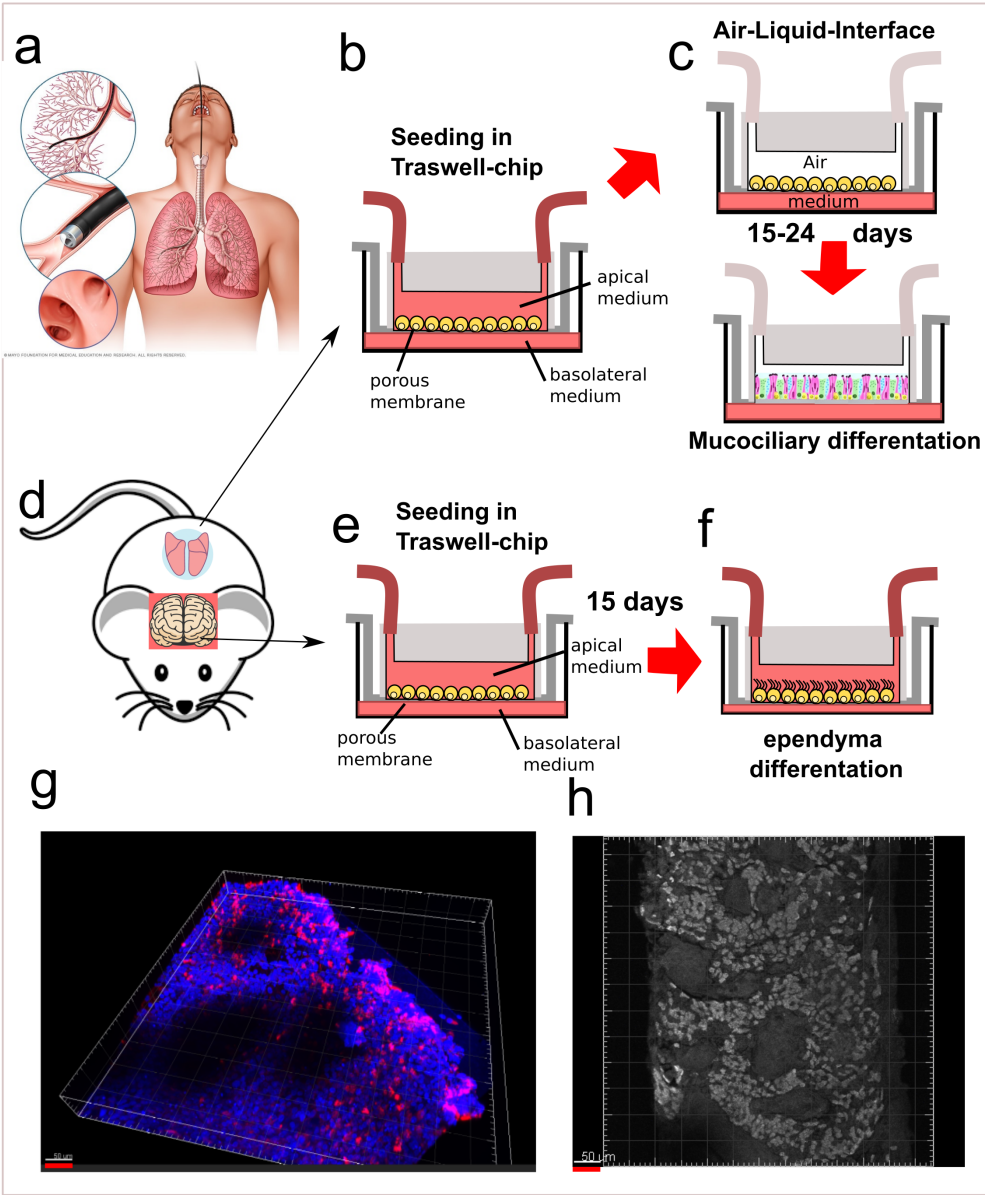

Fig. 2.3 **Culture of the airway and ependymal cells in Transwell-chip** a) Human and mouse airways stem cells can be isolated from fresh human tissues (or biopsy) and (d) mouse trachea. (b) After expansion in flasks, cells are seeded into the Transwell-chip at very high concentration. (c) After 2-3 days, the apical medium in the channel is removed so that cells are in an air-liquid-interface that trigger cell differentiation. Mucociliary functional epithelia are established after 2 and 4 weeks from the air-lift respectively for mouse and human cells. (d) Ependymal cells are isolated from mouse P0-P3 brain and grown in flask T-25 upon 70-80% confluency. (d) Successively cells are seeded into the Tranwell-chip at very high concentration. (e) The day after the medium is replaced with differentiation medium and cells are left in the incubator without changing the medium. After 15 days, ependymal cells are fully differentiated and have beating cilia (f). (g) KT human airway cell line differentiated in the Transwell-chip. Staining of cilia in red (Acetylated α-Tubulin) and nuclei in blue (Dapi). Image acquired with confocal microscopy. Holes in the epithelium are due to the heterogeneity of the epithelium height. (h) Mouse primary airway cells differentiated in the Transwell-chip. Staining of cilia in white (Acetylated α-Tubulin). Figure obtained with confocal imaging.

Basal cells are expanded in 75-cm^2 tissue culture flasks using airway epithelial growth medium supplemented with growth factors and supplements until 70-%80 confluent.
We used BEBM (catalog no. CC-3171) for primary human cells, Keratinocyte-SFM (1X) (Life Technologies) for KT cell line [156], Pneuma Cult Ex (Stem cell 05008) for mouse cells. Please refer to [152, 154] for media preparation protocols. Before cell seeding, the porous membrane of each Tranwell-insert is coated with rat tail collagen type I (300 mg/ml; Sigma) at 37 °C for 24 h. Airway cells are then trypsinised, (see [147] for more details) and seeded onto the chip at a concentration of 10^7 cells/ml using 100μl pipette tips and allowed to attach under static conditions, Figure 2.3b. Three hours later, cultures are washed with fresh medium and maintained in a submerged state for 2 days. Successively, the apical medium in the channel is gently aspirated to establish an air-liquid interface (ALI), that, in turn, it will trigger differentiation, Figure 2.3c. The medium in the basolateral compartment of the Transwell-chip is replaced with differentiation media (StemCell Pneumacult-ALI with supplements [152, 154]). Medium is changed every other day, and the channels are rinsed once weekly with PBS to remove debris and mucus accumulation. Mouse and human epithelial cells formed a stable and terminally differentiated ciliated epithelium within 2-3 weeks and 3-5 weeks respectively after being placed under an ALI, Figure 2.3c. The cilia expression was assessed by staining Acetylated α-Tubulin, Figure 2.3g-h, and by high speed bright field imaging to confirm the activity of beating cilia on the cell surface.

2.3 Measuring the shear stress in microfluidic channels

Media perfusion can be used to expose cells grown in microfluidic channels to shear stress. The no-slip boundary condition assumes that the flow speed is zero at the surface of the cells in the channel, while at some height from this boundary the flow speed must equal that of the fluid. Shear stress on the cell surface arises as a result of this loss of fluid velocity. Assuming a constant flow of a Newtonian fluid moving along the x-direction, and a no-slip surface at the plane $z = 0$, the shear stress τ can be calculated with the following expression:

$$\tau = \eta \frac{\partial u_x}{\partial z}\bigg|_{z=0}, \tag{2.1}$$

where η is the viscosity of the fluid. Then, in principle, one can find the shear on the cells surface by knowing the velocity profile in the channel. Fluid speed can be calculated using the equation governing the motion of fluids, namely, the Navier-Stokes equations [158]. An example of the exact solution to this equation is the flow speed in a circular channel (laminar flow): flow profile is parabolic and it reaches the maximum speed at the centre of the channel,

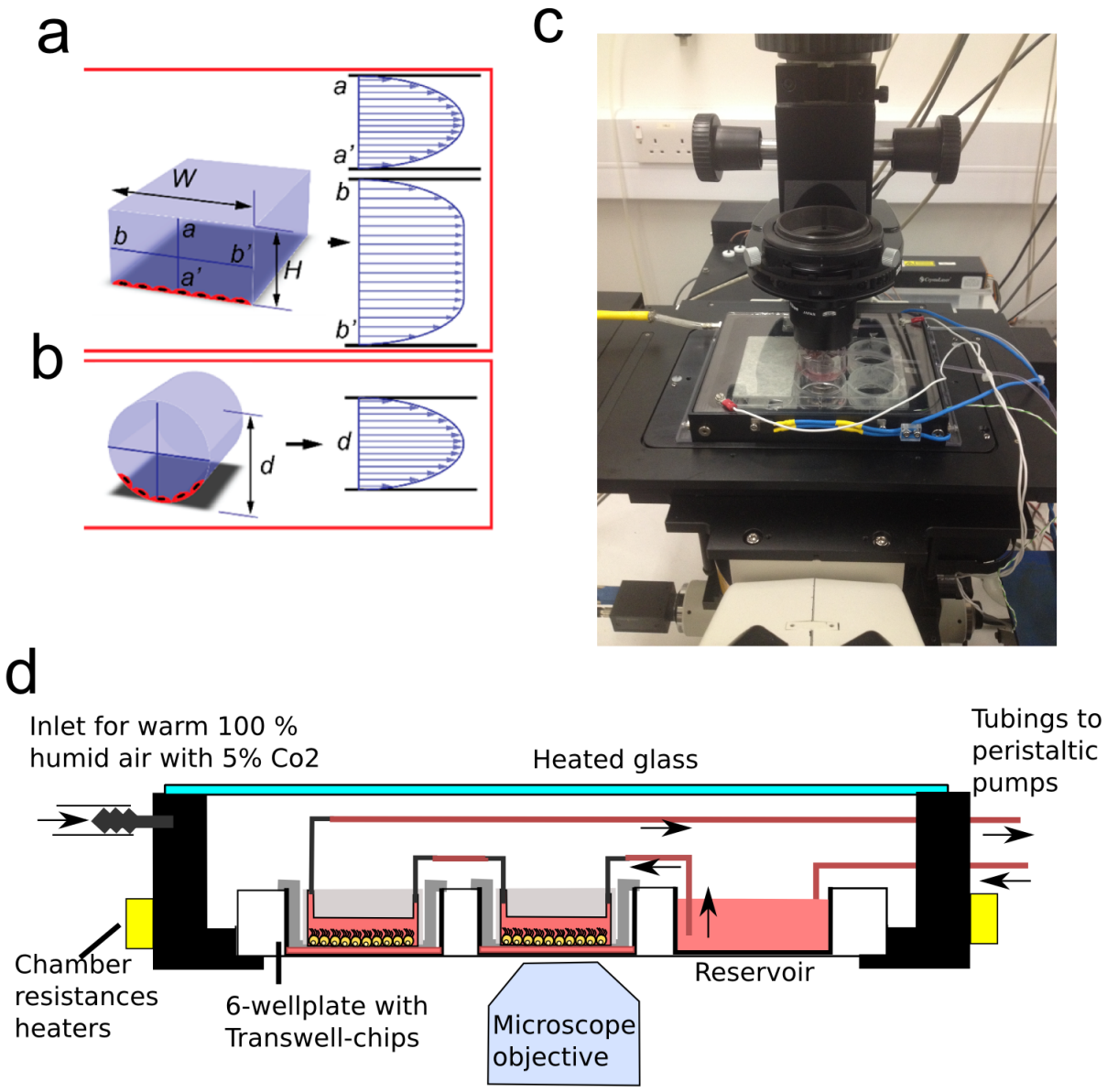

Fig. 2.4 **Illustration of microfluidic setups to apply shear stress in the Transwell-chip** a) Flow profile in a rectangular channel with a high aspect ratio. The flow speed across the larger dimension increases close to the surface and then remains roughly constant in the central part of the channel. (b) Flow profile in a circular tube is instead parabolic. Pictures (a)-(b) from [157]. (c) Picture of the cell-chamber designed by Dr Kotar hosting a wellplate and mounted on an inverted microscope. (d) Schematic of the cell-chamber during constant media perfusion. The chamber can hold a 6-wellplate and can keep the plate at the optimal cell-culture conditions while imaged on the microscope. The chamber is constantly perfused with air at 37 °C, 100% humidity and 5% CO_2. The inside temperature is regulated by resistors on the chamber side and kept stably at 37 °C by a feedback proportional-integral-derivative (PID) controller. The top glass is also heated to avoid air condensation on the glass. Few holes in the chamber allow the tubing to pass through and to connect the outside pumps with the Transwell-chips. This schematic represents the typical setup for constant fluid perfusion, where the medium is pushed by the peristaltic pump to the reservoir in a well of the plate and then flows into the Transwell-chip channels.

Figure 2.4b. For a flow rate Q in a channel of diameter d, the flow speed at distance r from the pipe centre is:

$$u_x(r) = \frac{8Q}{\pi d^2}\left[1 - \left(\frac{2r}{d}\right)^2\right].$$

However, in the case of microfluidic devices, the channels are rectangular. In the case of a rectangular channel of width w, and height h, the analytic solution for the flow speed profile involves infinite series functions of z and y, where z is the coordinate along the height and y is the one along the width [159]. Qualitatively, the velocity distribution along the smaller dimension displays a parabolic distribution. In contrast, across the larger dimension, the velocity increases close to the surface and then remains roughly constant in the central part of the channel, Figure 2.4a-b. An exact expression for the shear stress in a rectangular channel can be found in [157]. When considering high aspect ratio channels, where the width is much larger than the height ($w >> h$), the flow can be approximated to the one between two infinite plates. In this simple scenario, the flow profile is parabolic. Then the shear stress can be calculated as a simple function of the width and height [160]:

$$\tau = 6\eta\frac{Q}{h^2 w}. \tag{2.2}$$

For channels with $h = w$, the difference between the shear stress obtained with this formula and the exact one is around 13% at the channel centre, [160]. The above formula highlights that shear stress on cells cultured in rectangular channels (such as Transwell-chip) can be tuned by both varying the flow rate and the channel geometry.

2.4 Novel setups to apply shear stress on airway and brain cells

Cilia and cells response to shear stress can be immediate [65, 106] or may require longer times, as in the case of cilia alignment with external flows in *Xenopus* and mouse brain [125, 123]. In both situations, the medium perfused for the shear stress application must be kept at 37 °C and the right pH to maintain optimal conditions of cell culture. This condition can be generally achieved by placing the microfluidic devices in a conventional incubator or using custom chambers where the temperature and the 5% CO_2 is controlled [161]. In our lab, Dr Jurij Kotar developed a versatile cell-chamber that can be mounted on the stage of an inverted microscope. The internal temperature of the chamber and CO_2 can be controlled through computer software. The cell-chamber can host a wellplate; therefore, up to 6 cultures

(Transwell-chips) can be maintained alive in optimal conditions and imaged with microscopy, Figure 2.4c-d. In this section, I will describe the setups that we have developed to apply constant and oscillatory fluid flow and airflow on cells cultured in Transwell-chips.

2.4.1 Constant shear flow setup

We developed a versatile setup where shear stress of variable magnitude could be applied for periods such as days on ciliated airway and brain cells. Long media perfusion can be driven using many techniques, such as gravity, syringe or peristaltic pumps. We chose a peristaltic setup because it allows having a recirculating medium: the cells secret factors that are diluted into the total culture media volume and recirculate back to the cells [161]. This setup is particularly indicated for ependymal cells where culture protocols suggest not to change the medium during differentiation [151].

In a microbore tubing, the medium is pushed from the peristaltic pump to a medium reservoir, that in our case is inside one of the wells of the wellplate hosting the Transwell-chips, Figure 2.4d. This wellplate is kept at 37 °C and the right pH either in a conventional incubator or in the cell-chamber. By contrast, the pump is placed outside because high humidity can damage the pump components, Figure 2.4d. From the reservoir, the medium flows through all the Transwell-chip connected in series in the wellplate. All the connections between reservoir and Transwell-chips are made using microbore tubing and stainless-steel interconnections. The upstream reservoir ensures that the perfused medium is always at the right temperature and pH before flowing into the chips. The medium is eventually pushed back to the peristaltic pump placed outside through a long tubing, and then pushed again to the reservoir in a continuous fashion, creating a recirculating system. A chip in the wellplate is usually not exposed to flow and works as a control. The flow rate of the perfused medium, and so the shear stress on the cell, can be tuned by changing the velocity of the peristaltic rollers. Illustrations of the setup can be found in both Figure 2.4d and Figure 2.5a-b.

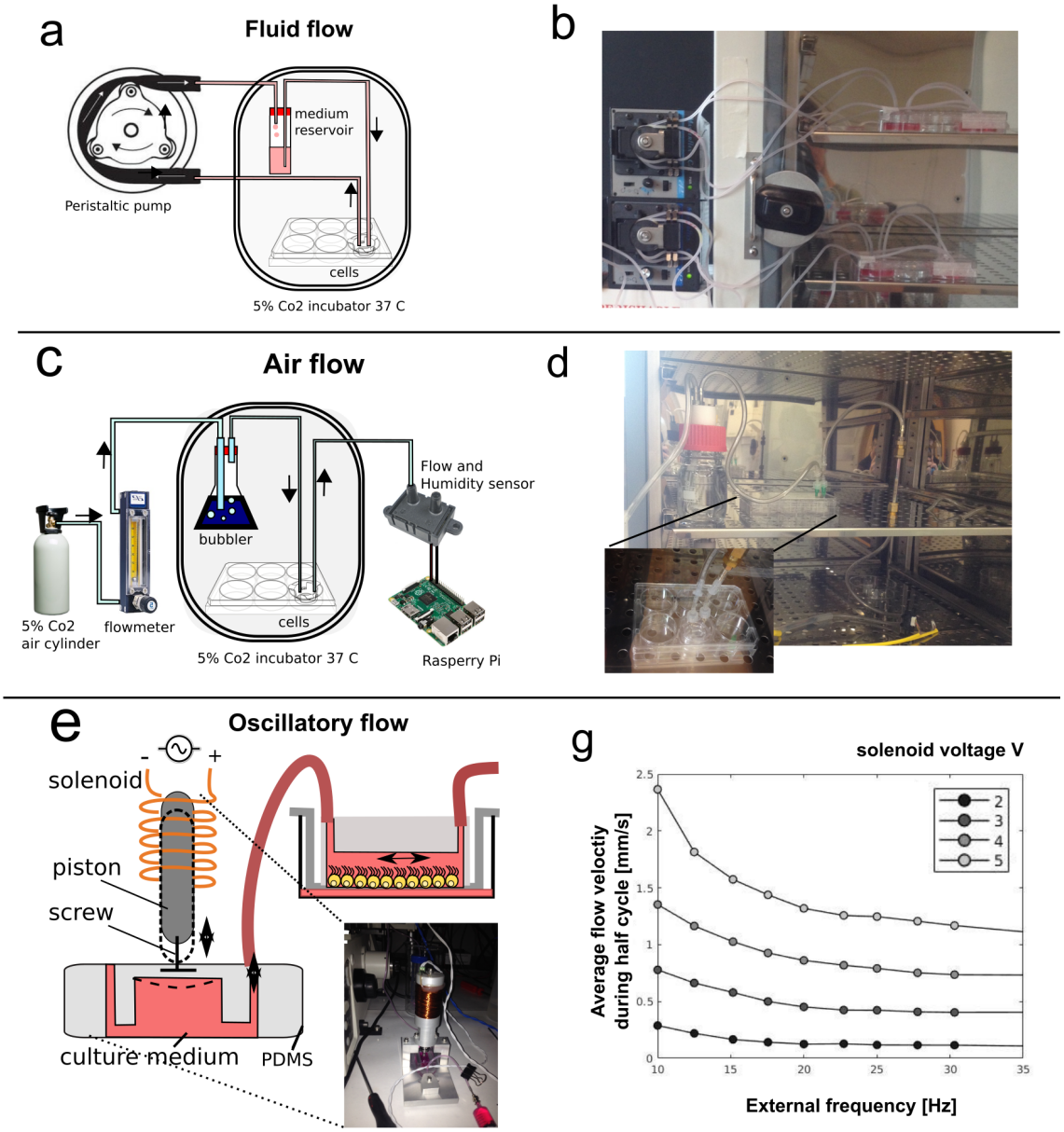

Fig. 2.5 **Illustration of microfluidic setups to apply shear stress in the Transwell-chip.** a) Illustration of the constant shear flow setup. (b) Picture of the setup with cultures in the incubator. (c) Illustration of the airflow setup. (d) Picture of the setup with zoom on tubing connections between the air flow-system and the Transwell-chip. (e) Schematic of the solenoidal pump for the application of oscillatory flow in the Transwell-chip. (f) Picture of the solenoidal pump. (g) Flow created at the centre of the Transwell-chip when a defined signal of amplitude V and frequency (external frequency) was applied at the voltage to a current converter that is connected to the copper wire of the solenoidal pump. Flow in the channel has been calibrated using 1 μm beads; we report the flow at the defined distance of 7 μm from the surface.

Materials and protocol

Suggestion to avoid bubble formation: Air bubbles in microfluidic systems are one of the major problems of long term perfusion systems. Air bubbles nucleation has been suggested to arise spontaneously from defect sites, such as the interconnections between PDMS and tubing, or tubing-tubing connections. The shear stress caused by an air bubble flowing in a small channel can be much larger than the one without bubbles, and it is detrimental to cell viability [162, 163]. To prevent bubbles formation, I have found particularly useful (i) pre-priming the tubing system with low surface tension liquids such as ethanol, (ii) placing the reservoir upstream of the cell culture and taking the medium from the bottom of the reservoir [161]. Bubble-traps from commercial companies did not increase cell viability of my experiments significantly.

Tubing preparation and priming: Here, I will describe how to prepare and clean the tubing system for long term media perfusion on Transwell-chips. Prior experiments, the tubings and connectors composing the system must be sterilised and cleaned with ethanol. A segment of approximatively 20 cm of peristaltic tubing (Masterflex Microbore, Puri-Flex Autoanalysis Tubing, 26, 0.89mm ID) is connected with two microbore tubings of 0.50" OD (WZ-06419-01 Coleparmer) using 18 gauge straight connectors (FIS5601087 Intertronics). Short microbore tubing segments are also connected in series to one of the ends of the system through 90-degree bend connectors (18 gauge). After priming step, these connectors will be used to connect the inlet and outlet of Transwell chip with the setup. The number of these short segments depends on the number of chips to connect in series. The peristaltic tubing is placed into the peristaltic pump slot, and the two ends of the tubing are inserted in the priming-reservoir chamber filled with ethanol. The reservoir for this priming step can be made using a falcon tube with two holes on the lid for the inlet and outlet of the tubings (the holes can be easily made with sharp tweezers). The priming is performed at the maximum flow rate for 1 day at room temperature. Successively, the system is rinsed for 2 hours at least by replacing the ethanol in the reservoir with the sterile water.

Cell plate preparation: Up to five Transwell-chips are placed in a 6-well plate with glass bottom. One well is filled with 8ml of medium and acts as the medium reservoir, Figure 2.4d. Each Transwell-chip is tightly held in the well using sterile tape (AreasSeal film, A9224-50EA). A well-plate lid with two holes of 3mm (diameter) above each well is placed on top of the plate. The plate is then placed into the clean cell-chamber. The tubing system is disassembled and assembled in the biological hood. The complete setup is moved to the microscope room, and the cell chamber is placed on the microscope stage.

The cell-chamber is then heated with custom software and perfused with humid and warm air with 5% CO_2 from a gas cylinder. Alternatively to the use of a cell-chamber, the plate with all the connected tubing can be placed inside an incubator with the peristaltic tubing segment outside, Figure 2.5b. The peristaltic tubings outside the chamber or the incubator are connected to the peristaltic pump, and media perfusion is initiated. At this stage, the medium flows only into the tubing system, without the Transwell-chips connected, and it is kept going for 4 hours. This allows additional priming of the tubing with the medium to avoid bubbles formation. Finally, the Transwell-chips inlets and outlets are included in the recirculating medium system using bend connectors (with particular care not to introduce bubbles), and fluid perfusion also starts in the chips. After the long-perfusion (no more than 3 days), the Transwell-chips are disconnected from the setup and are ready for Bright Field and Fluorescent imaging with tracer particles.

2.4.2 Oscillatory fluid flow setup

In order to produce a setup similar to [65], with the help of Dr Kotar we designed a pump able to drive an oscillatory sinusoidal flow with defined frequency and velocity magnitude, and that could be connected to a Transwell-chip, see Figure 2.5e. The inlet of a Transwell insert is connected through tubing to a PDMS chamber filled with fresh medium. An alternating flow of medium is created when the top membrane of the elastic chamber is moved up and down by a piston. The oscillations of a soft iron piston are controlled by the magnitude and frequency of alternate current (AC) flowing into a solenoid copper coil around the piston and a preloaded spring in a similar fashion to commercially available solenoidal fluid pump, Figure 2.5e-f. While the frequency of the signal sets the frequency of the oscillating flow, the amplitude of the signal rules the flow speed. The solenoid is made by wrapping copper wire (0.5 mm) 300 times around an aluminium case that host the soft iron piston and the spring. The piston is tightly connected to the top membrane of the PDMS chamber through a screw which end is embedded in the PDMS. The PDMS chamber is 5 mm height and with top area 10 mm x 10 mm. The alternate current is created by a function generator connected to a current drive source. The output current is monitored with oscilloscope through a current proportional voltage output. This setup allows external flows spanning in a broad range of frequency and flow velocity v_{EX} (average during half cycle) from 200 μm/s to 2 mm/s. The friction of the plug with the surrounding material sets the minimal flow speed while the maximum speed is constrained by the highest current that could be generated by the voltage-to-current converter.

Flow speed calibration. We tracked 1 μm polystyrene tracers particles to measure the flow and frequency created by the solenoidal pump into the Transwell insert as a function of the frequency and amplitude of the input signal. The calibration was performed in a Transwell-chip without cell. Recordings of the oscillating particles were taken at 500 fps and with 40X NA 0.95 and 20X NA 0.75 objectives at distances of 7, 14 and 21 μm from the wall surface. The average velocities during the half period of oscillation were measured by tracking the particle displacements. The minimum applied velocity was chosen to be similar to the flow measured in vivo by tissue ependymal ciliated cells of $\approx 200\,\mu$m/s [39]. The maximum applied flow velocity is 10 times the physiologically relevant one for ependymal cells. Figure 2.5g shows the output flow velocity varying the amplitude and frequency of the AC signal in the solenoid. The generated flow velocity was measured to be higher for low frequency due to the resonant response of the system.

2.4.3 Air Shear Stress setup

Shear stress in the airways comes from the movement of air during inhalation and exhalation. In order to investigate whether air shear stress could induce cilia alignment, we designed a setup where airflow can be applied on *in vitro* airway cells for many days. This system allows perfusion of humid air (relative humidity >90%) on cells grown in Transwell-chips using the desired flow rate.

The applied air is a mixture of normal air but with 5% CO_2 (BOC 225742-L) to keep the cell-medium at the right pH. The airflow rate going out from the cylinder can be set with airflow regulator (Cole-Parmer 5-mm Flowmeter, max 50 mL/min WZ-32015-01). The air is heated and saturated with water by pushing it through a leakage-free reservoir with warm sterile DEMI water. The reservoir was made by Dr Jurij Kotar using a 100 ml Duran bottle and with a modified lid that allows one inlet and one outlet for 4mm ID tubing. The process of saturation is helped by using a glass bubbler immersed in the water of the reservoir. The humid air is then additionally sterilised by passing through a 0.2 μm syringe filter and finally pushed into Transwell-chips (always placed in a 6-well plate, the lid has holes to allow connectors to go through) connected in series using Tygon tubing and 17 or 18 gauge dispensing needles (Intertronics FIS5601242 or FIS5601087), Figure 2.5c. The air going out from the Transwell-chips is then sent to a digital air flow rate sensor (Mouser 785-HAFBLF0200C4AX5 , Mfr. Honeywell with pin connectors JST PHR-6, Farnell) and a humidity sensor. Both the sensor outputs are continuously read to check for leakages and proper air humidity using an i2C protocol with a Raspberry PI connected to the internet. The reservoir, Transwell cultures and sensors are placed in a conventional incubator to keep the

right temperature and CO_2 percentage. The tubing (Tubing Tygon s3 e-3603 oi 4mm od 6mm), connectors and water reservoir were autoclaved prior assembly.

2.5 Conclusions

In this chapter, we presented a novel bio-compatible microfluidic device named Transwell-chip. This has been designed to apply shear stress on cells types that require a two-compartment (divided by a membrane) culture for optimal growth. For example, airway cells, that necessitate air-liquid interface for mucociliary differentiation. We found that airway cells differentiated very well in the device. Surprisingly, we found the chip also enables an efficient growth and differentiation of ependymal ciliated cells. In past works, the shear flow was applied to ependymal cultures grown in wellplates using rotating plates [125, 11] that did not allow homogeneous flow and caused contamination problems on many samples. For the first time, we have been successful in differentiating ependymal cells in a microfluidic device that permits the easy application of fluid shear stress and imaging, see Section 2.3 for cell culture protocols. Interestingly, we found the extra medium in the basolateral compartment of the 6-well insert to be a critical requirement for a good differentiation.

Transwell-chip offers many advantages over previous similar devices [145, 141, 146, 147, 137]. The use of PDMS permits to grow cells confined in any desired geometry and to image them at any time. The micro-fabrication process of the Transwell-chips requires only commercially available components and does not need expensive instrumentation. Moreover, the manufacturing process is very quick, so that multiple chips can be made in a single day, in contrast to previously reported devices [141]. We also designed and optimised setups that can be used with it for applying constant and alternate shear stresses using fluid or air.

Our device is only composed of a Corning Transwell insert and PDMS. Then, it is reasonable to guess that the cell types compatible with these two components can be grown successfully in this chip. This bio-compatibility permits to use the Transwell-insert for many other studies outside shear stress applications. For example, endothelial cells can be grown on the below compartment to reconstitute tissue-tissue interfaces critical to organ functions and provide low-cost alternatives to animal studies for drug screening [141]. In collaboration with Dr F. McCaughan we already started to use Transwell-chip for studying the volatiles released in the air by early-stage airway cancer cells, Appendix A. A group in Sheffield (Kai Erdmann' s Lab) has also started using our device for studying cancer cell lines of kidney in the presence of constant media perfusion. Overall, the advantages over the previously

published two-compartments devices offer great opportunities for the Transwell-chip to be used for shear and many other research studies in the future.

Chapter 3

Hydrodynamic entrainment of mammalian cilia in the brain

Motile cilia coordination is required for the proper function of major organs in humans; however, the mechanism behind it is still unclear. The traditional hypothesis is that cilia-driven flow could also itself be the mechanical origin of this coordination [67, 75, 66]. Cilia are microscopic filaments extended and moving into the fluid, and therefore the fluid will also act as a medium that will mechanically couple each single cilium. So, hydrodynamic interaction between cilia could provide the physical mechanism for their synchronisation and metachronicity, [77].

Despite many works supporting this view [68, 80, 81, 85, 69, 82, 83], recent experiments [65, 87, 88] showed evidences that elastic coupling through the cytoskeleton is more likely to be the main mechanism of flagellar synchronisation for the *Chlamydomonas* algae and other multi-flagellated algae. For example, the authors of [65] studied the phase locking between an external oscillatory flow and *Chlamydomonas* flagella. They measured that the required hydrodynamic forces for phase locking are over an order of magnitude larger than the ones between flagella, questioning the traditional view of hydrodynamic synchronisation and suggesting that flagellar synchronisation is due to elastic coupling, in agreement with [88]. Motile cilia in mammalian cells are also structurally connected through the cytoskeleton on the cell scale. This is achieved through the actin mesh that links all cilia of the same cell at the base [11, 10, 110] elastically, and even to the epithelium scale, through the basal membrane and cell junctions. In principle, these connections could lead to synchronisation [90, 89], leaving the origin of cilia coordination in mammal organs still unresolved.

This chapter is focused on understanding whether hydrodynamic forces are sufficient for the synchronisation of motile cilia in the brain. Specifically, we focused on ciliated ependymal cells of mouse brain which cilia have been already shown to be responsive to hydrodynamic forces and align with external flows. The function of motile cilia in the brain is still in debate (see Chapter 1). Investigating their mechanism of synchronisation can be crucial to explain how the observed complex spatiotemporally regulated pattern of cilia-driven flows arise in the brain. Inspired by the experimental setup in [65], we have tackled this problem by studying the response of single multiciliated cells to hydrodynamic oscillatory flows of the same order of magnitude of the cilia-driven flows.

In the next section are described the methods used to generate oscillatory flows over brain cultures and to measure cilia phase locking with external flows. Then I report the results obtained. Briefly, we find that phase locking of the motile cilia with the external flow (entrainment) is possible, and that it strongly depends on the number of cilia per cell. Specifically, cells with few cilia (up to five) are very responsive to external flows. Cilia from these cells are entrained with flow amplitudes comparable to the cilia-driven flows that regions of multiciliated epithelia can generate in vivo. By contrast, for cells with a higher number of cilia per cell, entrainment required much higher flow velocities. We suggest that this is due to the hydrodynamic interactions between cilia in the same cell and that multiple cilia can hydrodynamically screen the forces applied by the external flow, making the entrainment more difficult as the number of cilia increases. We support this view by quantitatively matching the data with a minimal hydrodynamic model using the idea that cluster of packed cilia can be represented by a hydrodynamically impenetrable rod. In the absence of external flow, we also measure an increase of the ciliary beating frequency (CBF) with the number of cilia, also consistent with hydrodynamically coupled cilia with coordinated motility [68, 164, 75]. From these data, we estimate the cilia-driven flow acting on each cilium in an isolated cell. In view of the high measured susceptibility to flow, we find this cilia-driven flow to be quantitatively sufficient for sustaining hydrodynamic synchronisation. Moreover, we match the trend of our experimental data with simulations of a minimal model of cilia interacting hydrodynamically (performed by Dr E. Hamilton), showing the possible hydrodynamic origin of the measured effects. Overall our results suggest that hydrodynamic forces are sufficient to be the mechanism behind the synchronisation of motile cilia in multiciliated cells of mammal brains.

3.1 Experimental setup and methods

We have used an *in vitro* culture assay of pure neural stem cells (NSC), isolated from neonatal mouse subventricular zone, that progressively differentiate into multiciliated ependymal cells [151]. Cells were grown in Transwell-chips as previously described in Section 2.2.1. After 15 days from the seeding in the chip, ependymal cells were fully differentiated into ciliated cells.

Firstly, each Transwell chip, in a 6 wellplate with glass bottom, is imaged in Brightfield using a Nikon 60X 1.20 NA water immersion objective on an inverted microscope, and kept at 37 °C and controlled pH using the custom made cell-chamber (Section 2.4.1). The inlet of the Transwell chip is connected to a custom-made fluid pump able to drive an oscillatory sinusoidal flow with defined frequency and velocity magnitude, see Figure 3.1a.

We applied external flows spanning in frequency f_{EX} from 10 Hz to 35 Hz, and a flow velocity v_{EX} (average during half cycle) from 200 μm/s to 2 mm/s. The lower value for v_{EX} was chosen to be close to the average net flow velocity created by ependymal cells in the brain [39]. The applied range of frequency is related to the average ciliary beating frequency of *in vitro* cultures. As a calibration step, the flow created by the pump was measured from the trajectory of microparticle tracers at 7 μm from the cell surface (see Section 2.4.2). In each experiment, a spatially isolated multiciliated cell was recorded for 5 seconds at 500 fps during each flow treatment to extract ciliary beating frequency (CBF) and phase. We took recordings only of cells close to the centre of the channel, beating in the same direction of the applied flow and with a well-defined peak in the frequency distribution (more information on the method in the next section 3.1).

3.1.1 Image acquisition and analysis

Images were taken with a Ti-E inverted microscope (Nikon, Tokyo, Japan) equipped with a 60X WI objective 1.20 NA. High speed videos were recorded at 500 fps using a CMOS camera (model No. GS3-U3-23S6M-C; Point Grey Research/FLIR). At each image was subtracted a running average of 60 frames. To define entrainment events, CBF is measured as the location of the highest peak of the first harmonic of the average periodogram, $P^S(f) = \sum_{px \in S} |\tilde{I_{px}}(f)|^2$, as in [165, 166, 72], with $\tilde{I_{px}}(f)$ the Fast Fourier transform (FFT) over time of the pixel intensity I_{px}, and S the ensemble of pixels in a sub-image thresholded for ciliary motion. The sub-image was defined to include all pixels for which the standard deviation of the intensity over time is larger than a threshold value (this found with Matlab

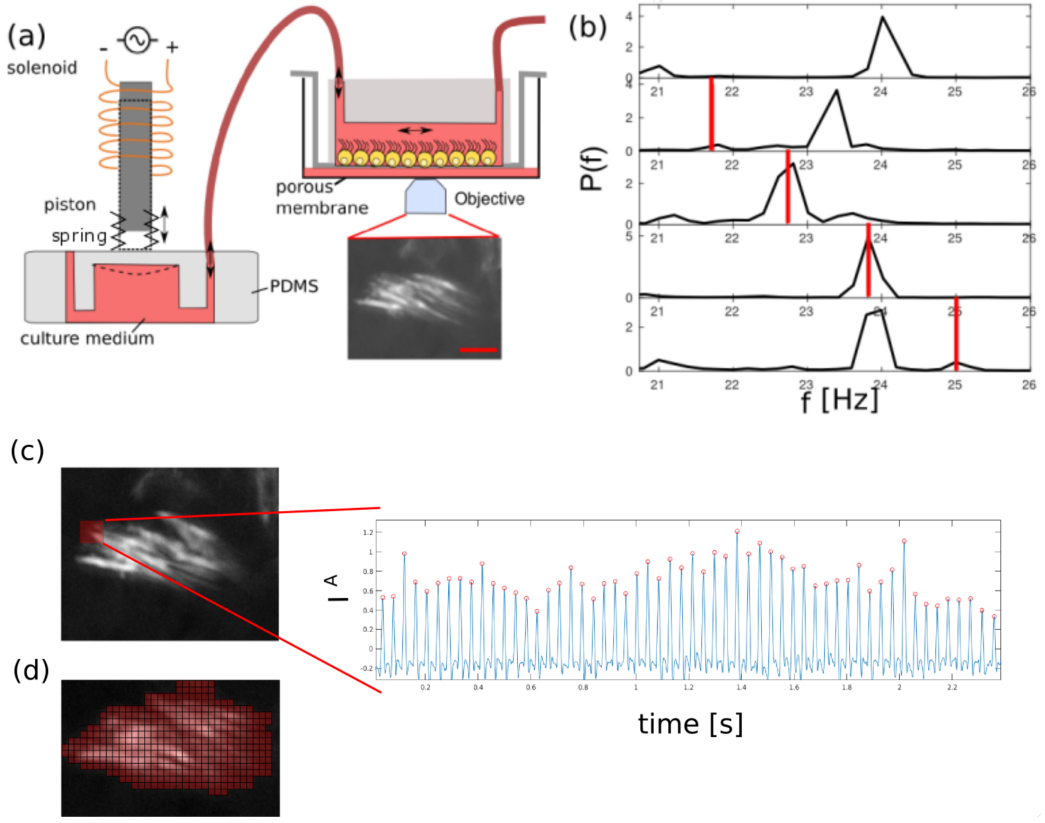

Fig. 3.1 **Methods.** (a) Schematic of the experimental setup, showing motility in a ciliated cell through a map of standard deviation in time, scale bar 5 μm. (b) The cilia beating frequency (CBF) is measured as the peak of the space-averaged periodogram of the cell pixels intensity, $P^S(f)$. An entrainment event is identified when the peak of the $P^S(f)$ coincides within 0.25 Hz with the frequency of the external flow f_{EX}, (red line). Here, the applied external velocity is $v_{\mathrm{EX}} = 0.6$ mm/s (average velocity during half cycle). (c) The pixel intensity $I^A(t)$ over time is used to identify the phase of a cilium or cilia within a cell. Each peak is the time when a cilium completes a beat cycle. The interrogation area is indicated in red on the standard deviation map. (d) The sub-image used for the calculation of the CBF and defined using the standard deviation of the pixel intensities over time.

function using Otsu's method), Figure 3.1d. Entrainment with the external flow is identified when the frequency of the signal highest peak pk^1 coincides with the frequency of the external flow within a certain tolerance σf. For our acquisition rate $\sigma f = 0.25$ Hz, the requirement is half of our frequency resolution. This method was implemented for high values of external flow $v_{\mathrm{EX}} > 1 mm/s$, when the external oscillatory flow induces a periodic defocusing of the field of view. This effect was detectable in the periodogram and often contributed to the highest peak of the signal, making it more tedious to measure CBF and entrainment events. For this reason, when the first peak of the signal $pk^1 \approx f_{\mathrm{EX}}$, we also

compared the second higher peak pk^2 to the value of pk_0^1, the signal peak in the absence of flow. When $pk^2 > 1/4pk_0^1$, we identify such entrainment events as false, and the second peak as the real contribution from the cell to the signal. This process was found to be valid and stable for every movie that we inspected.

Entrainment events can be identified by studying the phase of the cilia respect to the phase of the external flow. The cilium phase dynamics was calculated by tracking over time the pixel intensity of an interrogation area A, chosen to be close to the recovery stroke of the cell, $I^A = -\sum_{px \in A} I_{px}$. This area is small, such that only one or at most two cilia can be detected per time. When a cilium passes through this area, the pixel intensity I^A spikes, see Figure 3.1c. The time of the spike is an indication that the cilium completed a cycle, and the phase of the cilium ϕ_{cilium} increases by 2π. The number of cilia per cell was counted by inspection of movies at 500 fps, after median filtering (window of 3 x 3 pixels) and contrast correction - all the analysis were performed in Matlab.

In each culture, a small percentage of multiciliated cells has motile cilia lacking a common beating direction and frequency. For the entrainment experiments, we focused on 58 multiciliated cells from 8 different Transwell inserts, with all the cilia beating in a defined beating direction and showing a single peak spatial frequency distribution. We estimated the degree of cilia synchronisation for each cell (in the absence of external flows) using the frequency spatial noise $\eta_s = \sigma_f/(\mathrm{CBF})$, where σ_f is the standard deviation of the frequencies calculated on 4x4 pixels boxes over each cell, while the CBF is the median For the calculation of the spatial noise η_s and cell frequency maps we measured the frequency on 4x4 pixels boxes over the sub-image thresholded for ciliary motion. For each box, we averaged the FFT spectra of the pixel intensity over time, and we identified the frequency corresponding to the higher peak. In some rare cases, we noticed that second harmonics have a higher peak in the spectrum respect to the first one, leading to erroneous results. These rare events have a relevant effect when calculating the standard deviation of the frequency σ_f, since the standard deviation is very sensitive to outliers. Since these events rarely happen and in sparse positions over the cells, we decide to neglect all the suspected boxes with frequencies that are close to the double of the median frequency and do not have connected boxes with similar frequency (within the range of 2 Hz). We found this step critical for a correct calculation of η_s.

3.1.2 Cytochalasin-D treatment for actin depolymerisation

Cytochalasin-D treatment: following the protocols in [11], we depolymerised cell actin by adding 2uM Cytochalasin-D in the cell culture medium for 48hr. After imaging, cells (control and dug treated) were stained in 4% PFA for 10 minutes, permeabilised with Triton x-100 0.1% in PBS, and incubated for 1 hour with Nucblue R37605 (1 drop for mL of PBS) and with phalloidin for actin (Sir-Actin, 0.2 uM) following proprietary protocols. Z-stack were taken with a confocal microscope (slices of a distance of 0.15um each) and can be found at the following links: DMSO treated cells (control): Video 3, and Cytochalasin-D treated: Video 4. Both videos are available at https://doi.org/10.5281/zenodo.3689780.

3.2 Entrainment of multiciliated cells with external flow

We will refer to entrainment when we measure phase locking between the external flow and cilia within a cell. In contrast, the term synchronisation will be used to indicate when many individual cilia coordinate their beating to a coherent collective beat pattern. The entrainment regimes for a multiciliated cell in the frequency and flow domains are shown in Figure 3.2c. Each marker represents a separate recording, the solid markers identify an entrainment event, i.e. when the measured CBF coincided with f_{EX}, the frequency of the external flow, (more information in Section 3.1). The regimes saw here agree with the shape of an Arnold tongue, a general property of coupled phase oscillators, and as was previously found for a pair of eukaryotic flagella of the *Chlamydomonas* algae under the effect of external flow [65] and in model oscillator systems [167]. From these data, one can define the entrainment strength $\varepsilon(v_{\mathrm{EX}})$ as the range of frequencies where we measured entrainment. For values of v_{EX} and f_{EX} within the entrainment area, the phase difference between the cilium and the phase external flow, $\Delta(t) = (\phi_{cilium}(t) - \phi_{\mathrm{EX}}(t))/2\pi$, is constant over time ('locked') except for few occasional phase slips, Figure 3.2a-b. During a phase slip, the cilia carry out one beat more (or less) with respect to the external force, and $\Delta(t)$ increases (or decreases) of one unit. By contrast, when f_{EX} and v_{EX} are outside of the entrainment area, $\Delta(t)$ increases dramatically with time (Figure 3.2a-b). This behaviour of $\Delta(t)$ resembles the general phase dynamics of a self-sustained oscillator under external forces and noise [60]. Examples of the recordings that we used for the analysis are Video1 and Video2, available at https://doi.org/10.5281/zenodo.3689780 .

For each experiment, the CBF was measured using a spatial average over an area segmented over the multiciliated cell of the time-domain Fourier Transform (FFT) spectra of pixel intensity, similarly to previous works [166, 165]. The dynamics of the phase difference

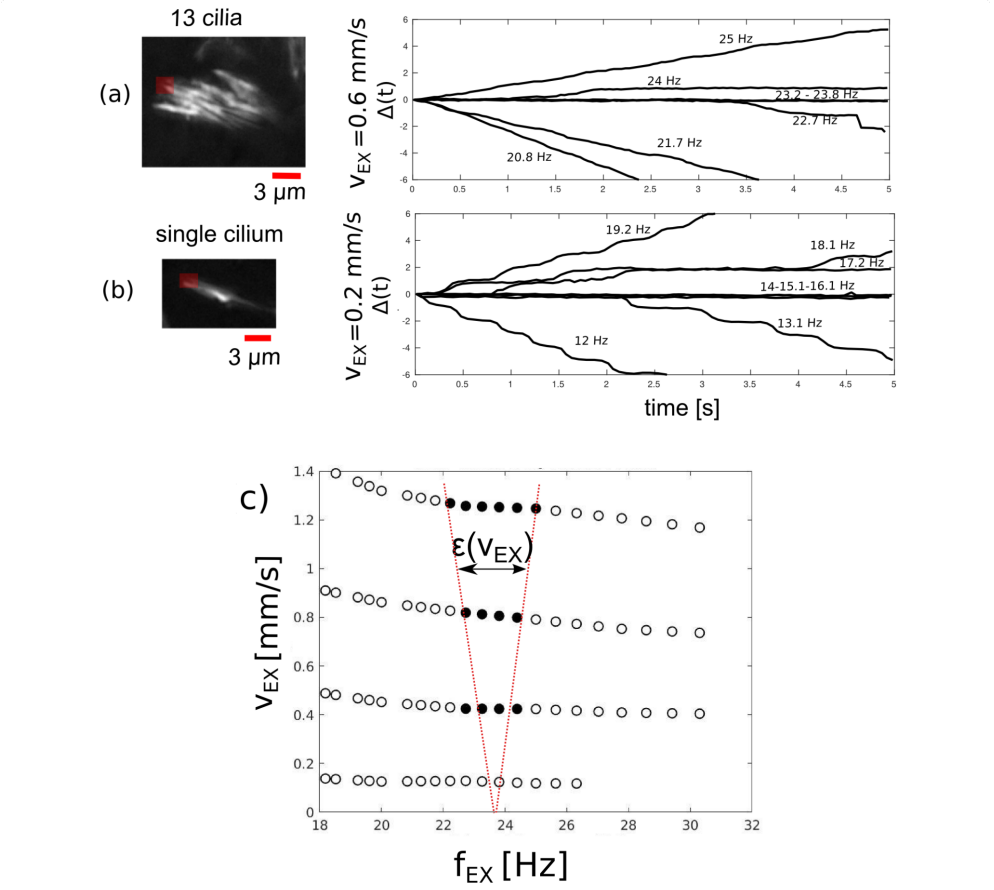

Fig. 3.2 **From cilia motility, we extract the frequency and phase of each cilium and the number of cilia per cell.** (a) Dynamics of the phase difference $\Delta(t)$ for a cilium within a group of 13 cilia during the application of an oscillatory external flow $v_{\mathrm{EX}} = 0.6mm/s$. The data are for the cilium passing through the interrogation window (red area) (b) Data for a single isolated cilium when an external flow of $v_{\mathrm{EX}} = 0.2mm/s$ is applied. The phase is constant (locked) when the cilium is entrained by the external flow. For the phase of the external flow we used $\phi_{EX}(t) = 2\pi f_{EX} t + \phi_0$, where ϕ_0 is set such $\Delta(t = 0) = 0$. The interrogation windows used are marked in red over the standard deviation maps of the intensity of the pixels. (c) Entrainment region, for the same multicilated cell, in the frequency and flow velocity domains; each marker here is the result of a separate recording. Markers are dark when the average CBF of the cell matches the frequency of the external flow. The entrainment strength, $\varepsilon(v_{\mathrm{EX}})$, is the range of frequencies spanned horizontally by the black dots. The entrainment region is highlighted here as the area between the red dashed lines; lines are a guide to the eye.

$\Delta(t)$ can be found by tracking the passage of one cilium of the multiciliated cell in an interrogation window close to the position of the recovery strokes as was done on algae [85]. Additional information on both image analysis methods is reported in Section 3.1.

3.3 Entrainment depends on the number of cilia

Ciliated cells in culture (probably in contrast to most ciliated epithelia *in vivo*) are not always fully ciliated, and they exhibit a varying number of cilia per cell. (see Figure 3.3a-b). For each multiciliated cell, we measured the entrainment strength ε as a function of v_{EX}, the average magnitude speed of the oscillatory flow. We found that ε increases almost linearly with v_{EX}, consistent with a recent study on the eukaryotic flagella of *Chalmydomonas* algae [65], Figure 3.3d. Moreover, ε does not change significantly with the intrinsic (absence of external flow) CBF of the cells (Figure 3.3c), but dramatically decreases with the number of cilia per cell, see Figure 3.3d. Markedly, cells with 1 to 5 cilia were entrained by the external flow over a frequency range of around 2 Hz with flow velocity $v_{\mathrm{EX}} \approx 200\,\mu$m/s. In sharp contrast, cells with higher numbers of cilia were entrained over a detectable frequency interval only for strong flows $v_{\mathrm{EX}} > 600\,\mu$m/s. The linearity of ε with the external flow v_{EX} and its trend with the number of cilia are highlighted in Figure 3.4d by showing the entrainment strength divided by applied the external velocity ($\varepsilon(N)/v_{\mathrm{EX}}$) as a function of N, the number of cilia per cell.

The observation that high forces are required to entrain larger clusters of cilia is not in contrast with hydrodynamics because the external forces on each cilium could be hydrodynamically screened by the forces applied by the beating cilia nearby. This effect can be estimated: for an isolated cilium, the total drag force F_{EX} exerted by the external flow is proportional to the drag coefficient. If we assume each cilium as a rigid rod, its drag coefficient in the fluid bulk is $\gamma = 4\pi\eta L/[\log(L/r) - 1/2]$ [168], with $r \ll L$ being respectively the radius and the length of the cilium and η the viscosity of the medium. In this case, the external drag force is $F_{\mathrm{EX}} = \gamma v_{\mathrm{EX}}$. For an ependymal cell with multiple cilia, the bases of the cilia are very densely and homogeneously concentrated in the centriolar patch located at the rear of the cell, [11], as we also see in our culture, Figure 3.4a-b. Therefore, from the hydrodynamic point of view, a cluster of cilia all beating at the same frequency and phase can be modelled as a single impenetrable rod sticking out from a cell membrane. The effective rod has a length L and an effective radius $r_e(N) > r$ that contains all the N cilia from the same cell, [169]. For notation purposes, we name this approximation 'Impenetrable Effective Rod' model (IER). This assumption is investigated numerically in the Appendix B.3. Then we can use the drag coefficient of this effective rod to estimate the hydrodynamic screening due to the nearby cilia to external flows. $F^i_{\mathrm{EX}}(N)$, the effective drag experienced by each cilium (i) in the cluster of N is thus:

$$F^i_{\mathrm{EX}}(N) = \frac{\gamma_e(N) v_{\mathrm{EX}}}{N}, \quad \gamma_e(N) = \frac{4\pi\eta L}{\log(L/r_e(N)) - 1/2}. \tag{3.1}$$

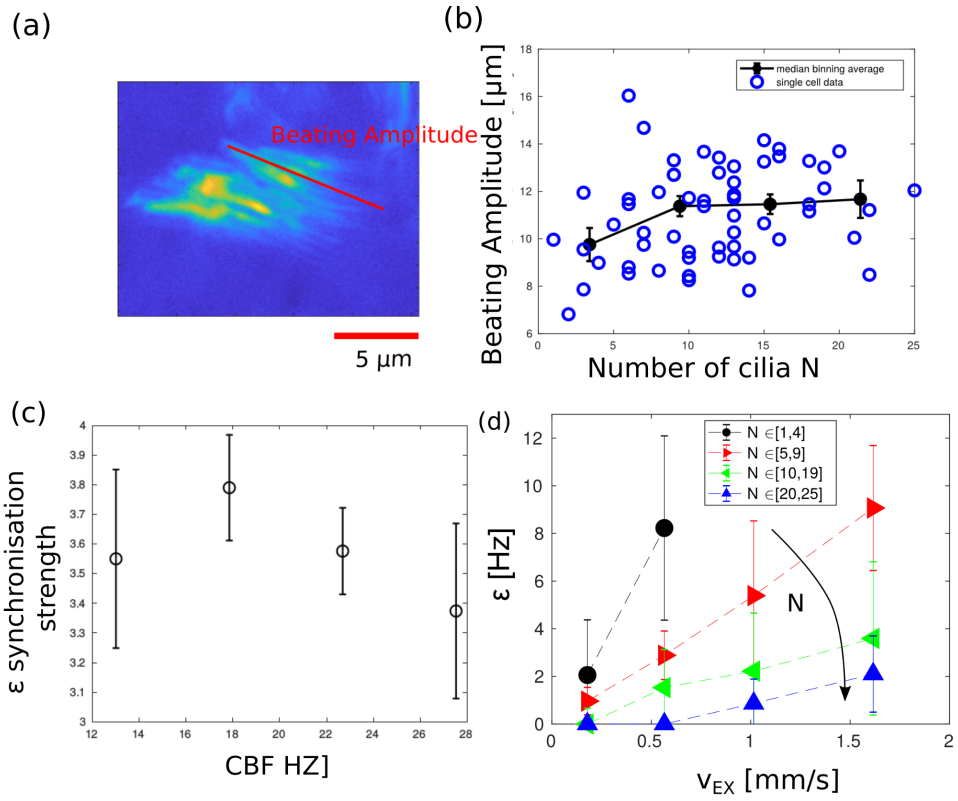

Fig. 3.3 **The entrainment strength depends on the number of cilia per cell.** We measured the maximal ciliary beating amplitude for cells with a different number of cilia. (a) The maximal beating amplitude for a cilium within each cell was measured by inspecting the recordings from the top view and marking two extreme points at the power and recovery stroke. For example, see Video 5 , https://doi.org/10.5281/zenodo.3689780. The length of the red line is the measured amplitude; below there is the standard deviation map of the same cell. (b) The graph shows the beating amplitudes for the 58 cells analysed as a function of the number of cilia per cell and the binning average. Cells with fewer cilia have around $1.5\,\mu$m smaller maximal ciliary beating amplitude. (c) The synchronisation strength ε of cilia within a cell does not significantly depend on the intrinsic CBF (in the absence of flow). The graph shows the entrainment strength ε against CBF when an external oscillatory flow of $v_{\mathrm{EX}} \approx 1\,$mm/s is applied. The data are presented median binned with standard deviations of the mean as error bars. (d) The entrainment strength $\varepsilon(v_{\mathrm{EX}})$ increases proportionally to the applied external flow but decreases with the number of cilia per cell N. Each line is the average of this trend over a group of cells with a similar number of cilia. Error bars represent the standard deviation. Complete datasets are shown in Figure 3.7.

We take the area of the centriolar patch $S_c(N)$ to quantify the effective radius of the rod as a function of the number of cilia within a cell: $r_e(N) = (S_c(N)/\pi)^{-1/2}$. We used transgenic mouse cells Cen2-GFP [170]. This choice allows visualisation of the base of the cilium

(centrosome) in the living cells [11]. We measured the area of the centriolar patch $S_c(N)$ for some of the cells treated with the oscillatory flow, Figure 3.4b. We found this number to increase linearly with the number of cilia, so that $r_e(N) \approx CN^{1/2}$, with $C = 0.6 \pm 0.1\mu$m, Figure 3.4c. In this scenario, the density of cilia in the effective rod is always constant $\rho_c = N/\pi r_e^2 = 1/(C^2\pi) \approx 0.9$ cilia/μm^2. It is worth noting that for cells with $N > 25$ we then estimate an effective radius of $r_e > 3\mu$m $\approx L/4$. For such aspect ratios, the slender body assumption in Eq 3.1 is less accurate.

We can compare this situation with the one where cilia are so densely packed that they are in contact: the spacing between neighbour cilia would be $2r$, where r is the radius of the single cilium. Then the section area of the effective rod could be approximated by $\pi r_{lim}^2(N) \approx N(2r)^2$. Also in this case, the effective radius increases with the root of N, $r_{lim} \approx C_{lim}N^{1/2}$ with $C_{lim} = 2r/\sqrt{\pi} \approx 0.11\mu$m and cilia density is constant: $\rho_c^{lim} \approx 26$ cilia/μm^2. In both scenarios, we should be able to show that the term $O(1/N)$ is leading in Equation 3.1, and that the drag on each cilium decreases as the number of cilia nearby increases, $F_{\mathrm{EX}}^i(N+1) < F_{\mathrm{EX}}^i(N)$. As the force applied by the external flow decreases, we also expect to have a drop in the entrainment.

3.4 Hydrodynamic screening affects the entrainment of motile cilia

The expression in Equation 3.1 permits to quantify the force applied on each cilium by the external flow as the number of cilia per cell increases. We can check whether this approximation is in agreement with the measured data. How to relate the entrainment strength to the external forces may be dependent on the intricate molecular response of the individual motors within a cilium [171] and on the efficiency of the ciliary beat [106]. Here we use as a minimal cilia model a two-state oscillator in viscous liquid driven by linear potential and entrained by an external periodic force (geometric rower model) [167], see also Appendix B.1. The molecular motors acting on the cilium are coarse-grained with a constant driving force F_{dr} applied to a sphere or a cylinder representing the cilium [83]. The constant force F_{dr} switches in sign when a particular limit configuration is reached ('geometrical switch') so that the rower is pushed in the other way, see also Figure 3.6a. The limit configurations can be set at the edges of a path of length A, so that the rower undergoes long-time periodic motion with amplitude A and frequency $f = \mathrm{CBF}_0 = F_{dr}/(2A\gamma)$, where γ is the drag coefficient of the rower. On top of this force, we can add a constant external force F_{EX} to the rower, for example, given by an external flow. This force can be set to switch in

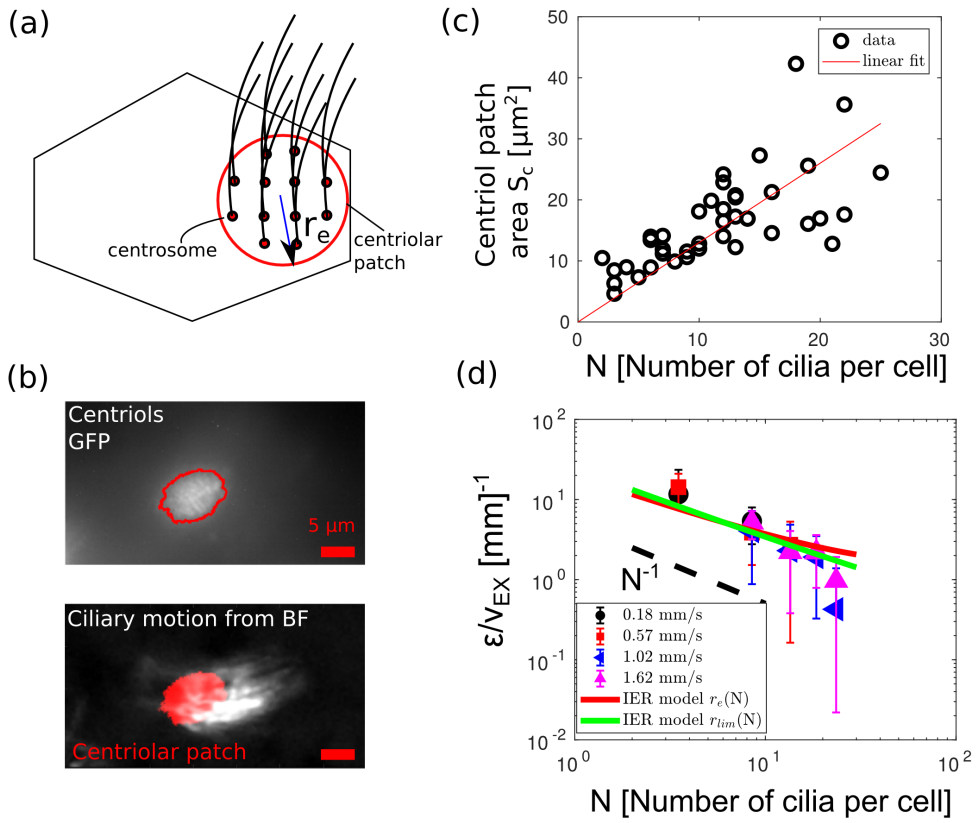

Fig. 3.4 **How a cell is affected by an external flow depends on the number of motile cilia: the entrainment of cilia motility gets weaker increasing the number of cilia, in agreement with a model where the nearby cilia hydrodynamically screen the external forces.** (a) Cilia in ependymal cells are very densely packed at the rear of the cell and are anchored at the cell membrane in the centriolar patch. The cluster of beating cilia can be hydrodynamically approximated as a unique impenetrable effective rod with the same size of the centriolar patch. (b) Cen-GFP mice can be used to measure the size of the centriolar patch for living cells before flow experiments. In the top figure, we show cilia centrioles in white (GFP). Stimulated emission depletion (STED) microscopy is necessary to resolve the single centriole [11]. Here we use these images only to measure the total area of the centriolar patch. The area is obtained by using Otsu's threshold method (red borders). In the bottom figure, we superimpose the measured centriolar patch with the cell motility map extracted from BF images. (c) The area of the centriolar patch S_c increases roughly linearly with the number of cilia,(linear fit R-squared $= 0.4$). We used this data to find an analytic expression for the r_e as a function of the number of cilia that can be plug in the Impenetrable effective rod (IER) model. (d) The measured entrainment strength decreases with the cilia number and collapses onto a single set when divided by the applied the external velocity ($\varepsilon(N)/v_{\mathrm{EX}}$). Here we show the median binned data with standard deviations. The trend with the number of cilia is in agreement with the proposed model, using a single fit parameter F_{dr}, that is the driving force coarse-graining the molecular motors within the cilium. We show the fit results using as effective radius (i) $r_e(N)$, equal to the centriolar patch size (R-squared $= 0.67$); (ii) $r_{lim}(N)$ that is the limit case where cilia are touching (R-squared $= 0.69$). The length of the effective rod is $L = 11\mu$m and medium viscosity $\eta = 10^{-3}$ Pa s for both fits.

sign accordingly to the defined external frequency f_{EX} and mimic the external oscillatory flow in our system. For this geometrical rower model, an analytic solution for the entrainment strength of the rower with the external oscillatory force can be found [172] which has a linear relationship with the ratio of the driving and external force. See also Appendix B.1 for more details. The entrainment strength is:

$$\varepsilon(N) = \frac{2(\mathrm{CBF}_0)F^i_{\mathrm{EX}}}{F_{dr}}, \tag{3.2}$$

We next apply this model to our data: the CBF_0 is the beating frequency of the cilium in the absence of external forces. In our culture, the CBF of the isolated cilium was measured to be $\mathrm{CBF}_0 \simeq 15\,\mathrm{Hz}$, see Figure 3.5a. The force applied by the external flow on the cilium is given by Equation 3.1, $F^i_{\mathrm{EX}} = \gamma_e(N)v_{\mathrm{EX}}/N$, with v_{EX} the average magnitude speed of the oscillatory fluid flow. On the other hand, we assume the driving force F_{dr} as an intrinsic parameter of the cilium, therefore independent of N and v_{EX}. The driving force can be calibrated from the motion of the single cilium in the absence of any external flow. The latter has to balance the hydrodynamic drag F^h_{dr} experienced by the cilium while moving with frequency CBF_0 and amplitude A. We again assume the cilium has the drag coefficient of a rigid cylinder and beat with amplitude $A \approx L \approx 11\mu\mathrm{m}$. Then, the driving force is equal to the hydrodynamic drag $F^h_{dr} = \gamma 2A(\mathrm{CBF}_0) \approx 11\,\mathrm{pN}$. However, in the real situation, the driving force has to balance the fluid viscous drag but also the intracilary friction given by viscoelastic structural elements in the cilium, such as Nexin linkers [106, 173, 174]. Inspired by the work of [106], we consider internal friction forces that can be assumed to be proportional to the hydrodynamic drag experienced by the cilium while beating. The total driving force can then be written as $F_{dr} = F^h_{dr}/\eta_c$, where $\eta_c < 1$ is the chemical-mechanical efficiency of the ciliary beat. More details can be found at Appendix B.1.1. Finally, for the cilium i in a bundle of other N cilia arranged in a hydrodynamically impenetrable cylindrical rod of radius $r_e(N)$ and length L, we have:

$$\frac{\varepsilon(N)}{v_{\mathrm{EX}}} = \frac{2\ \mathrm{CBF}_0}{(F^h_{dr}/\eta_c)} \frac{4\pi\eta L}{N[\log(L/r_e(N)) - 1/2]}. \tag{3.3}$$

We can fit this model to our data using the effective radius r_e found previously from experimental data, and the beating efficiency η_c as a unique parameter. Results are in Figure 3.4d. From the fit we found the driving force $F_{dr} = F^h_{dr}/\eta_c = 60 \pm 3\,\mathrm{pN}$, with R-squared= 0.67. From this we can estimate the ciliary beating efficiency $\eta = F^h_{dr}/F_{dr} = 0.18 \pm 0.01$. This value is in remarkable agreement with the ones estimated by previous works, where they found $\eta_c \in [0.2, 0.4]$ [174, 106]. It is worth noting that the experimental values are signif-

icantly lower than the fit line (within the error bars) for cells with a large number of cilia ($N > 20$). This difference could be due to the fact that our slender body assumption of Equation 3.1 is not very accurate in this regime, where $r_e \approx L/4$.

The same fit was performed using the effective radius r_{lim} in the situation of cilia touching, Figure 3.4d. For this limit case we found $F_{dr} = 30 \pm 3$ pN, with R-squared $= 0.69$. With this number we can estimate a ciliary beating efficiency of $\eta_c = 0.36$, that is still in agreement with the past literature [174, 106]. While cilia basal bodies distances are confined by the cytoskeleton in the cell, we can not exclude that while cilia are entrained to move at the same frequency, they also tend to be closer. For example, simulations have confirmed that hydrodynamic interactions can lead to bundle formation of *E. coli* flagella, and that the fluid flow generated by the flagella draws them together and enhances the bundling process [175]. Moreover, in colloids driven by optical tweezers in a circular path, doublet clusters spontaneously arise by the hydrodynamic interactions between the particles [176]. Despite its simplicity, the hydrodynamic model with two different estimates of the effective radius explains the measured trend quantitatively. Moreover, it leads to a value for the mammalian ciliary beating efficiency that is in agreement with the ones of other ciliated organisms.

3.4.1 CBF increases with the number of cilia per cell

Previous theoretical works [75, 68] predicted that arrays of beating cilia speed up their frequency (with respect to their intrinsic beating frequency) when hydrodynamically synchronised. The frequency increase is maximum when all cilia are beating in phase. Also in our model, the fact that cilia from the same cell behave as a unique rigid rod beating at the same frequency would imply that the average CBF (in the absence of external flow) should increase with the number of cilia per cell.

We again assume the molecular motors acting on the cilium to be coarse-grained into a constant driving force F_{dr} switching in sign at defined limit configurations [83]. In the absence of interacting cilia, this driving force is equal to the sum of the hydrodynamic drag and the internal ciliary friction [106]. The force balance equation can be written as $F_{dr} = 2A\gamma[\mathrm{CBF}_0] + 2A\gamma[(1-\eta_c)/\eta_c][\mathrm{CBF}_0]$, where $\gamma[(1-\eta_c)/\eta_c]$ is the inter-cilium friction coefficient and η_c is the chemo-mechanical ciliary beating efficiency defined in the previous paragraph, γ the cilium drag coefficient. In a multiciliated cell with N cilia, our Impenetrable Effective Rod (IER) assumption states that each cilium $i \leq N$ has drag coefficient γ_e/N, reduced by the hydrodynamic screening of nearby cilia, Equation 3.1. Now the driving force on this cilium F^i_{dr} can be written as $F^i_{dr} = 2A(\gamma_e(N)/N)[\mathrm{CBF}] + 2A\gamma[(1-\eta_c)/\eta_c][\mathrm{CBF}]$. We

assume the driving force is an intrinsic property of the cilium and independent on the cilia number, $F_{dr} = F^i_{dr}$. Thus we find:

$$\mathrm{CBF}(N) = \frac{\mathrm{CBF}_0}{1 - \eta_c + \eta_c[\gamma_e(N)/(\gamma N)]} \,. \tag{3.4}$$

The above equation describes a saturating curve for $\mathrm{CBF}(N)$ as a function of the number of cilia within a cell. The ciliary beating efficiency sets the maximum value for the ciliary beating frequency at large N: $\mathrm{CBF}_{\max} = \mathrm{CBF}_0/(1-\eta_c)$. We compare this theoretical trend with the CBF gathered from 120 cells. In Figure 3.5a we show the theoretical curves using η_c and $\gamma_e(N)$ obtained from the previous experiments with external flows considering the two scenarios of cilia touching (green line r_e^{lim}) and cilia separated by the same distance of the basal bodies (red line r_e).

For the former case, the value for $\mathrm{CBF}_{\max}$ seems to agree with the measured one, although the theoretical CBF increase at small N is sharper than the one we observed. Regarding the latter case, the theoretical CBF increase seems to be always lower than the average measured trend, although theoretical values are still within the errorbars. From the fit of the data with the equation 3.4 (two free parameters) we obtain $\eta_c^{CBF} = 0.4 \pm 0.2$, that is still in agreement with previous works [174, 106], and $C^{CBF} = 0.7 \pm 0.4 \mu$m, where the effective radius of the cilia bundle is $r_e^{CBF} = C^{CBF}\sqrt{N}$, again in agreement with our previous measurement of cilia distance within a cell. The differences between the values obtained from this fit and the values from the previous experiments could be because cilia are not always beating coherently in the absence of external flows. We estimated the degree of cilia synchronisation for each cell (in the absence of external flows) using the frequency spatial noise $\eta_s = \sigma_f/(\mathrm{CBF})$, where σ_f is the standard deviation of the frequencies calculated on 4x4 pixels boxes over each cell, while the CBF is the median, see for example the frequency map in Figure 3.5b.

We found the spatial noise to be significantly different from zero for all the cells examined, highlighting that cilia in the same cell do not beat as a unique entity, as assumed by our IER model, but with a finite frequency de-tuning. By contrast, when cilia are entrained with the external flow, the spatial noise significantly decreases, Figure 3.5b. This effect is expected to reduce the hydrodynamic screening between cilia respect to the one expected from the IER model, and in turn to lead to a less sharp growth of the CBF with the number of cilia.
From our measurements, CBF seems to reach a plateau value for cells with $N > 20$ that is roughly 50% higher compared to the ones with only a few cilia. A similar CBF increase with cilia number was measured after cells were treated with actin drug Cytochalasin-D, which progressively depolymerises the actin network connecting the centrioles in the cells and at

the cell border [110, 11], Figure 3.5c. This evidence suggests that the observed CBF increase with cilia number is not due to cytoskeleton coupling.

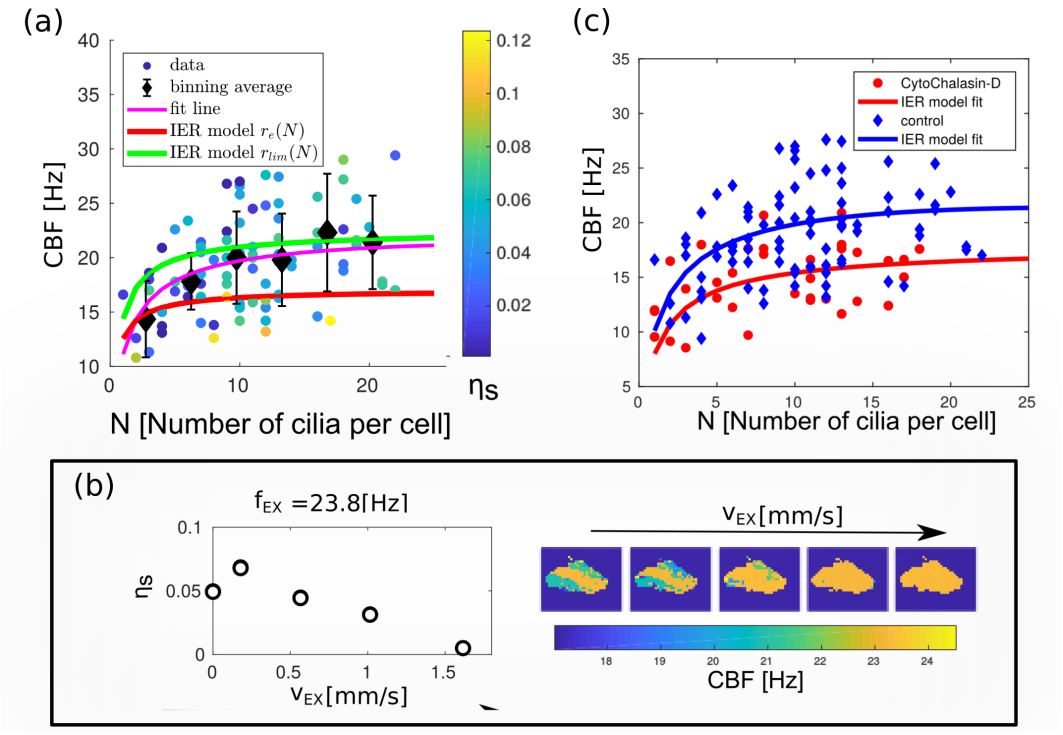

Fig. 3.5 **In the absence of external flow, the ciliary beating frequency (CBF) increases with the number of cilia.** (a) Individually (and binned) CBF for 120 cells as a function of the number of cilia. Error bars are the standard deviation of the binned data. The colour of the unbinned data indicates the value of spatial noise η_s for each cell. A high value indicates that cilia within a cell are beating at a different frequency and so very far from the assumptions made for the Impenetrable effective rod (IER) model. Interestingly, the average value of η_s for cells with cilia $N < 20$ is $\langle \xi_s \rangle_{N<20} = 0.04 \pm 0.02$, while it is almost double for the cells with a larger number of cilia $\langle \xi_s \rangle_{N>20} = 0.07 \pm 0.02$. The red and the green line would show the predicted trends of the CBF if cilia were behaving as single impenetrable rods (IER model). For these two lines, we used the values found in the previous experiments with external oscillatory flows. Respectively the red line assumes cilia average distance dictated by the basal bodies distance and the green line is the limit case of cilia touching. The purple line is a fit with two free parameters (η_c and C^{CBF}). (b) The spatial noise of a ciliated cell decreases when cilia are entrained to external flows. For example, we show this decrease for a single cell; each marker of spatial noise was calculated using a frequency map, illustrated in the left panels, with the colour corresponding to the measured frequency in each 4x4 pixel box. (c) CBF increases with the number of cilia for both control and cells treated with actin drug Cytochalasin-D. Blue markers (control) are the same data as in Figure (a). Red markers are from cells treated with the actin drug. We fit the data with the IER model. For cells treated with Cytochalasin-D we found $\eta_c^{Cyto} = 0.5 \pm 0.1$, $C^{Cyto} = 0.2 \pm 0.3 \mu$m, and $\mathrm{CBF}_0^{Cyto} = 10 \pm 2$ Hz, respectively for the energy beating efficiency of the cilium, the interciliary distance ($r_e^{Cyto}(N) = C^{Cyto}\sqrt{N}$) and the ciliary beating frequency of the isolated cilium, R-squared= 0.13. These values are still in agreement with the one found for cells not treated with actin drug, where $\eta_c^{CBF} = 0.4 \pm 0.2$ and $C^{CBF} = 0.7 \pm 0.4 \mu$m, R-squared= 0.18. See Section 3.1.2 for the Cytochalasin treatment protocol.

3.5 Estimation of the flow generated by cilia within a cell

Hydrodynamic screening effects and interciliary dissipation seems to quantitatively describe the observed trend of CBF and entrainment strength with the number of cilia. We now assume that the observed trend of the CBF with the number of cilia is only due to hydrodynamic forces between cilia. This assumption is also motivated by the fact that CBF increase was not affected after depolymerisation of the cell actin network, supporting the hypothesis that the measured effect is not driven by the elastic forces transmitted through the cytoskeleton. Moreover, we argue that steric interactions between cilia can not be responsible for an increase in the average ciliary beating frequency, see Appendix B.2. In this limit scenario we can use the same minimal model to roughly estimate the magnitude of the flow on the cilium i created by nearby cilia $j \neq i \in N$ in the absence of i. It is now convenient to write an explicit expression for the average hydrodynamic forces applied by nearby cilia during half cycle of the beating. The sum of these forces we now define as F^i_{nc}, acting on the cilium i in a cell of N cilia. We can write a force balance equation on the cilium i averaged during its half beating. Keeping the former assumption of the single cilium as a rigid rod driven by a constant switching force F^i_{dr}, the average velocity v^i of the cilium during half cycle can be found from:

$$\gamma v^i + \gamma v^i \frac{1-\eta_c}{\eta_c} = F^i_{dr} + \gamma v^{nc}_{\mathrm{EX}} \tag{3.5}$$

where we introduced $v^{nc}_{\mathrm{EX}} = \sum_{j\neq i}^{N} v^{ij}$ as the sum of the average flow velocity v^{ij} produced by the cilium j at the position of the cilium i during its half beating cycle. This is the average speed of the flow induced by all the other cilia at the position of the cilium i during its half beating cycle, if the cilium i were to be removed. As in the previous section η_c accounts for the internal ciliary dissipation [174, 106]. The driving force is again $F^i_{dr} = \gamma v^i_0/\eta_c \approx 2A(\mathrm{CBF}_0)\gamma/\eta_c$, and v^i_0 is the cilium average velocity in the absence of any interaction. From Equation 3.5 we estimate that the flow induced by the nearby cilia on the cilium i is

$$v^{nc}_{\mathrm{EX}} = (v^i - v^i_0)/\eta_c. \tag{3.6}$$

We previously showed that the average velocity of each cilium, v^i, reaches a plateau value v^i_{max} when the number of cilia is sufficiently large. This is valid for hydrodynamically screened cilia within the assumptions made for the Impenetrable Effective Rod model. The value of the maximum velocity can be found from $v^i_{max}/v^i_0 = \mathrm{CBF}_{\max}/\mathrm{CBF}_0 = 1/(1-\eta_c)$, Equation 3.4. Thus $v^i_{max} = v^i_0/(1-\eta_c)$.

Substituting the latter expression into Equation 3.6, we found in the limit of large number of cilia

$$v_{\mathrm{EX}}^{nc} = v_0^i[\frac{1}{(1-\eta_c)} - 1]/\eta_c = \frac{v_0^i}{(1-\eta_c)}. \tag{3.7}$$

Therefore, it becomes apparent that for cilia bundles beating at the maximal frequency $\mathrm{CBF}_{\mathrm{max}}$, the flow generated by all other cilia (nearly) sets of the flow generated by a central cilium, $v_{\mathrm{EX}}^{nc} = v_{max}^i$. This simple estimate provides a useful measure of the flow generated by the nearby cilia directly on the cilium i during hydrodynamical screening. We previously found that a similar magnitude of external oscillatory flow ($v_{\mathrm{EX}} \approx 200\,\mu$m/s) was sufficient to entrain small groups of cilia, and so certainly a single cilium (Figure 3.3d). We thus expect that the extracted oscillatory cilia-driven flow v_{EX}^{nc} is also sufficient to ensure hydrodynamic entrainment of the cilium i. The same reasoning could be extended for each other cilium j in the cell, suggesting that cilia within a cell could be synchronised through internal hydrodynamic forces. Moreover, the magnitude of the interaction velocity v_{EX}^{nc} is in agreement with the measured flow field near eukaryotic beating cilia with similar length [94, 85], and by the net flow generated by ependymal cells *in vivo* [39], supporting that the initial assumption that the measured forces between cilia can have a hydrodynamic origin.

Simulations of hydrodynamically coupled oscillators under external flow

To identify if the dynamics of cilia could stem from hydrodynamic coupling, we compared our data with simulations of simplified cilia coupled hydrodynamically. Simulations were run by Dr E. Hamilton. Building on previous work by our group and others [83] we know that minimal 'rower' models in which each cilium is represented by a single sphere driven by a geometrically updated potential can shed light on the effects of synchronisation due to cilia arrangement and beating dynamics. This type of model is based on the physical intuition that, in a coarse-grained fashion, the degrees of freedom of the complex cilium shapes and activity can be captured by a rower's driving potential. The main advantage of this approach is that it greatly simplifies the calculation of drag forces, both those acting on the individual object and the force induced by one object on another [95, 96]. The bead moves away from the trap vertex until it reaches the switch point, where the trap is reflected, and the bead reverses direction, Figure 3.6a. This feedback-controlled motion of the potential is sufficient to induce sustained oscillations, and each particle undergoes long-time periodic motion with a fixed amplitude but free phase and period. Theoretical and experimental studies showed that pairs and chains of rowers could undergo synchronization [82] and even metachronicity [98, 99]

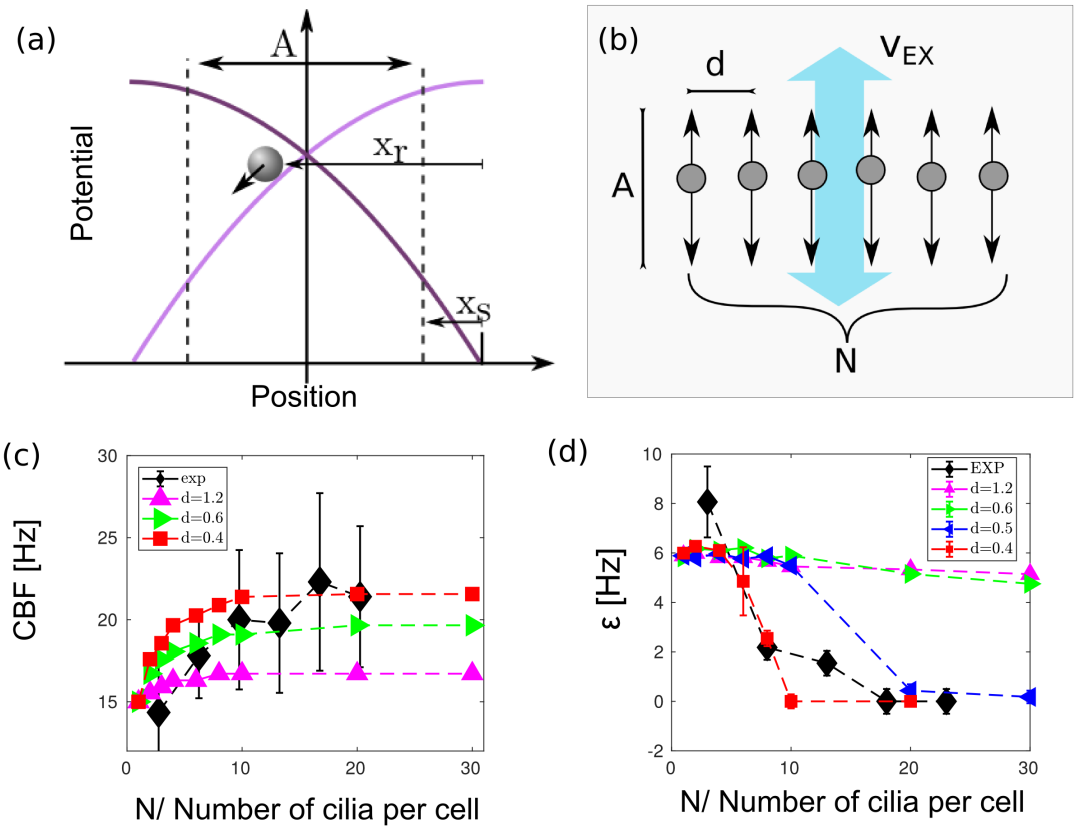

Fig. 3.6 **A coarse-grained cilia model where each cilium is a hydrodynamically coupled phase oscillator is studied numerically, and recapitulates the main trends seen in the experiment.** (a) Geometric switch "rower" oscillator: Two potentials (purple and light purple curves) are switched on and off in turn using feedback loops. The other potential is switched when the particle reaches the position indicated by the black dashed line, maintaining a phase-free oscillation. (b) Illustration of the simulation rower geometry. (c) The median frequency of rowers increases with the number of rowers N. The growth is more marked as the rowers get closer, $d = [0.4, 0.6, 1.2]\,\mu$m. The trend in simulations of the simple rower model matches with the experimental data (black points are the binning median of the CBF measured experimentally with standard deviation errors), where the distance between cilia could be smaller (up to $d_{cilia} \approx 0.2\,\mu$m). (d) Chain of rowers under external oscillatory flow. The entrainment strength ε measured with the external flow decreases as the number of rowers, or their density, increase. For the rowers with distance $d = 0.4\,\mu$m entrainment was not observed when the number of rowers was $N > 10$. In black are plotted the experimental data showing a similar trend. However, the magnitude of the external flow used experimentally was an order of magnitude higher than the one used in simulations, and the distance between cilia is lower. The magnitude of the external oscillatory flow in the simulation is $v_{ex}^{sim} = 30\,\mu$m/s, while the experimental data were obtained from cells treated with $v_{\mathrm{EX}} = 600\,\mu$m/s (unbinned experimental data in Figure 3.7).

when the separation is sufficiently small.

Each cilium is simulated with a rower with radius $a = 0.1\,\mu$m, oscillating with fixed amplitude $A = 7\,\mu$m, tuning the strength of the parabolic trap to ensure an intrinsic frequency $f_0 = 15\,$Hz. These values were chosen to be similar to the ones that found experimentally tracking a single cilium. Simulations of chains were performed by Dr Hamilton using a code developed for [95] varying the number of N rowers, keeping nearest neighbours separated on average by a distance d. We explored the set of $N = [1,2,4,6,8,10,20,30]$ and $d = [0.4,0.5,0.6,1.2]\,\mu$m (see Figure 3.6c). The rowers are coupled through the hydrodynamic forces via a Blake tensor, with the oscillations occurring at a fixed distance $z_{wall} = 7\,\mu$m above the no-slip boundary [95]. For sufficiently small d, the chain of rowers synchronises through hydrodynamic forces and beads oscillate at a common frequency $f > f_0$, as seen in Figure 3.6c. As expected, the frequency-shift $\delta f = f - f_0$ initially increases with N, before saturating. The increase is more significant for rowers with small separation, due to the increase in their interaction strength. Interestingly, despite the simplicity of the rower model, the order of magnitude of δf in these simulations is the same as observed experimentally, although the latter is consistently lower. This could be explained by the fact that the distance between cilia in the same cell is much smaller ($d \approx 0.1\,\mu$m) than the one that we can simulate (for distances $d \approx a$ near-field effects may play a role that we do not take into account).

Dr Hamilton then simulated the chain of rowers under an external flow with a magnitude of $v_{\mathrm{EX}}^{sim} = 30\,\mu$m/s. The chain was defined as entrained when more than 80% of the rowers were phase-locked with the external flow. Results are shown in Figure 3.6d. We observe a decrease in the entrainment region as the number of rowers in the chain increases. This effect is more pronounced when the density of the rowers increases. In the most extreme cases, the chain does not entrain with the flow, which is consistent with the experimental data. It is worth noting that, for a given velocity, the smaller chain of rowers is entrained for a much broader range of frequency ε than what is observed experimentally, i.e. the rower model overestimates the susceptibility of cilia to external flow. The simplicity of the model means it does not make sense to try to be quantitative. However, it captures well the qualitative trends observed in the cilia. For a complete description of the simulation methods, we suggest Dr Hamilton's PhD thesis [177].

3.6 Discussion and conclusions

In the present work, we provide the first experimental proof of entrainment of mammalian multiciliated cells by hydrodynamic forces. From this main experiment, we combine experimental and theoretical approaches to understand the mechanism that leads to cilia synchronisation in the single multiciliated cell. Each cell has a variable number of motile cilia that are able to reach synchronisation in frequency through an unknown mechanism of coupling. Studying this coupling is useful for the comprehension of the large scale problem, where thousands of multiciliated cells arranged in packed epithelia display metachronal coordination.

Firstly, we measured the hydrodynamic forces required for entrainment of cilia in isolated multiciliated cells. We found that multiciliated cells with few cilia (from 1-5) are very responsive to external oscillatory flow and can be entrained by a fluid flow around $v_{\mathrm{EX}} = 200\mu$m/s. The magnitude of this flow is similar to the one that a cilium can generate during its power and recovery strokes [85] and to the total net flow generated by ciliated cells in the brain [39]. We showed that the entrainment strength of a cilia bundle decreases with their number as we would expect for hydrodynamically coupled cilia. The forces applied by the external flow on each cilium are hydrodynamically screened by the beating cilia nearby, so each cilium feels a lower drag than when isolated. This trend is quantitatively described by a model that assumes the group of packed cilia to behave hydrodynamically as an impenetrable rigid rod with an effective radius (that depends on the number of cilia) and each cilium beating driven by an average constant force, [167]. From the fit of the data with the model, we estimate the beating efficiency of the cilium in agreement with past works with other ciliated organisms [106].

Secondly, we measured that multiciliated cells with a higher number of cilia were on average beating with larger CBF. Again, we could quantitatively describe this trend with cilia effective drag reduction by screening effects and interciliary dissipation. The CBF increase was not affected after depolymerisation of the cell actin network, supporting the hypothesis that the measured effect is not driven by the elastic forces transmitted through the cytoskeleton. Moreover, we argue that steric interactions between cilia could not be responsible for the observed trend (see Appendix B.2). Arguing that CBF increase has only hydrodynamic origin, we estimated the cell-driven flow that is acting on each cilium in a synchronised multiciliated cell. We found that this flow is quantitatively sufficient to entrain the motility of each cilium within a cell.

To further verify the importance of hydrodynamic forces, Dr Hamilton carried out simulations of motile cilia studying the effects of cilia number and external flow, within the minimal model of rowers. In this model, actively driven oscillators interact only through the fluid flow that they create themselves by oscillating. We found that the trends of the simulation results match the experiments on live cilia. Specifically, simulations predict an increase of the CBF with the number and density of cilia that is similar to the one measured. Moreover, they show a threshold with the number of cilia above which the entrainment of a chain of rowers is not possible anymore, as observed experimentally.

While our results suggest an important role of hydrodynamic coupling, we can not rule out that other mechanisms are at play for the synchronisation of cilia from the brain. Biochemical or mechanical elastic coupling at the base of the cilia could also contribute to their coordination. In the algae *Chlamydomonas*, where the elastic coupling between cilia is important for the synchronization [87, 88], hydrodynamic forces required for entrainment were measured to be an order of magnitude higher than the physiological ones [65]. By contrast here we measure a high susceptibility of motile cilia to external flow, in the same order of the cilia-driven flow reported in the literature [94, 85] and quantitatively in agreement with the cilia-driven flow that we measured in a synchronised multiciliated cell. It is worth noting that we did not take into account that cilia in multiciliated cells are so densely packed that also steric interaction could play an essential role in their synchronisation. Investigating such effects from an experimental point of view is very challenging. Simulations of hydrodynamic interacting filaments where steric interaction (in the form of increasingly stiff repulsions) can be tuned and turned on and off seems a more amenable approach to unveil this fascinating question. Further experimental investigations are required to validate these results for other mammalian multiciliated cells. Particularly complex behaviours are expected from cilia propelling mucus, such as in the airways, where cilia beat in a non-Newtonian medium and are also tethered by mucins [43].

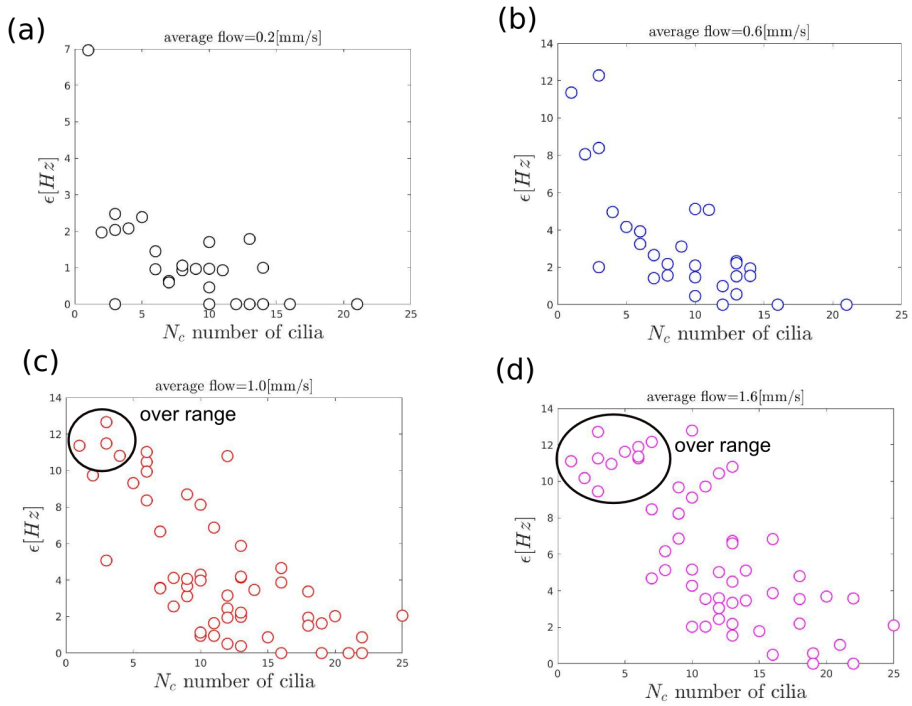

Fig. 3.7 **Supplementary figure on the synchronisation strength $\varepsilon(v_{\mathrm{EX}})$ for each cell as a function of the number of cilia per cell N.** Each plot shows data using a different external flow average velocity v_{EX} (shown on top of the graph). The points in the "over range" circle correspond to the cells that were entrained for the whole range (or nearly whole) of frequency spanned by the external flow.

Chapter 4

Investigating the role of external flows and viscosity in the alignment of cilia in the brain

4.1 Introduction

In the third ventricle cavity, cilia beating is highly organised in modules and gives rise to a spatiotemporally regulated network of fluid flows whose specific functions are still unknown [39]. Besides, it was observed that cilia orientation is not fixed after brain maturation, but reliably and periodically switches during day and night [39]. This observation is in contrast with the hypothesis reported in previous works [125], where cilia beating direction can be changed by hydrodynamic forces only while cilia are growing (*ciliogenesis*). These two conflicting results leave unclear which could be the mechanism that rules the cilia orientation switch found *in vivo*.

One of the main limitations of the experiments in [125] is that the value of the applied shear stress τ_0 was chosen on the basis of the estimated average flow produced by a ciliated cell in culture, $V \approx 50\mu$m/s at a distance of $h \approx 20\mu$m from the wall, leading to $\tau_0 \approx \eta V/h = 0.02$ dyne/cm^2. However, it was shown that cilia-driven flow *in vivo* have magnitude much higher than the one measured *in vitro*. In the third ventricles they have been measured $V = 100 - 500\mu$m/s [39], then leading to physiological shear stress up to an order of magnitude higher than the one applied by [125], $\tau \approx 10\tau_0 \approx 0.2$ dyne/cm^2 (1 dyne/cm^2 = 0.1 Pascal).

This new evidence motivated us to investigate whether cilia are responsive after complete differentiation to shear stress similar to the one experienced *in vivo*. Our results are described

in Section 4.3. Using our novel microfluidic setup, we found that cilia align with external flows at any day in culture, suggesting that cilia beating direction is not locked but still able to respond to flow also after maturation. These results are in agreement with what reported recently *in vivo* [39]. Moreover, we found that cilia alignment with external flow depends on cilia density that may have implications on the mechanism arising the complex flows network in the third ventricles.

Furthermore, we used our setup to investigate whether metachronal activity arises in cultures aligned with external flows. We found that ciliary beating frequency (CBF) is correlated for near ciliated cells, but this correlation decays at a very short mutual distance for both cultures treated and not treated with external flows. Similar results have been obtained using the Multiscale differential dynamic microscopy (Multi-DDM) technique [114], recently developed by our group to estimate cilia coordination in airway samples. Overall, our results suggest that ependymal cultures do not beat in a metachronal fashion also after alignment, Section 4.4.

Finally, in Section 4.5, we studied cilia alignment of cells cultured in medium with increased viscosity than water. When ependymal cells are grown *in vitro*, multiciliated cells are found to beat in random directions, but still with clusters of cells that spontaneously align in the same direction [125] as a result of hydrodynamic forces between cilia [80] or PCP pathways [126, 124]. Here, we varied the hydrodynamic strength between cilia by changing the viscosity of the medium. Then, we investigated the length-scale of these clusters of aligned cilia as a function of the altered viscosity. Our results suggest that hydrodynamic forces between cilia have a significant effect also on the scale of local ciliary alignment. Changes in the viscosity of the cerebrospinal fluid could then affect the complex cilia-driven flow patterns observed in the brain. Overall, our results highlight the importance of hydrodynamic forces between cilia and external flows in the brain at any age of development.

4.2 Methods

4.2.1 Cell culture and flow treatment

Differentiating ependymal cells were isolated from mouse brain and grown in Transwell-chips as previously described in Section 2.2.1. Ependymal cells differentiation *in vitro* into ciliated cells is achieved after approximately 10 days *in vitro* after cell seeding (DIV) [151, 125]. We treated cell cultures with shear stress for three days during and after cilia growth, specifically

at 5,12,19,26 days *in vitro* (DIV). We used the constant flow setup described in Section 2.4.1. A schematic of the fluid setup is also reported in Figure 4.1. During the flow treatment, cell culture plates are placed at 37 °C and 5% CO_2 using a conventional incubator or using a custom cell-chamber. After flow treatment, cells are removed from the flow setup, and cilia motility is imaged with a microscope. For the experiments described in the last section of this chapter, cells are grown in glass coverslips, and they have not been exposed to any external flow.

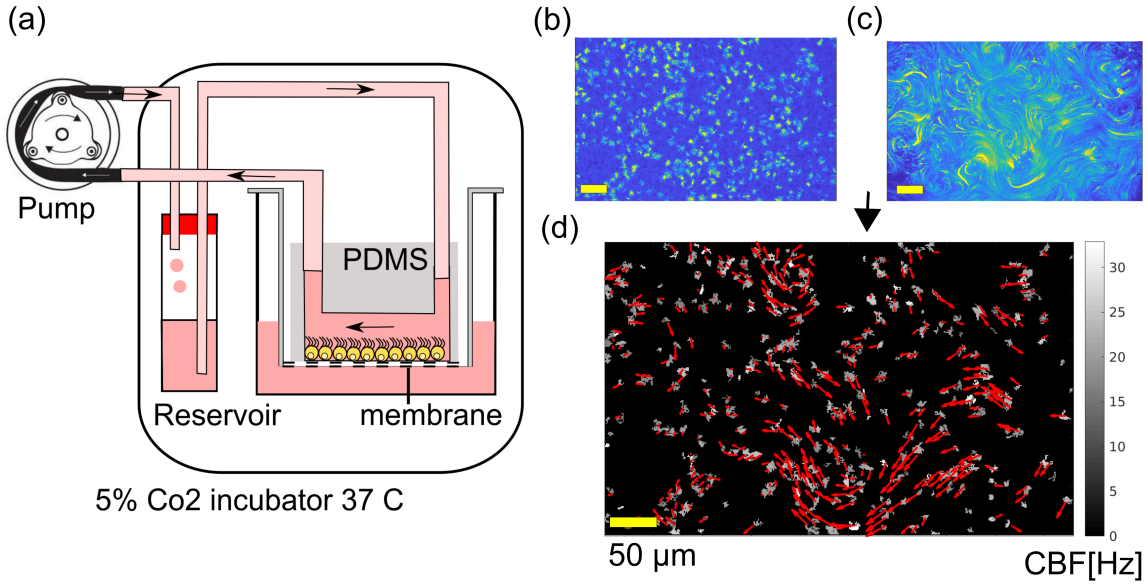

Fig. 4.1 **Experimental procedure for measuring CBF and cilia beating direction in ependymal cultures treated with fluid flow.** Continuous fluid flow is applied for three days on cells cultured in Transwell-chips. Then, the chips are removed from the flow and cilia motility is imaged with the microscope. From high speed Bright Field movies, we identify ciliary beating frequency and cell position, while from tracer particles, we measure ciliary beating direction. (a) Illustration of the setup: shear stress is applied on cells through a closed medium cycle using a peristaltic pump and a medium reservoir. (b-c) Normalised standard deviation maps of the pixel intensity over time of a Bright field movie (b) and fluorescent microscopy images after the addition of tracer particles (same field of view) (c). The information from Bright field videos and fluorescent microscopy movies of cilia-driven particles can be joined in Figure (d). The colourmap indicates the ciliary beating frequencies (CBF) and the red arrows connote the measured flow field above the identified cells. The length of the arrows is proportional to the flow velocity. The experimental procedure is summarised in Video 6, available at https://doi.org/10.5281/zenodo.3689780

4.2.2 Image acquisition procedure

The image acquisition starts 1 hour after the Transwell-chips have been disassembled from flow setup. All videos are acquired with a microscope (Ti-E inverted Nikon, Tokyo, Japan) equipped with 20X objective, (NA 0.75, depth of field 1.8μm). During the imaging, cell cultures are always kept at 37 °, and 5% CO_2 using the custom made chamber.

1. Firstly, high speed BF images are acquired for several fields of view (FOV) for each chip. Each BF video is registered at 160 frames per second for 5 seconds. These videos record the dynamic of the cilia, and they will be then used to extract cell positions and CBF.

2. Secondly, fresh medium with PEG-coated fluorescent particles of 1μm diameter (particle dilution at 0.5 %) [178] is perfused in the chip using a syringe pump previously connected to the inlet of the Transwell-chip. Each chip is held stable in the wellplate using sterile tape in order to avoid drift of the chip during media perfusion. We wait 15 minutes after we stop media perfusion.

3. Finally, videos of the cilia-propelled fluorescent particles (FL) are recorded on the precedent FOVs (10 seconds at 10 frame per seconds).

In future terminology, I will use FL while referring to the videos of the fluorescent particles and BF for the bright field videos acquired before the addition of the particles. It is worth noting that CBF can not be extracted from the FL videos because particles move around the field of view hiding the cilia motion. For this reason, avoiding drift during particle perfusion is a critical step to have a precise mapping of CBF (from the videos before particles addition) and cilia beating direction for each cell.

4.2.3 Image analysis

For each field of view we have one BF and one FL video that are analysed with Matlab to obtain the following information:

1. **Cell position (first rough estimate):** using the BF video, cell locations are first roughly identified by the pixels for which the standard deviation of the intensity over time is larger than a threshold value (this is found with Matlab function using Otsu's method), Figure 4.1b.

2. **Ciliary beating frequency and cell position (refined) :** for each of the validated pixel, CBF is then calculated as the frequency with the highest peak in the FFT signal of pixel intensities over time [165, 166, 72]. Single multiciliated cell can be identified as the group of connected pixels where the frequency standard deviation does not vary more than a threshold $\sigma_f^{max} = 1$ Hz. This information also provides another way to distinguish background noise from cilia signal, and therefore, an additional filter for the identification of cell locations, Figure 4.1d.

3. **Ciliary beating direction**: Here, we assume that the generated cilia-driven flow corresponds to the beating orientation of underlying cilia. This assumption was recently validated in [39]. The fluid flow generated by the ciliated cells is measured from the FL video using particle image velocimetry software PIVLab, Matlab [179]. Particle image velocimetry (PIV) algorithm is able to extract a displacement vector field between two consecutive frames. Description of the algorithm is in Figure 4.2. For the PIV measurements, we use a grid with a spacing of 32 pixels (7.6 μm), that it is roughly the size of a ciliated cell. For each FL video, we have a series of displacement vector fields that are then averaged over time to obtain a smooth result of the flow field.

4. **Joining the information**: For each vector of the flow field, we have a corresponding box (7.6x7.6 μm^2). We only keep the boxes that are covered for more than half by identified ciliated cells (using the thresholding method of points 1 and 2). Then, for each selected box i, we have: (i) the CBF, using the average CBF inside the box; (ii) the beating direction $\tilde{v} = \vec{v}_i/|v_i|$, where v_i is the measured flow field. The size of the box is roughly the size of a cell. For this reason, we can assume that each box corresponds to a single multiciliated cell, although this is not rigorously true. The experimental procedure is summarised in Video 6, available at https://doi.org/10.5281/zenodo.3689780

Overall, combining the image analysis of videos of cilia motility and tracer particles, we can routinely measure ciliated cell positions, beating frequency and direction over all the investigated FOVs (Figure 4.1d).

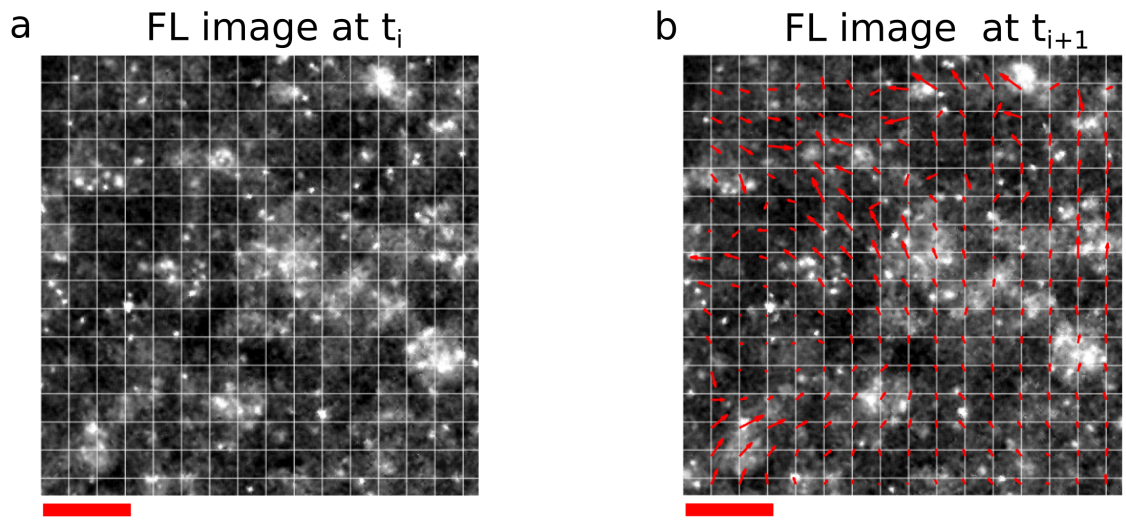

Fig. 4.2 **Using particle image velocimetry (PIV) to measure cilia-driven fluid flow from videos of tracer particles.** PIV can be used to measure the displacement field of the tracer particles between two consecutive frames of a video. The acquired FL images are first pre-processed to maximise their contrast. Each image t_i is divided into several small subregions of 32x32 pixels (7.6x7.6 μm^2) (a). Then each subregion is correlated with an interrogation area in the consecutive frame t_{i+1} (b) in the direct or Fourier space. The position of the peak of the cross-correlation yields the displacement of the particles in the subregion between the two frames examined. The procedure is repeated for each subregion of the image, and a displacement vector field is obtained. Successively, the field is post-processed following two steps: (i) vectors that have magnitude larger than a threshold are removed, (ii) the vector field is then interpolated in these points. The red arrows in (b) represent the validated vector field from these pair of images (b). Scale bar 30μm. Examples of the video used for the PIV are Video 6 and Video 7, available at https://doi.org/10.5281/zenodo.3689780.

4.3 Cilia alignment with external flows

4.3.1 Alignment of ependymal cilia is independent from days in culture.

We applied constant shear stress $\tau \in [0.1, 0.8]$ dyne/cm^2 on maturating (5-8 DIV) and mature (DIV>14) ependymal cells for 3 days. Our objective is to measure whether *in vivo* physiological shear stress could induce alignment in completely differentiated ependymal cells [125]. Ependymal cells are considered mature after DIV 10 [125]. Constant flow is applied on cell grown in Transwell-chips with straight or tapered channels. Tapered geometry allowed to have different levels of shear stress in the same culture, maintaining a constant flow rate [180]. The width of the channel increases as a function of the axial position x,

and this lead to a hyperbolic shear stress along x, $\tau = (6\eta Q)/(h^2 w)$ with $w(x) = w_0 + \alpha x$, Figure 4.3c. See Section 2.3 for more details on this formula. By contrast, in the straight channel geometry, the shear stress is a constant along the axis and permits to gather a larger number of data from cells in the same shear conditions. We applied external flows on 4 chips (2 straight and 2 tapered) for each cell age (5,12,19,26 DIV), for a total of 16 chips. Besides, we used the same number of chips as control.

After 3 days of constant shear flow, the Transwell-chips are disassembled from the flow-setup and imaged with and without tracer particles. We acquired BF and FL movies on 12 and 20 FOVs respectively for each chip with straight and tapered geometry. For each identified ciliated cell i, we measured the CBF and the cilia-driven flow $\vec{v}_i$ in the complete absence of any external flow (see methods in Section 4.2). The absence of external flows ensures that the observed flows are only generated by cilia. We measured the global cilia alignment using the following expression

$$\Phi = \frac{1}{N} \sum_{i=1}^{N} \tilde{v}_i \cdot \vec{e}, \tag{4.1}$$

where $\tilde{v} = \vec{v}_i/|v_i|$ is the normal vector pointing in the direction of the cilia-driven flow, $\vec{e}$ is the normal vector pointing in the direction of the previously applied external flow and N is the total number of boxes where ciliated cells are detected. Again, during these measurements, there is no external flow applied, and $\tilde{v}_i$ is only cilia-driven. For $\Phi = 1$, cilia beating directions completely aligned with the applied flow, while $\Phi = 0$ when cilia are randomly oriented. For control cells, the direction of $\vec{e}$ is arbitrary.

Over the examined range of shear stresses, we always found high positive values for the alignment Φ, independently on the culture age. In Figure 4.3a we show results for shear stress $\tau \approx 0.8$ dyne/cm^2. In the direction of alignment, cilia beating generates a net average flow $\overline{V} = \sum_{i=1}^{N} \frac{v_i \cdot \vec{e}}{N}$ that we report to be $\overline{V} \approx 50\mu$m/s for mature cells at DIV >15, while is $\overline{V} \approx 20\mu$m/s for cells DIV=8.

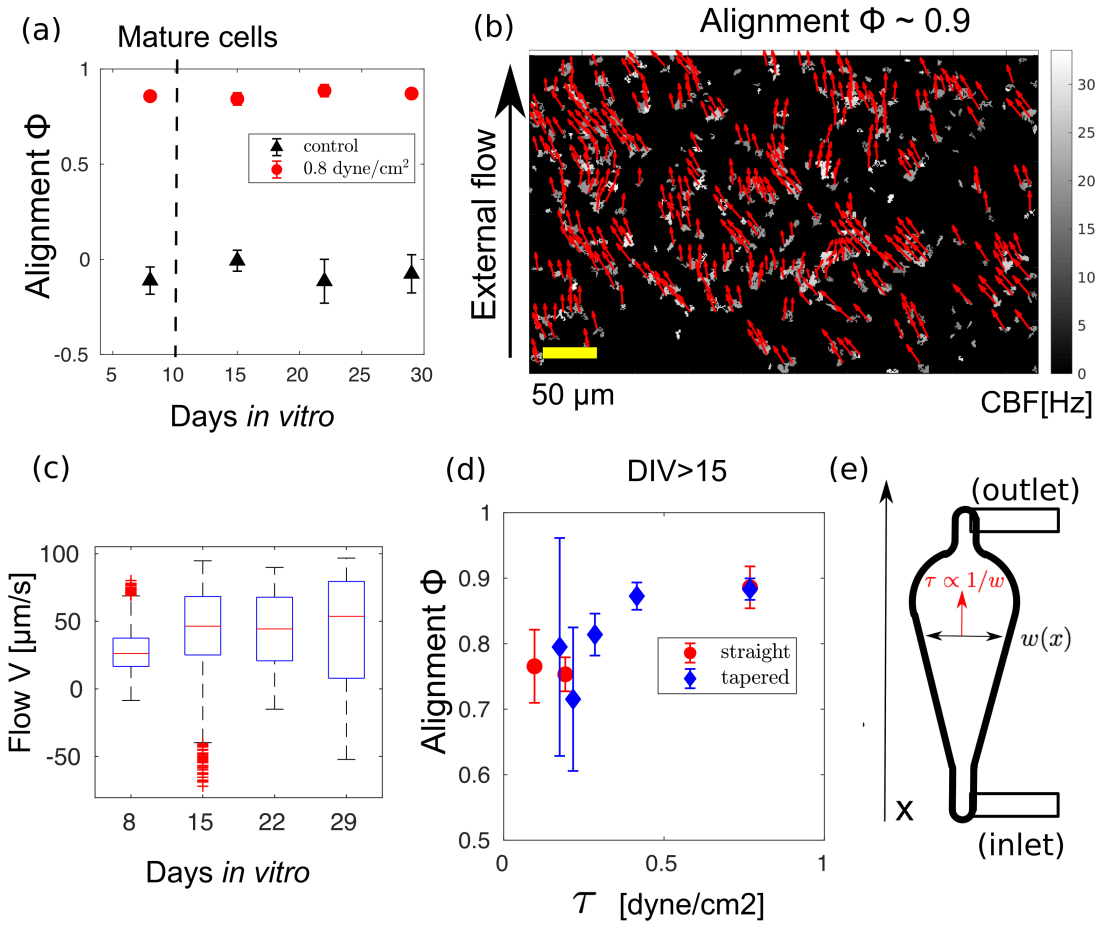

Fig. 4.3 **Ciliary beating strongly aligns with the external flow independently of the days in culture.** (a) Cilia alignment for cells treated with shear stress $\tau \approx 0.8$ dyne/cm^2 at different days *in vitro*. Each point is obtained by averaging alignment values obtained from straight (2 cultures) and tapered (2 cultures) channels. Error bars are standard deviations of the average. (b) Analysis results for a field of view of a culture at 29 DIV and treated with $\tau \approx 0.8$ dyne/cm^2. Video of the propelled particles, Video 7, available at https://doi.org/10.5281/zenodo.3689780 (c) Average cilia-driven flow V in the direction of the applied shear stress as a function of the culture age (the measurement is in the absence of any external flow). Differentiated cells at DIV>15 propel an average fluid flow that is roughly the double of differentiating cell at DIV 8. Same dataset of (a). (d) For mature culture (DIV>15) ciliary beating direction align significantly for all the explored range $\tau \in [0.1, 0.8]$ dyne/cm^2. The alignment slightly increases when higher shear stresses are applied. Data from cells cultured in tapered channels (blue) agrees with the one obtained for straight channels (red). The standard deviation for cells grown in the tapered geometry is higher probably due to the lower statistics. (e) Illustration of the tapered channel used to apply different shear stresses in the same cultures. The shear stress decreases along the main axis of the channel (x) as the channel width w increases. Movies were recorded only along the centerline of the tapered channel. The alignment Φ has been averaged over continuous segments of size $\delta x = 1700 \mu$m.

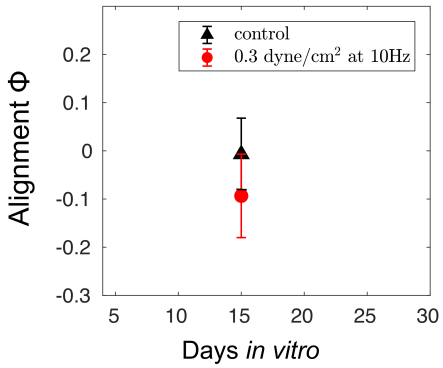

Fig. 4.4 **Cilia do not align with oscillatory flow.** Ependymal cells were exposed to oscillatory flow at DIV 15 (3 samples + control) for 3 days at average shear stress during half cycle of $\tau \approx 0.3$ dyne/cm^2. For all the samples no significant alignment was measured. For a description of the setup to create alternated flow see Chapter 2.

The global alignment slightly decreases for culture treated with lower shear stress, but it is always significant in all the applied range. In Figure 4.3d we report the average alignment as a function of the applied shear for mature cells (DIV>15).

The lower alignment $\Phi \approx 0.7 \pm 0.1$ was for $\tau \approx 0.2$ dyne/cm^2, while the alignment reaches a peak of $\Phi \approx 0.87 \pm 0.01$ for $\tau \approx 0.8$ dyne/cm^2. No significant difference was found for cells treated with similar magnitude of shear stress but grown in the tapered or straight geometry. Similarly to the *Xenopus* ciliated skin [123], no significant orientation was present on mature cells at DIV 15 after treatment with strong oscillatory flow (shear stress $\tau_{osc} = 0.3$ dyne/cm^2 during half cycle), Figure 4.4.

4.3.2 Cilia-driven flow and alignment depend on local cell density.

For each identified cell i we can extract a local density ρ_i by counting the total area occupied by neighbour beating cilia in the radius of $r_\rho = 40\mu$m around the cell, Figure 4.5a. The value of the examined radius is set by the typical mutual distance over which cilia beating directions become uncorrelated; in the next Section 4.4, we describe how this typical distance can be estimated. The average local density for mature cultures is approximately the double than for differentiating cultures at DIV 8, Figure 4.5b, in agreement with a culture undergoing *ciliogenesis* and previous works [125]. Cilia-driven flow increases with the local density, not in contrast with past theoretical works [68], Figure 4.5.

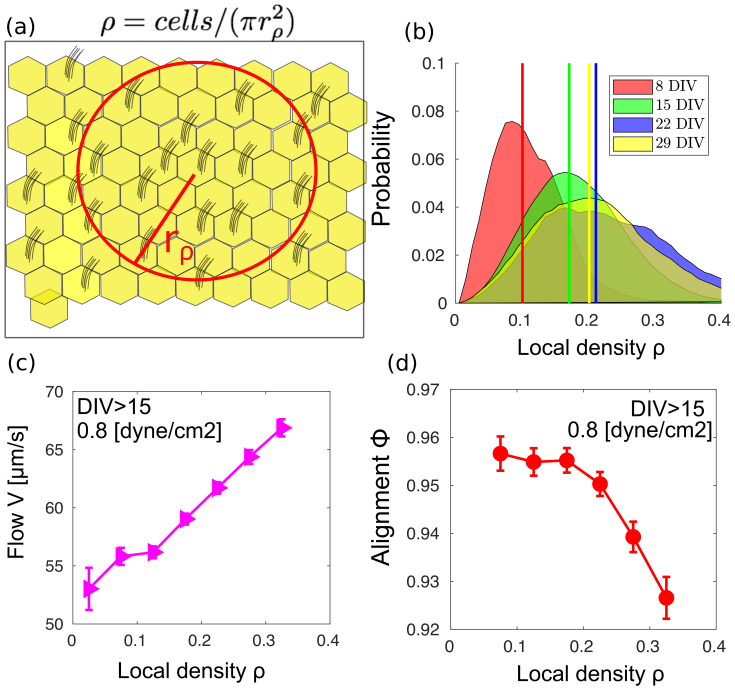

Fig. 4.5 **Cilia generated flow and alignment depends on the local density of cilia.** (a) Illustration of how local density ρ is measured in ependymal cultures, where not all the cells are ciliated. We count the number of pixels where cilia were detected in a circle of radius r_ρ around the cell i and we divide this number by the area of the circle (in pixels) to obtain a local density ρ_i. (b) Distribution of ρ in culture with different age. Differentiating culture at DIV 8 have cells with a lower local density that culture at DIV$>$ 14. (c) Cilia powered flow increases as a function of the local density of cells. Median binning of the flow velocity, V, in the direction of applied shear as a function of the local density ρ. Error bars are standard deviations of the average binning. (d) Ciliary beating alignment with the external flow decreases with the local density. Points are median binning of the global alignment, Φ, as a function of the local density ρ. For both (c) and (d), we show data from all the cultures treated with $\tau = 0.8$ dyne/cm^2 and at DIV$>$ 14. Error bars are standard deviations of the median binning.

Most strikingly, we found that cilia alignment with the external flow depends on the local density of cells. The alignment parameter $\Phi \approx 0.96 \pm 0.01$ for the most isolated ciliated cells, $\rho = 0.1$, while $\Phi \approx 0.92 \pm 0.01$ for cells located in the most crowded ciliated area $\rho = 0.3$, Figure 4.5d. These results are in agreement with what we found in Chapter 3, where we showed that single ependymal multiciliated cells respond to external flow in a way that it is strongly dependent on the number of cilia per cell. Specifically, the hydrodynamic screening of dense cilia makes the entrainment of multiciliated cell with an oscillatory flow weaker as the number of cilia per cell increase. On a larger scale, we would then expect that also the forces applied by a constant external flow would be dependent on the multiciliated cell

density, with consequences on their alignment. Although statistically significant, the effect that we measure here is small. A possible reason is that these ependymal cells were exposed to shear stress for a long time (3 days) to increase the chance to align ciliary beatings, thus saturating their response to external flow. In future works, it would be beneficial to investigate this trend using the minimum shear stress necessary to align cilia.

4.3.3 New insights in cilia response to fluid flow the and future works

In apparent contrast with [125], we showed that cilia from mouse ependyma could respond and align to physiological shear stress found *in vivo* also after complete *ciliogenesis*. Strikingly, we measured that the alignment with flow depends on the local density of cilia - ciliated cells in denser clusters presented a lower alignment after shear treatment relative to more isolated cells. At the present stage, we can only speculate the latter trend is consistent with the results that we obtained in Chapter 3, where the hydrodynamic screening from nearby cilia reduces the entrainment of individual cilia with an oscillatory flow. This hypothesis needs further theoretical investigation. Previous works reported that cilia do not align with external flows after complete *ciliogenesis* [125]. From our observations, we can speculate that such effect is due to the increase in the density of ciliated cells during *ciliogenesis*, that in turn, it makes the alignment of cilia with external flows more difficult. In the present work, ependymal cells were exposed to shear stress for a long time (3 days) to increase the chance to align ciliary beatings and measure whether global alignment was possible after complete *ciliogenesis*. However, in future works, we aim to identify the minimum shear stress necessary to align cilia with the flow as a function of the cell density. Using cells $DIV > 14$ grown in a channel with a tapered geometry, we aim to apply shear stress $\tau \in [0.02 - 0.1]$dyne/cm^2 for three days. This value was chosen because no alignment was observed when shear stress of $\tau \approx 0.02$ dyne/cm^2 was applied on cultures at $DIV > 10$ by [125]. Then we will measure alignment and beating direction distribution as a function of density and applied shear. Moreover, we aim to run hydrodynamic torque calculations on beating cilia at different density in response to a constant external flow. Using the tracking of the beating pattern of a single cilium, we can calculate the torque exerted on it by external shear flows. Successively, we can compare the torque in the presence of nearby cilia beating with an identical pattern, with the same or different phase. This would help to compare cilia screening effect with our data.

Overall, our results suggest that temporally regulated cilia flow networks in the brain could be regulated by hydrodynamic forces between cilia themselves and between external flows at any age. The cilia direction switch that reliably and periodically occurs in the brain [39] could be then caused by time alteration of cilia activity or CSF production. Moreover,

we suggest that the density distribution of cilia in the brain could very well play an essential role in the establishment of complex flow networks and how they respond to CSF flow. Other researchers have already planned further theoretical investigation on how the cilia flow-response is affected at different ciliated cell density. How these flow highways arise in the brain, their function, and the role of Planar Cell Polarity are still fascinating mysteries that also need to be addressed in the future.

4.4 Frequency and orientation spatial coordination do not increase with global alignment.

4.4.1 Spatial correlation of the cilia beating directions

In ependymal cultures, multiciliated cells are often found to be aligned in small clusters without any external polarisation signal [125]. Theoretical studies suggest that hydrodynamic coupling between cilia can lead to global alignment depending on the frequency and amplitude of cilia beat [80, 172]. In cultures, hydrodynamic forces between cilia may not be enough for global alignment but could be sufficient to produce the observed alignment at short scale [125]. This hypothesis is supported by previous works that found complete lack of cilia alignment for cells with impaired cilia beat [33, 125, 181, 133].
We measured the typical size of aligned clusters in cultures by studying the fluctuations in cilia beating direction respect to the average one, $\Delta\tilde{v}_i = \tilde{v}(r_i) - \tilde{v}_m$, where $\tilde{v}_m$ is the average beating direction and $\tilde{v}(r_i)$ is the beating direction of the cell in the position r_i. We define the correlation function of cilia beating direction by:

$$C_o(r) = \frac{1}{c_0^o} \frac{\sum_{i,j}^{N} \Delta\tilde{v}_i \cdot \Delta\tilde{v}_j \delta(r - r_{ij})}{\sum_{i,j}^{N} \delta(r - r_{ij})}, \tag{4.2}$$

where $\delta(r - r_{ij})$ is the Dirac delta function (this function is equal to zero everywhere except for the zero where $\delta(0) = 1$), and $c_0^o = \sum_j^N (\Delta\tilde{v}_i)^2$ is a normalisation factor and r_{ij} is the mutual distance between the ciliated cells i and j [182]. Large values of $C_o(r)$ indicate that orientation fluctuations are positively correlated, while $C_o(r)$ averages at zero for random and uncorrelated fluctuations. It is worth noticing that this analysis can also be performed on already aligned cultures (previously treated with external flows). The function $C_o(r)$ is used to extract the typical size over which the fluctuations of beating direction around the mean become uncorrelated. Figure 4.6a,b shows an example of correlation functions for cultures at DIV=15, treated and not treated with shear stress.

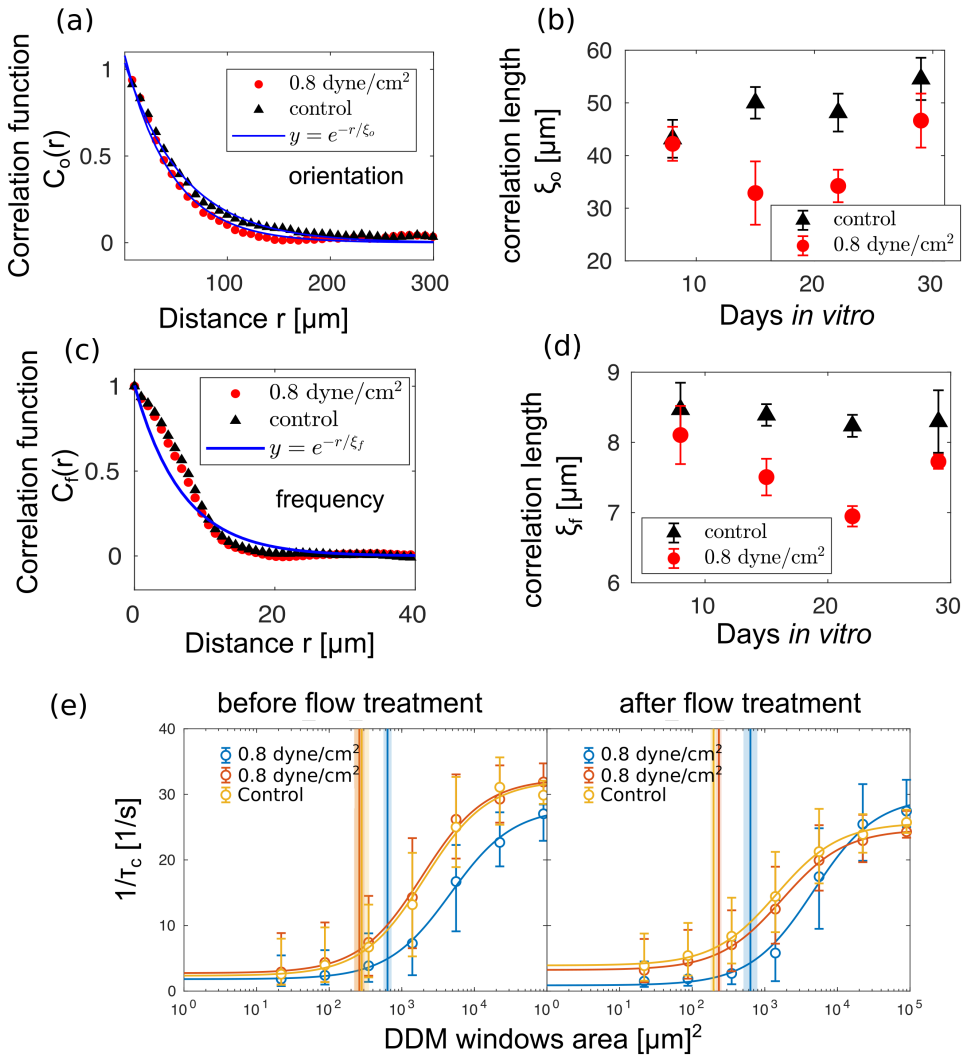

Fig. 4.6 **Spatial correlation of ciliary beating frequency and alignment in brain ciliated cultures aligned with flow.** (a) Correlation functions $C_o(r)$ of orientation fluctuations decay exponentially with the mutual distance between ciliated cells for both cultures treated with shear stress (and aligned) and control not aligned. The flow is always off when data are acquired. In both cases, these functions can be fitted with an exponential decay to extract a typical decay length ξ_o. (b) The typical lengths are around few times the size of a cell ($\xi_o \approx 40\mu$m) and do not change much with the culture age or when the ciliary beating are aligned. (c) Cultures treated with shear stress and controls do not show large scale frequency correlation. The correlation functions of frequency fluctuation $C_f(r)$ decay on a scale comparable to the size of a single cell ($\xi_o \approx 10\mu$m) for both cultures aligned and control. (d) The typical length ξ_f seems to not vary much also with culture age. Error bars are the standard deviation of the average. Each point is the average over more than 20 FOVs acquired from 4 chips for both (b)and (d). (e) Sigmoidal curve from Multiscale-DDM. The decay rate τ_c is the time scale at which beating coordination is lost in an analysed window. We show the median of the decay rate τ_c^{-1}(circles, whiskers showing 25th and 75th percentiles) measured at each tile area across several FOVs; then these data are best fitted with a sigmoidal curve. For each curve, the vertical line indicates the left shoulder of the fitted sigmoidal curve and gives a typical length scale ξ_{DDM} at which coordination between cilia is lost. We found no significant difference in ξ_{DDM} before and after the application of shear stress. Data are shown for 3 cultures (1 is a control).

We found that $C_o(r)$ can be fitted with an exponential decay $y = e^{-r/\xi_o}$, where the characteristic length ξ_o is a estimate of the typical size of an oriented cluster, Figure 4.6a. We measured $\xi_o \approx 30-50\mu$m, with aligned cultures having slightly lower values respect to control. This difference is not observed at all the age (DIV), suggesting that it may just be caused by slightly different growth condition, Figure 4.6b.

Overall, we use spatial correlation functions of the cilia beating direction to estimate of the typical mutual distance after which cilia beating direction becomes uncorrelated. The average value has been used in Section 4.3.2 to define the radius r_ρ for the measurement of local cilia density. In fact, in a circle of this radius, $r_\rho = \xi_o$ all the ciliated cells have an influence on the beating direction of the cell at the centre of the circle.

4.4.2 Spatial coordination of ciliary beating frequency

Metachronal waves require that cilia are all beating in the same direction. We investigated whether cilia alignment with external flows also induced the emergence of the metachronal activity or a sort of higher cilia coordination in ependymal cultures. Previous works investigated metachronal activity in ciliated carpets by spatially correlating the frequency and phase of each cilia [68, 69, 72]. However, cilia in ependymal cells are densely packed, and so it is challenging to measure the phase of individual cilia. Therefore, we firstly focused on the spatial correlation of the CBF. We then compared results with a novel image technique, Multiscale-DDM [114, 109] , that is able to extract cilia length scale of coordination from high-speed bright field videos.

Frequency correlation functions

We used the spatial correlation function of the frequency fluctuations to quantify a degree of coordination in our samples. Frequency correlation decays to zero at a certain mutual distance between ciliated cell; this trend can then used to estimate the typical cluster size of correlated beating cilia.

The frequency correlation function is calculated with the following expression [182]:

$$C_f(r) = \frac{1}{c_0} \frac{(f(r_i)-\overline{f})(f(r_j)-\overline{f})\delta(r-r_{ij})}{\sum_{i,j}^{N}\delta(r-r_{ij})}, \tag{4.3}$$

where $\overline{f}$ is the average frequency and c_0 is a normalisation factor defined as $c_0 = \sum_j^N (f(r_j) - \overline{f})^2$.

For both ependymal cultures aligned with flow and controls we record BF images over many fields of view (FOV), then for each FOV we extract cell positions and CBF as described in the Methods section 4.2. For each FOV the $C_f(r)$ is calculated using Equation 4.3. The correlation functions can be fitted with an exponential decay $y = e^{-r/\xi_f}$, that catch a sensible mutual distance ξ_f over which uncorrelated frequencies are observed. For both control and aligned cultures, we found that the correlations decay to zero above the typical size of a single cell ($\approx 10\mu$m). These results hold at any culture age. Figure 4.6c,d.

It is worth highlighting that frequency spatial correlation does not provide any information on the phase coordination of the cilia. Cilia beating with the same average frequency is not equivalent to synchronisation. Indeed, cilia could beat at the same average frequency but with an incoherent phase difference (no phase locking). For example, this could be due to high thermal noise. For this reason, this analysis has a substantial limitation on the identification of metachronal activity. However, the short spatial frequency correlations measured here are undoubtedly an indication that metachronal activity is not present in our samples.

Multiscale Differential Dynamic Microscopy

A recent video analysis algorithm named multiscale Differential Dynamic Microscopy (multiscale-DDM) [114, 109] has been developed to measure spatial and temporal coherence of cilia beat of airway cell cultures. This approach has been build on the recently invented technique Differential Dynamic Microscopy (DDM), that relies on the Fourier analysis of difference images (microscopy images) to acquire information about dynamics in a sample [183]. For example, in the case of colloidal particle diffusion, this method gives the same information usually accessed by dynamic light scattering [184]. This technique can also be used on high speed videos of cilia motility to extract information on the collective cilia dynamics, such as average ciliary beating frequency (CBF), metachronal wave emergence and, most importantly, a decay time τ_c that is related to the coherence in frequency of cilia movement [114].

In order to measure whether alignment induced increased coordination of the ependymal cilia, we further analysed with DDM the Bright Field (BF) movies of cultures before the application of shear stress and after. For each Bright field movie, the algorithm measured characteristic decay rates t_c that is the typical time at which beating coordination is lost. An average t_c is calculated on windows of increasing size. Plotting the decay rates against their tile size on a semilogarithmic scale produces a sigmoidal dataset that works as a quantitative

measure of cilia coordination within a given culture. This extension of the DDM algorithm is called multiscale-DDM [114]. In Figure 4.6e, we show the sigmoidal plots obtained by using multiscale-DDM before and after the treatment with the external flow. Coordination is lost on windows of area $\xi^2_{DDM} \approx 200 - 500\mu\text{m}^2$ and so we have a typical cluster size of $\xi_{DDM} \approx 14 - 22\mu\text{m}$. Interestingly, the coordination lengths measured with Multiscale-DDM are always larger than ones we found using frequency correlation functions.

Conclusions

Both Multi-DDM and frequency correlation function analysis used here show that there is no significant difference between the length scale of cilia coordination ξ_{DDM} or ξ_f before and after the treatment with the flow. Therefore, in our cultures, global beating orientation does not increase cilia spatial coordination.

The density of multiciliated cells in cultures is lower than *in vivo*. In our cultures, we measured a density of $\rho_c \approx 20\%$. In contrast, the third ventricle of mice is almost fully covered by ciliated cells [39]. Hydrodynamic coupling between cilia increases when cilia are closer [85, 82]; therefore, cell density may play an important role in the achievement of global coordination and metachronal activity. Here, the low cell density found *in vitro* does not provide conclusive evidence whether metachronal waves can be found in the brain ventricles.

4.5 Effects of medium viscosity during cell differentiation

When ependymal cells are grown *in vitro*, clusters of multiciliated cells spontaneously align their beatings in the same direction [125], Figure 4.6a. The local alignment at cluster level could be orchestrated by biological pathways such as the Planar Cell Polarity [126, 124], or could be ruled by the hydrodynamic forces between cilia [80, 172]. In brain ventricles, past works highlighting that PCP protein Vangl2 is important for cilia orientation in response to flow; however, this protein does not seem to be involved in the process of biasing beating direction like in other organs [10]. For example, the authors of [125] reported that mouse mutants with impaired cilia (cilia were not able to generate flow) have multiciliated cells with basal bodies pointing in random directions, and showed complete absence of cilia alignment even on a short scale. This phenotype was observed although multiciliated cells displayed the proper asymmetric distribution of PCP proteins. Understanding the mechanism underpinning the local alignment could help to unveil the nature of how defined patterns of cilia-driven

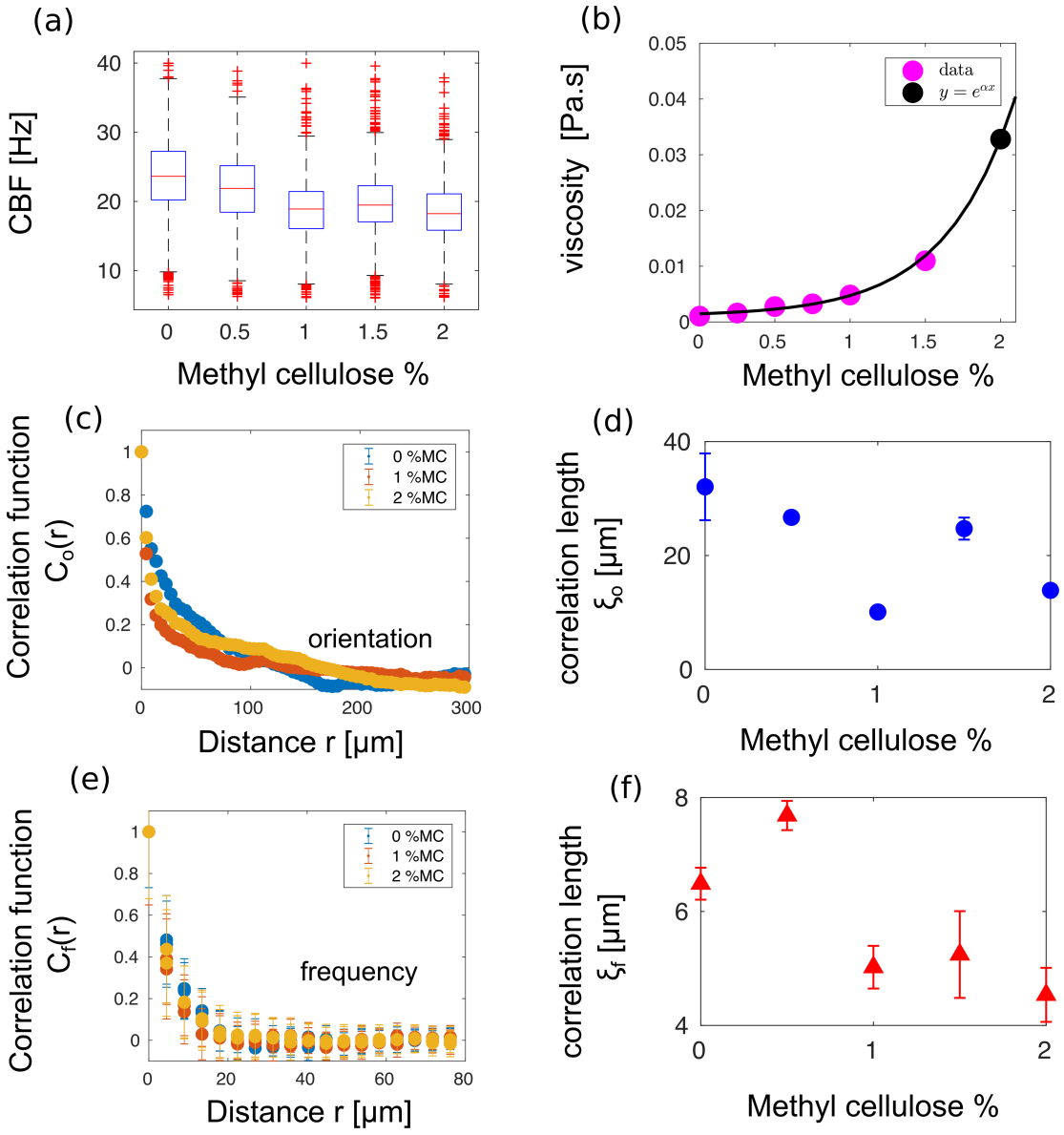

Fig. 4.7 **The effect of medium viscosity on ciliary beating frequency and orientation.** (a) Median ciliary beating frequency (CBF) as a function of the percentage of Methyl Cellulose (MC) in the culture medium. The bottom and top edges of each box indicate the 25th and 75th percentiles. Outliers as red crosses (b) Viscosity of the medium as a function of the MC. The viscosity was extracted from the diffusion coefficient of 1μm tracer particles, using DDM. The viscosity for MC concentration of 2% was extrapolated from an exponential fit of the data. (c) Correlation functions $C_o(r)$ of orientation fluctuations decay exponentially with the mutual distance between cells for all the cultures. In both cases, these functions can be fitted with an exponential decay to extract a typical decay length ξ_o. (d) The typical lengths decrease with the viscosity. Each point is an average of 16x2 independent measurements from 2 cultures. Errorbars are the standard deviation of the average. (e) Medium viscosity seems not to change the scale of beating frequency spatial correlation. The correlation functions of frequency fluctuation $C_f(r)$ decay on scale comparable to the size of a single cell ($\xi_o \approx 10\mu$m) for all the concentration of MC. (f) The typical length ξ_f for different concentration of MC. Each point is an average of 16x2 independent measurements from 2 cultures. Errorbars are the standard deviation of the average.

flow arise in the brain.

Theoretical works on models of cilia carpet have predicted that global polarisation of beating direction can arise from hydrodynamic forces between cilia. However, the transition from cilia randomly orientated to global aligned is possible only when hydrodynamic interactions between cilia are sufficiently large [80, 172]. The fact that global alignment is observed only at a small scale could be a consequence of the hydrodynamic forces not being sufficiently large. The authors in [80] estimated that the hydrodynamic forces between cilia increase linearly with: (i) the viscosity of the medium, (ii) the frequency of cilia beating and (iii) the difference of the areas covered during the effective and recovery strokes by each cilium.

Thus, at first sight, an increase of viscosity could lead the cilia to align over a large scale spontaneously [80]. However, it has been shown that the viscosity varies other variables of the cilia beating, such as ciliary beating frequency (CBF) and cilia waveform pattern. Previous authors have investigated the effect of viscosity on the coordination of fluid and mucus propelling cilia [30, 185]. They both reported a clear dependence of the beating frequency and metachronal activity on the viscosity of the fluid. Ciliary beating Frequency (CBF) decreases when the viscosity of the propelled fluid is increased. The metachronal wave direction changes from diaplectic to orthoplectic in water propelling cilia of (*Paramecium*) and in mucus propeller (frog esophagus) as viscosity increased. Metachronal waves can be distinguished either symplectic, antiplectic, dexioplectic, or laeoplectic, depending to whether the power stroke of their cilia is with, against, to the right of, or to the left of, the direction of movement of the waves. Orthoplectic waves are when the wave propagation and effective stroke are parallel (symplectic, antiplectic). When wave propagation and ciliary power stroke occur at right angles, metachronism is called diaplectic [67]. According to [186], the observed change in metachronal activity with fluid viscosity could be explained by a decrease in the temporal asymmetry of the ciliary beat due to the load increase.

From this scenario, an increase in viscosity could have multiple effects: (i) it could increase the hydrodynamic interaction between cilia [80]. (ii) it could decrease ciliary beating frequency (CBF). (iii) it could affect the cilia beating pattern, such as a reduction of temporal asymmetry between power and recovery stroke [186, 185], and so on the area where hydrodynamic forces act. Overall, it is not clear whether these combined effects would bring a lower or higher alignment of the cilia carpet. In the present section, we investigate the effect of increased viscosity on the coordination of mammalian cilia in the brain.

4.5.1 Experimental procedure and protocols.

Differentiating ependymal cells were isolated from mouse brain and grown in flask as previously described [151]. Then they were seeded in glass wellplates and left to differentiate for 14 days in DMEM medium with different concentration of Methylcellulose (MC), $0, 0.5, 1, 1.5, 2\%$ w/wt. The viscosity of the medium was measured using differential dynamic microscopy (DDM) with tracer particles [187], Figure 4.7b. After complete *ciliogenesis* at day *in vitro* (DIV) 14, we measured average ciliary beating frequency and beating directions (using PIV) in an area of 0.4x0.4 mm^2 for each culture by joining 16 field of views acquired with a 40X NA 0.95 objective (160 fps for 5 seconds for BF images and 10fps for 10 seconds for FL images). We used at least two cultures for each different viscosity. The fluorescent beads tend to aggregate when MC is present in the solution, thus decreasing the accuracy of the particle image velocimetry (PIV) analysis. Therefore for the measurement of beating directions, the culture medium was replaced with DMEM (without MC) and fluorescent tracer particles. Images acquisition and analysis are described more in details in Methods Section 4.2.

Methylcellulose (M7140-100G Sigma) powder is autoclaved in a Duran bottle with a magnetic stir bar. DMEM is then warmed to 50 °C using water bath made with a hot plate and added under cell culture hood to the powder to obtain a 6% MC w/w concentration and is stirred for 1 hour while cooling down. After that, DMEM was added in order to obtain a 2% w/w MC and left in the fridge overnight. Then, it is additionally diluted with DMEM to the desired concentration. In my case was 2,1.5,1,0.5 % w/w. The viscosity of medium with different concentration of MC is measured using polystyrene beads and DDM using sealing tape on glass-bottom Petri dish in the cell-chamber at 37 °C and humid air CO_2 5%.

4.5.2 CBF and cilia orientation correlation length decrease with medium viscosity

We calculate the correlation functions of the orientation fluctuations $C_o(r)$, Equation 4.2 [182] on each acquired FOV. For these we can measure the average size of locally oriented cell clusters as previously described in Section 4.4.

Figure 4.7c reports examples of the shape of these correlation functions. These can be fitted with an exponential decay $y = e^{-r/\xi_o}$, where ξ_o is a estimate of the typical size of the oriented cluster. We found ξ_o to decrease with the concentration of MC Figure 4.7d. For 2 MC %, $\xi_o \approx 10\mu$m, the size of a single cell.

Moreover, we found that the average CBF decreases as the viscosity medium increases, in agreement with other work on different organisms [30, 185], Figure 4.7a. While the medium with MC concentration of 2% is approximatively 40-times more viscous than the water, the measured change in CBF is relatively smaller, from 23Hz at water viscosity to 18Hz at 2 MC%. The frequency correlations functions (Equation 4.3) decay on a shorter length scale ξ_f when the concentration of MC is increased. These characteristic lengths are always comparable with the size of a multiciliated cell, $\xi_f \approx 10\mu$m, Figure 4.7(e-f).

Our results suggest that hydrodynamic forces between cilia have a significant effect on the scale of local ciliary alignment. In particular, we measured that the orientation fluctuations become uncorrelated more rapidly with the mutual distance for cells grown at high viscosity. Further investigations of the cilia beating pattern are essential to understand whether this effect comes from the decrease of temporal asymmetry in the cilia beating waveform. With the present data, we can not exclude whether MC has an effect on the establishment of PCP asymmetric localisation, as this also needs to be addressed in the future.

Chapter 5

Investigating airway cilia alignment with external flows

In the airways, the aligned beating of motile cilia is essential for mucus transport toward the pharynx, see Section 1.2. Random cilia orientation can block mucus transport, leading to bronchiectasis and chronic sinusitis [31, 32, 115]. Alignment along the oral axis requires multiciliated cells to break the planar apical symmetry of the epithelium; how this polarity is established is still not known [13].

In mouse airways, cilia grow and establish a common beating direction in the period spanning from embryonic day 16 to the first postnatal days [10, 188], see also Section 1.4.2. Basal bodies dock at the cell membrane during the embryonic phase, and they show a significant bias in the oral direction [10] immediately. Differently from cilia in the brain, this initial polarity was also observed in mutants with impaired cilia motility. This evidence suggests that cilia motility and cilia-driven flow are not involved in the initial bias [133]. The polarisation signal that leads this initial orientation is not known [131]. PCP pathway and cilia direction have been reported to be influenced by mechanical forces in other systems [134, 125], therefore mechanical cues such as fetal breathing flow [189] and strains happening during embryogenesis could be involved in this process in the airways [10, 135, 136]. Successively, during the first postnatal months, basal bodies direction refines towards the oral direction. It is a current hypothesis that cilia-driven flows or external forces act in this process of direction refinement [10]. This hypothesis is motivated by the recent works on ependymal brain cells [125] and *Xenopus* [123], that showed cilia being able to align in the direction of physiological shear flow during *ciliogenesis*. Yet, clear evidence that airways cilia respond to hydrodynamic forces is still missing.

Cilia in the airways are constantly exposed to shear stresses due to the movement of air during inhalation and exhalation. A pertinent question to ask is whether these forces affect the establishment or refinement of cilia orientation.

Measuring the shear stresses caused by tidal breathing is experimentally very challenging. Computational fluid dynamics simulations provide a way to estimate airflow profiles in the airways form simple to complex physiological geometries that are based on micro-computed tomography scans [190]. These studies reported that airway wall shear stress varies little with airway generation in the lung [191, 192, 190] and it is of the order of $\tau = 0.45$ dyne/cm^2 during normal breathing [192, 190], but can reach up to 3 dyne/cm^2 in the nasal cavities [191].

In previous works, shear stresses on the physiological range of tidal breathing were applied to airway cultures. It has been shown that phasic shear stress increases mucin secretion [193] and induce ATP release. In turn, ATP release increases ciliary beating frequency (CBF) and decreases airways surface liquid (ASL) absorption [192, 191]. In Figure 5.1, we show that physiological shear stresses and ATP concentration indeed significantly increase CBF also in our airway cultures. However, these previous works did not investigate whether shear flow induced alignment in cilia dynamics. This question has been done recently by [137], where airway cells grown in microfluidic flow chamber have been exposed to controlled unidirectional shear stress 0.5 dyne/cm^2 for 24 hours during different timepoints of the *ciliogenesis*. From past studies on ependyma cells and *Xenopus*, *ciliogenesis* is indeed the only time window when cilia can change their direction [125, 123]. The cells treated with airflow showed cytoskeleton rearrangement; however, cilia alignment was *not* observed. Then, the authors concluded that it might be useful to expand the treatment time to more days or even to the complete *ciliogenesis* to assess the response of airways cilia to flow [137].

Motivated by these works [137, 125], we first investigated the effect of physiological air shear stress on airway cells during the entire period of cell differentiation. Moreover, we mimicked the effect of shear stress from fetal breathing on young airways cilia using fluid shear stress. At the current stage, the reported results are only preliminary, and further investigations are required to draw firm conclusions. Overall, we provide relevant insights and experimental protocols that may be useful to tackle this fascinating question in the future.

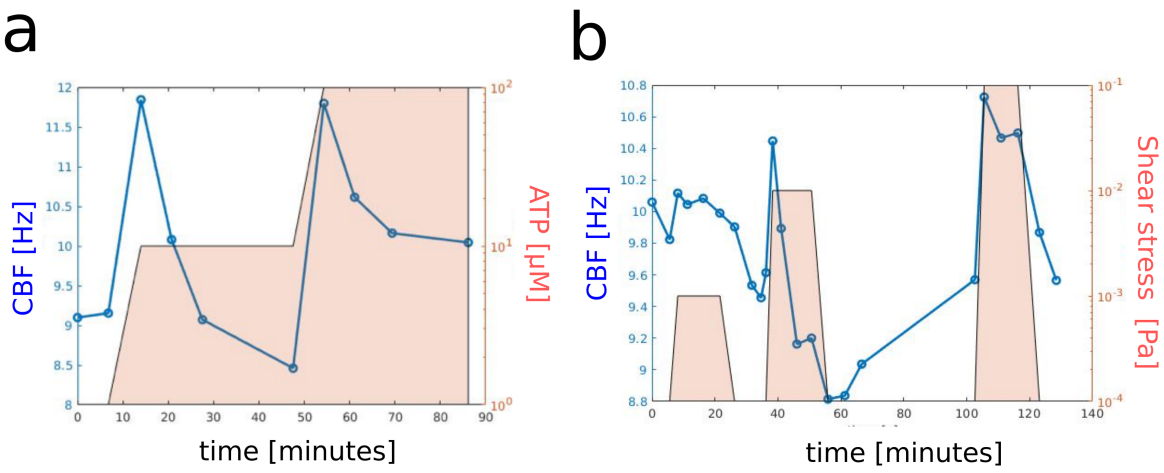

Fig. 5.1 **Exogenous application of ATP in cell medium increases CBF in airway cultures. Moreover, physiological shear stress induces the release of ATP that, in turn, increases CBF.** (a) Average CBF reaches a peak after the addition of 10 μM exogenous ATP in the cell culture medium and then comes back to the initial value after approximatively 30 minutes. The CBF reaches a peak again when more ATP is added (100 μM), then it drops and flattens out. CBF was measured from microscopy videos of 6 field of views acquired at regular time intervals (we always used the same fields of view). We perfused the medium with exogenous ATP from the inlet of the Transwell chip using a syringe pump at a low flow rate. (b) Measured CBF during the application of 10 minutes of fluid shear stress. This number reaches a peak when shear stresses of 0.01 Pa and 0.1 Pa are applied. CBF does not vary much when we applied the lowest shear stress of 0.001 Pa. Shear stress was induced by perfusing warm medium in the inlet of the Transwell chip using a syringe pump. Between each shear flow treatment, we waited at least 10 minutes. Shear stress values were calculated from flow rates using Equation 2.2.

5.1 Cilia response to prolonged air shear stress

Mouse airways epithelial cells (maec) grown in Transwell-chips with rectangular channel (height and width $h = w = 1$mm) were perfused with humid airflow rates of $Q = 5$ml/min and $Q = 25$ ml/min (two chips in series for each flow rate) during all the period of *ciliogenesis*. For mouse cells, this period spans 15 days: from air-liquid interface (ALI) day 1 to air-liquid interface (ALI) day 15. In contrast, *ciliogenesis* lasts 4 or 5 weeks for human airways cells. The airflow setup is described in Section 2.4.3. For airflow rates $Q = 5$ml/min and $Q = 25$ ml/min, the generated shear stresses (at the centre of the channel) are $\tau_w \approx 0.26$ and 1.3 dyne/cm^2 respectively. These values are comparable to physiological shear stresses acting in the airways caused by normal and accelerated tidal breathing [192, 190].

For each flow rate Q, the air flowing into the channel is simulated with COMSOL software. The shear stress is then calculated with the Equation 2.1 from the speed profile. Simulations were performed assuming air as incompressible fluid and laminar flow regime. The last assumption is reasonable for Reynolds number $Re < 2300$. We measured Reynolds numbers to be $Re \approx 5$ and 25 for inlet airflow rates of $Q = 5$ and 25 ml/min respectively, validating our assumption of laminar flow. These values are calculated with the formula [157]:

$$Re = \frac{\rho v D_H}{\mu},$$

where $\rho = 1.12\text{Kg/m}^3$ is the density of humid air, v is the average velocity of the airflow that we can assume $v = Q/(wh)$, $\mu = 19\mu$Pa.s is the viscosity of humid air at 37 C °and finally $D_H = 2wh/(w+h)$ is the hydraulic diameter of the channel. An example of the simulated airflow speed and shear stress are shown in Figure 5.2a-b. Cells were disconnected from the flow setup for medium changes and mucus washings every other day.

Cell viability and differentiation was comparable for controls and cells treated with $Q = 5$ ml/min, (shear stress $\tau_w \approx 0.2\text{dyne/cm}^2$). The CBF was not significantly different between the two, with the average value slightly lower for the cells treated with flow respect to control, see Figure 5.2e. By contrast, the viability for cells treated with $Q = 25$ ml/min (shear stress $\tau_w \approx 1.3\text{dyne/cm}^2$) was very low and no ciliated cells were observed on both replicas under inspection with the microscope (data not shown). The observed low viability suggests that prolonged exposure to not-physiological air shear flow is fatal to the cells. We then added medium with fluorescent particles of diameter 1μm to measure whether cells treated with $Q = 5$ml/min aligned with the flow. Although their average CBF was not significantly lower than controls, we found these cells were not able to move particles in both replicas, Figure 5.2d. By contrast, control cultures were able to propel tracer particles over large distances, Figure 5.2c.

Previous works applied 0.5 dyne/cm^2 air shear stress on airways human cells for 24 hours, and they observed that cilia were still able to propel particles as in controls [137]. On the contrary, we found that exposure for 15 days of similar air shear stress significantly modified cilia functions, although it did not interfere with cell differentiation. Air humidity, temperature and flow rate were constantly measured by digital sensors. We did not find any value significantly different from the reference ones for all the period of the experiment. A possible hypothesis is that the shear flow may have permanently altered the properties of the mucus and PCL. Past works reported that air shear stress induces an increase in the production of mucus and a drop in the absorption of the ASL [191]. Therefore we can not exclude that

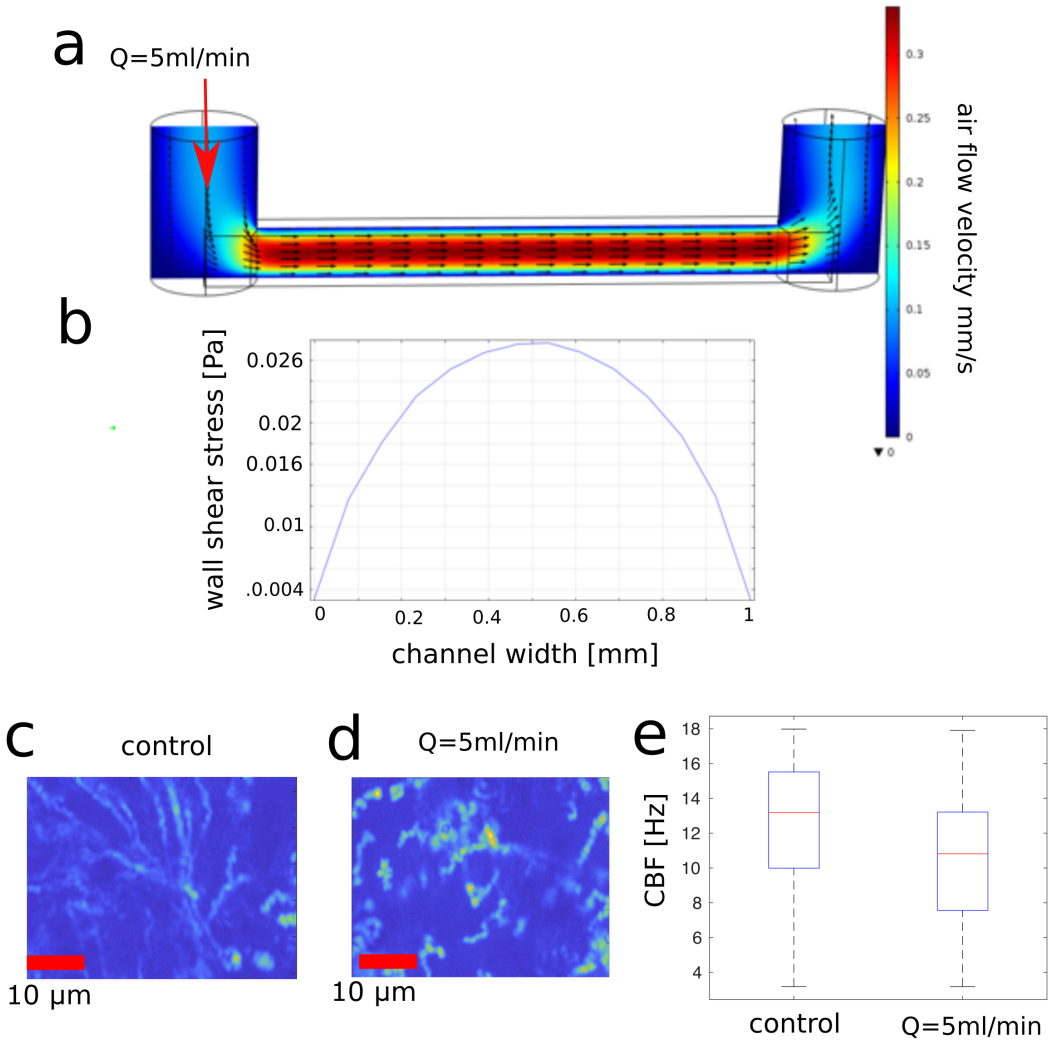

Fig. 5.2 **Cells treated with physiological air shear stress are not able to propel particles, although their average CBF is not significantly lower than controls.** (a-b) Colour maps made from the standard deviation over time of the pixel intensities of microscopy movies with tracer particles. Bright pixels indicate the passage of tracer particles. We show colour maps for cultures treated (b) and not-treated (a) with air shear stress. (b) Tracer particles oscillate around a mean position without being moved for large distances. By contrast, the tracers particles above control cells are propelled nicely, visualised by the long trajectories (a). Scale bars: 10 μm. Microscopy videos were acquired at 10 fps for 10 seconds. (c) Ciliary beating frequency (CBF) for cells treated with airflow rate $Q = 5$ml/min and control cells. The bottom and top edges of each box indicate the 25th and 75th percentiles. The two values are not significantly different. (d) Airflow velocity in the channel when a flow rate of $Q = 5$ml/min is perfused in the Transwell-chip. The flow speed is calculated with COMSOL software. (e) Calculated shear stress along the width of the channel for airflow rate $Q = 5$ml/min. Units of 1 Pa = 10 dyne/cm^2.

the PCL, where cilia beat, had been permanently modified by constant abnormal production of mucus and liquid absorption. For example, ciliary beating is impaired in diseases such as Cystic Fibrosis (CF), where the dehydrated top mucus layer compresses the PCL [43].

The use of air shear flow is an obligated choice when dealing with *in vitro* airway cultures because mucociliary differentiation is triggered by the establishment of an air-liquid interface [137, 144]. However, the use of airflow has two main limitations for our study: (i) the transmission of shear forces from the flowing air to the cells is complicated by the viscoelastic properties of mucus, whose composition is also altered by the shear response of secretory cells [191]. Secondly, (ii) *in vivo* air flows acts only postnatal, while *ciliogenesis* and alignment start during embryogenesis when the multiciliated cells are submerged by fluid.
Therefore, the timing of initial cilia orientation is not consistent with the beginning of airflow in the airways. By contrast, fluid shear flow from fetal breathing acts in the airways during the initial cilia polarisation[189]. For these reasons, we decide to apply shear stress on airways cilia by using fluid flow, similarly to Chapter 5. Since cells are submerged into the culture medium, the mucus would be diluted into the bulk and would also simplify the application of shear flows.

5.2 Cilia response to fluid shear stress

The loss of mucociliary differentiation *in vitro* is the major problem faced when fluid flows are applied to airway cultures during *ciliogenesis*. Following gold standard protocols, the differentiation of primary murine and human airways basal cells into secretory and ciliated is induced by an air-liquid interface (ALI), see Section 2.2.2. Differentiation *in vitro* is inhibited when cells are cultured under submerged conditions, and this fact is a significant difference between the *in vitro* and *in vivo* systems. In mammals, mucociliary differentiation starts during development, when the airways are fulfilled with amniotic fluid [10].

However, recent results have shown that the mechanism by which submersion prevents *ciliogenesis* is related to the resulting hypoxic environment [144]. The deficiency of oxygen keeps active the Notch signalling which represses genes necessary for *ciliogenesis*. Markedly, ciliated cell differentiation was restored in submerged and hypoxic cells upon treatment with the γ-secretase inhibitor DAPT, which indeed inhibits the Notch signalling [144]. Moreover, it was observed that treatment of standard ALI cultures with the Notch inhibitor DAPT favours the differentiation of basal cells into ciliated cells, producing a significant

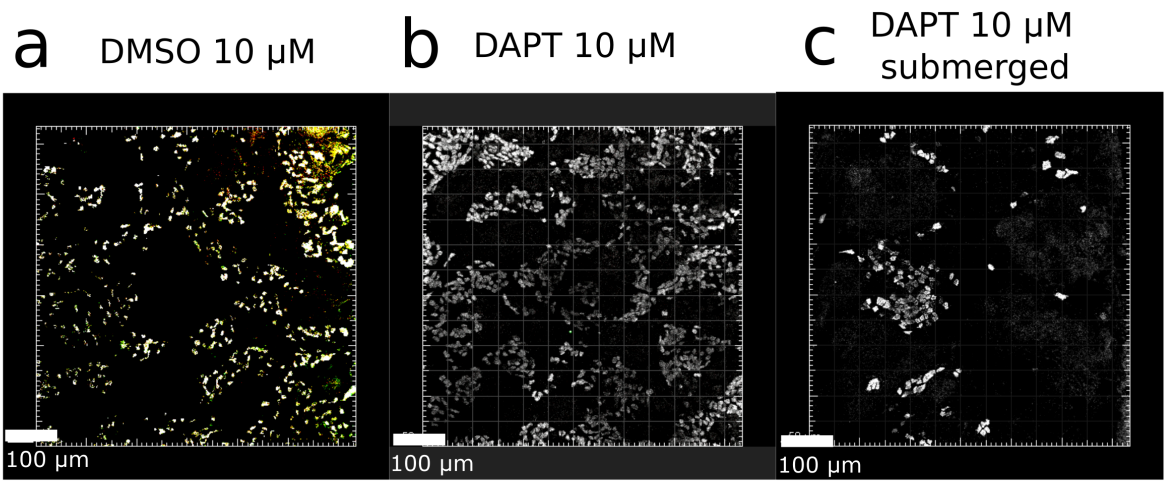

Fig. 5.3 **Treatment with γ-secretase inhibitor of Notch signalling DAPT significantly increases the fraction of multiciliated cells and restores cell differentiation in cultures under submerged conditions.** Cilia of mice airway cells are stained in white (with Acetilated-tubulin). ALI cultures are cultured with 10μM of DMSO (a) and with 10μM of DAPT (b). In (c) we show cells cultured with 10μM of DAPT and left submerged for 15 days. Although DAPT treatment allows differentiation of submerged cultures, the fraction of multiciliated cells in these cultures is lower respect to not-submerged control cultures in (a). Fixation was performed at -20 C °in Methanol.

increase of the fraction of multiciliated cells - up to 2-fold in both mouse and human airway cultures [194]. In our hands, treatment with DAPT markedly increases the number of ciliated cells of mouse and human cultures in Transwell-chips and allows ciliary differentiation in submerged conditions, Figure 5.3.

Airway human nasal cells are grown in Transwell-chips with straight geometry at ALI with already described protocols (Section 2.2.2). Using the setup described in Section 2.4.1 we applied fluid shear stress $\tau \approx 0.2$ dyne/cm^2 for 5 days on cultures at ALI 15 (half *ciliogenesis*) and ALI 35 (complete *ciliogenesis*) by perfusing differentiation medium with the addition of 10μM of DAPT (Sigma, aliquots at 10mM in DMSO stored at -20 C °) to prevent differentiation inhibition driven by hypoxic conditions.

After 5 days of constant shear flow, the Transwell-chips are disassembled from the flow-setup and imaged with and without tracer particles. We acquired BF and FL movies on 20 fields of view (FOVs) respectively for each chip. For each identified ciliated cell i, we measured the CBF and the cilia-driven flow $\vec{v}_i$ in the complete absence of any external flow (see methods in Section 4.2) to be sure that cilia only generate the observed flows. An example of the analysis results for one FOV is shown in Figure 5.4a.

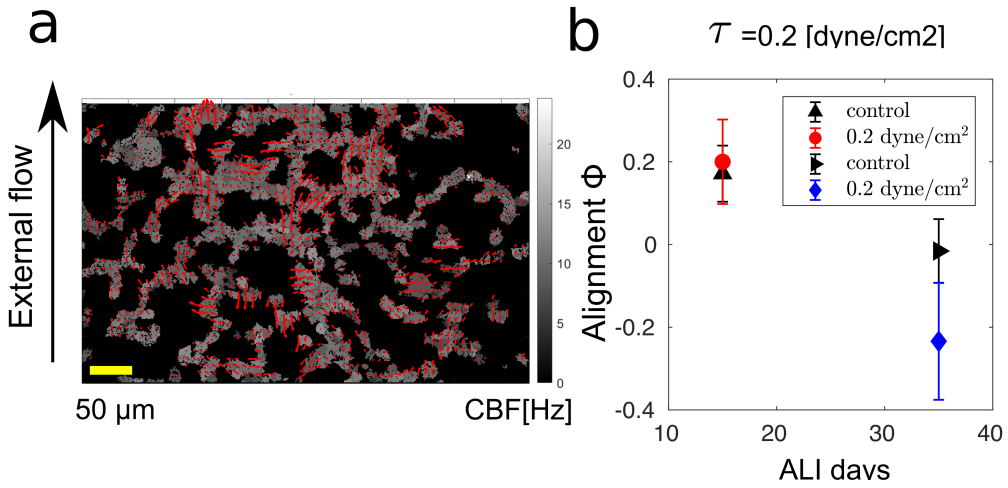

Fig. 5.4 **Human airways nasal cilia do not significantly align with external fluid flows applied at the half or the end of *ciliogenesis*.** (a) After flow treatment, we acquire many BF and FL movies with tracer particles for each culture. Movies are then analysed to extract CBF and cilia beating direction. The greyscale colour-map reports the ciliary beating frequencies (CBF) while the red arrows denote the measured flow field above the identified cells. The length of the arrows is proportional to the flow velocity. (b) Cilia did not align significantly with external flows for both flow treatment at ALI 14 and ALI 35. This result is indicated by the alignment parameter Φ being close to 0 for both control and cells with shear. Error bars are the standard deviation of the average alignment parameter Φ.

Then, we quantified with Φ the global cilia alignment with the external flow, defined in Equation 4.1. Φ is the average over all the projections of cilia beating direction on the direction of the external flow. For $\Phi = 1$, cilia beating directions completely aligned with the applied flow, while $\Phi = 0$ when cilia are randomly oriented. In Figure 5.4b we report the average alignment Φ for the cells treated with shear flows compared with control cultures that were left submerged for the same period of 5 days. We did not find any significant positive alignment in the direction of the external flow respect to controls for both cells at ALI 15 and ALI 35. Differently from the cell treated with air shear stress, Figure 5.2d, here, the cells are still able to generate flow.

5.3 Conclusion and future works

In this chapter, we show a few possible ways to investigate the effect of shear stress on the alignment of airway cilia. We optimised a protocol to apply both controlled air and fluid shear flow on airway cells grown in the microfluidic device Transwell-chip. We found that unidirectional physiological air shear stress during all the period of *ciliogenesis* caused multi-

cilated cells to lose their ability to propel particles. Our hypothesis is that mucus may have been altered by secretory cells in response to shear flow and possibly caused compression of the PCL where cilia beat. At the current stage, this remains just a hypothesis, and it would need further investigation.

On the other hand, we investigate cilia alignment under the effect of unidirectional fluid shear flow. This approach offers two main advantages: (i) mucus is diluted into the bulk fluid. So shear stresses are directly applied on ciliated cells. (ii) Fluid shear flow reassembles the mechanical force happening during early *ciliogenesis in vivo*.
It is well known that airway cultures need to be at air-liquid interface for successful differentiation and that submerged conditions inhibit *ciliogenesis*. To avoid this *in vitro* limitation, we applied shear fluid flow with Notch inhibitor DAPT, that allows ciliogenesis also in submerged cultures. With this setup, our preliminary results suggest that cilia from human nasal cells do *not* align with shear fluid flow applied at the half or the end of *ciliogenesis*. On the other hand, it can not be excluded that higher shear stresses or different treatment time could be relevant for cilia response. It is worth noticing that the cells treated with the fluid shear flow with DAPT differentiated nicely and propelled particles, differently from the culture treated with airflow.

To our knowledge, this is the first time that mechanical forces acting during embryonic days have been investigated in a *in vitro* system as cause for cilia orientation. Previous works only focused on airflow [137], or phasic shear flow after *ciliogenesis* applied for short periods [191]. Future works with this setup can offer valuable insights on whether airway cilia can respond to flow during differentiation as in the case of the ependymal and *Xenopus* ciliated cells [125, 123].

Chapter 6

Conclusions

Motile cilia are widespread across the animal and plant kingdoms, displaying complex collective dynamics central to their physiology. Their coordination mechanism is not generally understood, with previous works mainly focusing on algae and protists. Here we concentrate on the current hypothesis that cilia-driven flow could itself be the mechanical origin of this coordination. I investigated the role of hydrodynamic forces in the synchronisation and the alignment of mammalian cilia in organs such as airways and brain ventricles.

In the first part of my PhD, I developed a novel two-compartment microfluidic chip where airways and brain ciliated differentiate nicely, and external viscous forces can be applied. This device, named Transwell-chip, is composed of a PDMS channel bond to a Corning Transwell insert and offers many advantages over the previous published organ-on-chip devices with similar functions. The geometry of the top compartment permits the inlet and outlet of fluid and airflow, while the bottom compartment is filled with media that feed the above cells without the need to continually perfusing setups. In our hands, we successfully applied constant and oscillatory fluid and airflows on cells for long periods such as days.

Using external oscillatory flow, we studied the synchronisation of cilia beat in multiciliated cells from brain ventricles. The response to controlled oscillatory external flows shows that strong flows at a similar frequency to the actively beating cilia can entrain cilia oscillations. We find that the hydrodynamic forces required for this entrainment strongly depend on the number of cilia per cell. Cells with few cilia (up to five) can be entrained at flows comparable to the cilia-driven flows reported *in vivo*. The experimental trend is quantitatively matched by a model that assumes the group of packed cilia to behave hydrodynamically as an impenetrable rigid rod with an effective radius (that depends on the number of cilia) and each cilium beating driven by an average constant force. Simulations

of hydrodynamically interacting cilia show the same trends observed in experiments. Our results suggest that hydrodynamic forces between cilia are sufficient to be the mechanism behind the synchronisation of brain cilia dynamics.

Then, we investigated the response of motile cilia to constant and unidirectional external flow in the brain and the airways. Cilia in such organs are indeed exposed continuously to shear stresses coming from external sources: fetal and air-breathing in the airways and CSF flow in brain ventricles. Whether these mechanical forces are responsible for the alignment and organisation observed in our body is still unknown. We mainly focused on brain ciliated cells, because they grow submerged in medium, differently from airway cells that grow in air-liquid-interface. We showed that cilia from cultures of mouse ependyma could respond and align to physiological shear stress found *in vivo* also after complete *ciliogenesis*, as opposite as it was believed before [125]. These results suggest that cilia-driven flow networks in the brain could be regulated by hydrodynamic forces between cilia themselves and between external flows at any age. The long-term susceptibility of cilia to external flows is not in contrast with the observed cilia direction switch that reliably and periodically occurs in the brain [39]. Moreover, we measured that more densely ciliated area are less responsive to external shear flow, in agreement with a hydrodynamic screening effect. From this observation, we suggest that density distribution of cilia in the brain could very well play an important role in the establishment of complex flow networks and how they respond to CSF flow.

Finally, we investigated whether airway cells are also responsive to shear stress induced by air and fluid flows. In agreement with other studies [137], our preliminary results show no significant alignment of airways cilia exposed to air or fluid flow in a physiological range (breathing). Future work will tackle this question with additional experiments in this direction.

Overall, my work has brought new insights toward understanding cilia synchronisation and alignment in mammalian tissues. We highlighted for the first time the importance of hydrodynamic screening between dense cilia when responding to external flows, oscillatory or constant. Moreover, our results show that mammalian cilia from the brain are very responsive to flows similar to the one generated by cilia themselves, suggesting that hydrodynamic forces between cilia are important for both their alignment and frequency coordination.

6.1 Open questions and outlooks

Although hydrodynamic forces seem to be sufficient to explain cilia synchronisation in the brain, we do not exclude that elastic and steric interactions between cilia could play an important role. Recent theoretical works reported that more than one mechanism might be important to achieve the observed synchronisation [89, 90], and the question is still an open one. While decoupling these multiple factors is experimentally difficult on mammalian cells, numerical simulations of cilia dynamics could investigate the single contribution of each interaction. For example, simulations of hydrodynamic interacting filaments, where steric interaction (in the form of increasingly stiff repulsions) can be tuned and turned on and off, seem an amendable approach that could be used in the future. Our experiments provide data that could be compared with these simulations. Further experimental investigations are also required to validate these results for other mammalian multiciliated cells. Particularly complex behaviours are expected from cilia propelling mucus, such as in the airways, where cilia beat in a non-Newtonian medium and are also tethered by mucins [43]. Moreover, our approach is based on studying the dynamics of the entire cilium and group of cilia; however, each cilium is composed of thousands of molecular motors. How these molecular motors coordinate to achieve the cilia beating pattern and how these respond to external flow is unknown and may be important to understand the complete picture.

For what concerns cilia alignment, we showed that this can be established with hydrodynamic forces in brain ventricles, while in the airways this is still not clear [137]. In brain cultures, we observed that more densely ciliated areas are less responsive to external shear flows. Further works should aim to elucidate whether this behaviour stems from the hydrodynamic screening of dense cilia. Future works could be running numerical calculations of the hydrodynamic torque on beating cilia at different density in response to external flows. Further studies are needed because hydrodynamic screening effects may have an essential role in all the ciliated organs exposed to fluid flows. For example, airway cells have more dense cilia (100-300 per cell) relative to ependymal cells (20-40 cilia per cell). These differences could have a significant impact on the screening of external flows and could determine the different cilia hydrodynamic response observed in the two organs. Another open question is the interplay of the Planar Cell Polarity pathway and hydrodynamic forces in establishing cilia alignment. In both airways and brain, the role of PCP has also been reported to be very important [125, 10], but this may be the dominating factor in the establishment of cilia orientation in the airways [133]. Nevertheless, PCP pathways itself has been reported to be influenced by mechanical forces [134], so that the hydrodynamics and PCP could play together for the emergence of cilia alignment in a way that depends on the biological system.

Further investigation should focus on PCP polarisation in response to hydrodynamic forces. For example, whether cilia alignment with external flows also induces PCP polarisation in brain cells is not known and need to be tackled by future studies. Overall, the intricate differences between the biological systems involved and the many open questions make the emergence of cilia coordination still a fascinating topic that remains to be investigated.

Appendix A

Toward detection of lung cancer specific biomakers in exhaled breath with Transwell-chip

Lung cancer is one of the most common causes of cancer-related mortality in the world (CRUNK. Cancer mortality statistics at http://www.cancerresearchuk.org/cancer-info/cancerstats/mortality/GoogleScholar). Early detection and the development of novel approaches to the chemoprevention and lung cancer treatments are recent challenges to reducing the mortality of this disease [195]. Markedly, late diagnosis is the major reason for the high fatality of lung cancer [196]. The five-year survival rate after detection varies between 77% in an early stage and 1% in the latest cancer stage.

Breath analysis is a non-invasive diagnostic method that is recently attracting much attention. In the pioneering work of Gordon *et al.* [197] it was observed that there were several volatile organic compounds (VOCs) within the exhaled breath of lung cancer patients that were significantly associated with the disease. After this, the research field grew dramatically, because automatised mass spectroscopy analysis of the exhaled air could be simple enough for reliable detection of cancer biomarkers and potential use as part of a routine pulmonary test in clinics [198].

The group of Frank McCaughan developed an *in vitro* model of bronchial dysplasia that recapitulates key molecular and phenotypic characteristics of human early squamous lung cancer. Specifically, they found that deregulated sex-determining region Y-box 2 (SOX2) expression recreates the molecular and microenvironmental context in which this disease occurs [154, 155]. This *in vitro* system is a perfect candidate for studying the biomarkers

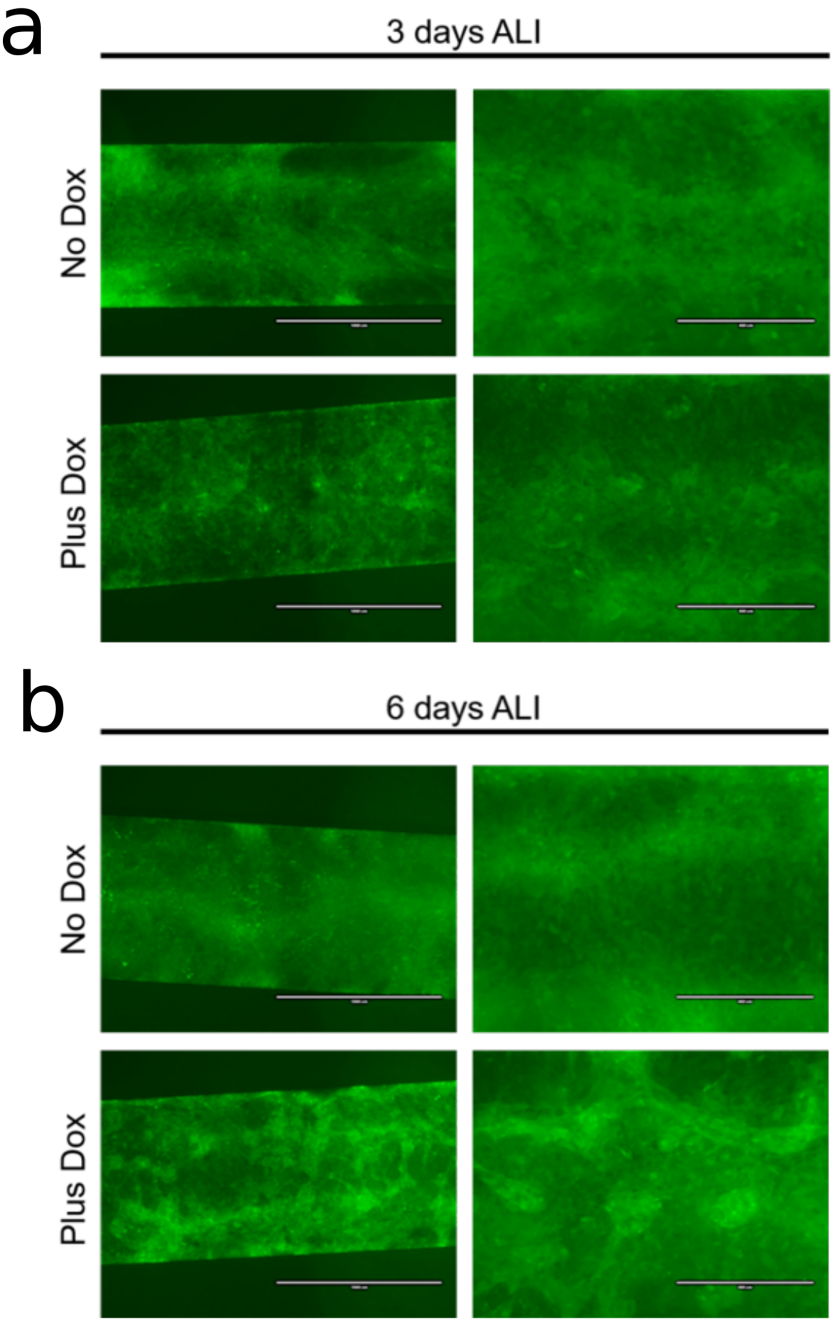

Fig. A.1 **Dysplastic phenotype of human airways in Transwell-chips.** SOX2 deregulation was induced during the establishment of ALI with 0.5μg/ml of doxycycline. Fluorescent images of KTshP53iSOX2 cells with and without doxycycline maintained at air-liquid-interface for 3 days (a) and 6 days (b). Both stages present disorganisation and unnatural outgrowths typical of cancer tissues across the epithelium with SOX2 induction. Scale bars in left GFP images are = 1mm. Scale bars for the right images are = 0.4mm. Images are representative of 3 experimental repeats. Both figures were provided and produced by Phil Barry.

released in the exhaled air by cancer cells during the earlier stages.

In Cambridge, Owlstone Medical company is a world leader in cutting-edge technology able to detect breath volatiles. Owlstone Medical is recently running a study that aims to analyse the breath of 4000 people suspected of having lung cancer. Through miniaturised volatiles collection technology, their goal is to find a "breath signature" that indicates the presence of this disruptive disease (more information at ClinicalTrials.gov identifier NCT02612532).

In collaboration with Owlstone and Frank McCaughan's group, we started testing whether the Transwell-chip could be used to identify useful biomarkers for early squamous lung cancer detection. The top channel of the chip allows airflow to be perfused above the airway cells and then it can be collected and analysed by mass spectroscopy. In the present section, I will describe the preliminary stage of this collaboration, in particular, the efforts to recreate the *in vitro* early cancer model in Transwell-chips.

A.0.1 Deregulation of SOX2 leads to dysplastic phenotype in Transwell-chips.

With the help of Phil Barry, (at that time PhD student with F. McCaughan), we first optimised the growth of KTshP53iSOX2 cells in Transwell-chips, protocols are described in Section 2.2.2. These immortalised human bronchial epithelial cells, named KT cells [156], have been previously engineered to induce deregulation of the SOX2 expression in the presence of a low concentration of doxycycline (2-5 μg/ml) [154]. Moreover, the loss of tumor promoter 53 is a cooperating genetic event that potentates the dysplastic phenotype.

In agreement with [154], we also found in the Transwell-chip that SOX2 deregulation drives the dysplastic phenotype in a confluent epithelial monolayer of KTshP53iSOX2 at the air-liquid interface (ALI). Qualitative changes in phenotype were observed via fluorescent imaging (due to constitutively expressed shP53-GFP construct in KTshP53iSOX2) when SOX2 was induced with 0.5μg/ml of doxycycline, Figure A.1. These changes were characterised at 3 and 6 days from the treatment by disorganisation and expansive outgrowths across the confluent epithelium, similarly observed in previous works [154].

A.0.2 Prospectives

In this work, we reproduced a consistent early lung cancer phenotype in Transwell chips. In collaboration with the Owlstone company, we already started pilot experiments to test

whether this model could be useful for early cancer detection. Humid air can be perfused into Transwell-chips with KTshP53iSOX2 cells SOX2 induced or not. Then the air flowing out the chip can be then collected using Owlstone technology and successively analysed with mass spectrometry for volatiles detection. The description of the setup (flow perfusion and collection) is in Section 2.4.3. Transwell-chip provides a promising model for future studies aimed to identify breath biomarker signatures specific to SOX2 deregulation in early lung cancer.

At the current stage, we are optimising the number of cells per chip in order to have a sensible signal to noise ratio of any interesting volatiles; data are too preliminary to be presented in this thesis. Moreover, the device shown here could be used for novel screening approaches for inhalation chemoprevention therapies for squamous lung cancer.

Appendix B

Supplementary considerations on cilia entrainment with hydrodynamic forces

B.1 Entrainment of a two state oscillator in viscous liquid and the effect of interciliary dissipation

In this section, we briefly review the dynamics of the geometric rower model driven by linear potential and subject to an external periodic force [167]. In this specific case, we can write an analytic expression for the entrainment strength ε that can be used to fit our experimental data.

The oscillation cycle of the rower is prescribed to an amplitude A by a linear driving force F_{dr} applied to the particle that switches in sign at the imposed geometrical boundaries. The internal drive is represented by a discrete variable $\sigma_{dr} = \pm 1$, where the sign is determined at the first passage condition of the particle. We assume the rower as sphere of radius r immersed in a liquid of viscosity η. Then the rower oscillates with constant velocity $v = F_{dr}/\gamma$, where the drag coefficient $\gamma = 6\pi\eta r$. The equation of motion is $\dot{x} = v\sigma_{dr}$, and the frequency of oscillation is $f = F_{dr}/(2\gamma A)$.

On top of this motion an external clock signal imposes a force F_{ex} which is parametrised by $\sigma_c = \pm 1$, and switches accordingly to the imposed external frequency f_{ex}. Therefore the rower particle fells now a force $F = \sigma_{dr}F_{dr} + \sigma_{ex}F_{ex}$, with σ_{dr} and σ_{ex} determined by the geometrical condition and clock frequency.

The equation of motion of this oscillator is now given by:

$$\gamma\dot{x} = \sigma_{dr}F_{dr} + \sigma_{ex}F_{ex}. \tag{B.1}$$

In the absence of noise, entrainment of the rower with the external force can be found when $f_{ex}/f \in [1 - F_{ex}/F_{dr}, 1 + F_{ex}/F_{dr}]$ [167]. This equation has been validated by experiments with colloids driven by optical tweezers. The range of external clock frequency f_{ex} in which entrainment is possible defines the Arnol'd tongue width and the entrainment strength ε:

$$\varepsilon = 2f\frac{F_{ex}}{F_{dr}}. \tag{B.2}$$

This equation can be generalised to the case of a rower with the slender shape of a cylinder and can be used to fit our data for a cilium under external oscillatory flow. In this case, the external force is $F_{ex} = \gamma v_{EX}$, where v_{EX} is the average magnitude velocity of the oscillatory flow. The intrinsic driving force F_{dr} can be derived from the motion of the cilium while isolated from other cilia and external flow.

B.1.1 The effect of intraciliary dissipation on cilia entrainment

In the previous model, we did not account for the intraciliary dissipation that happens during the ciliary beat. To move the cilium, the force applied by the molecular motors has to balance the fluid viscous drag of the moving cilium but also the intracilary friction given by viscoelastic structural elements in the cilium (such as Nexin linkers). Thus $F_{dr} = F^h_{dr} + F^{in}_{dr}$, where F^h_{dr} is the viscous drag of the rower and F^{in}_{dr} the internal friction forces. Evidence of this dissipation is the molecular motors' incomplete chemical energy conversion from ATP into mechanical work [174]. The force exerted by the external flow will be also balanced by the internal friction $F_{EX} = F^h_{EX} + F^{in}_{EX}$. Inspired by previous work [106], we can assume that the intraciliary friction forces F^{in} are in general proportional to the total forces applied F such that $F^{in} = (1 - \eta_c)F$ and $F^h = F\eta_c$, where $\eta_c < 1$ is the efficiency of the chemo-mechanical work energy conversion.

It is worth noting that, if we decrease the efficiency coefficient of the cilium η_c, (more internal friction) the driving force generating cilia motion must be larger to sustain the same frequency oscillation and velocity: $F_{dr} = F^h_{dr} + F^{in}_{dr} = F^h_{dr}/\eta_c$. On the other hand, the forces applied by the external oscillatory flow are $F_{ex} = \gamma v_{EX}$, only ruled by the drag coefficient of the rower. From this simple observation, we can already predict that the ratio between external forces and driving forces will decrease when we decrease η_c. Applying this simple model for the internal friction forces to the geometrical rower, we find that Equation B.2 becomes

$$\varepsilon = 2f\frac{F_{ex}\eta_c}{F_{dr}^h}. \tag{B.3}$$

As expected, this model predicts that the synchronisation strength decreases as the efficiency of the ciliary beat drops, not in contrast with previous works [106, 173]. The fit of this model with the experimental data permits now to estimate the energy efficiency of the ciliary beat η_c.

B.2 Considerations on the role of steric interactions in ciliary beating frequency and entrainment

Motile cilia of ependymal cells beat in a synchronised fashion [39]. The mechanism underpinning cilia synchronisation could involve multiple couplings such as hydrodynamic interactions, basal coupling and also steric interactions between cilia [199]. In this work, we study the dynamics of cilia after synchronisation (or entrainment) is already established.

We measured the ciliary beating frequency (CBF) of isolated cells with a different number of cilia, and we observed that cells with a more significant number of cilia have a higher CBF respect to the one with fewer cilia. We assumed that the observed increase of CBF is only due to hydrodynamic interactions. Here we give a brief justification for such assumption.

Theoretical studies reported that hydrodynamic forces between synchronised cilia could induce an increase of the cilia beating frequency [68, 75, 79]. This phenomenon can be understood in the simple case of two synchronised cilia always moving in the same direction: the hydrodynamic forces between them are both directed in the same direction of movement so that both cilia will move faster than when isolated.

On the other hand, theoretical studies have also investigated the contribution of steric interactions between near cilia (or flagella) [200, 199]. These studies investigated cilia collisions using as steric interaction term a truncated and shifted Lennard-Jones Potential [200, 199]: when two cilia collide, each cilium will experience an exclusive volume force of the same magnitude ($\vec{F}^{st}$) but in opposite directions. While these works reported that steric interactions between cilia could be a mechanism of cilia synchronisation [200, 199], they did not investigate whether steric interactions alone can induce an increase of the average ciliary beating frequency (CBF).

We now show that steric interactions between cilia can not directly induce an increase of CBF in a simple case. Ciliary beating frequency (CBF) is determined by the velocity each cilium moves during its half beating cycle CBF$= v/2A$, where v is the average velocity during half beating cycle, and A is the amplitude. Let's assume a 1D system where two cilia,

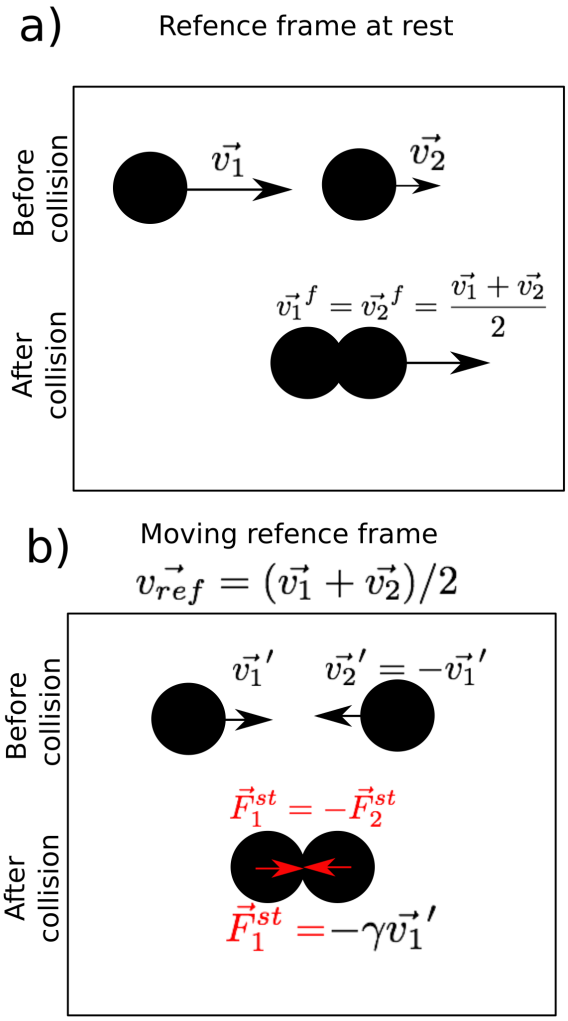

Fig. B.1 Illustration representing cilia steric interaction. We show an example of two cilia (from top view) moving in the same plane and confined to move in 1D. a) In the frame of reference at rest: before collision cilia move with different velocities in the same direction (slower cilium head of the faster cilium); after collision cilia move with the same velocity, that is equal to the average between the initial velocities. b) In the moving frame of reference: before collisions, the two cilia move in the opposite direction with a velocity of equal magnitude. After the collision, the two cilia do not move. The forces driving the initial velocities of the two cilia are balanced by the steric forces $\vec{F}^{st}_{1,2}$.

beating in the same plane, interact sterically. $\vec{v_1}$ and $\vec{v_2}$ represent the velocities respectively of the first and second cilium (during half beating cycle). With these assumptions two cilia can interact sterically when (i) one cilium is slower than the other (with the slower cilium head of the faster) or when (ii) cilia are moving in opposite directions. Both collisions can be treated in the frame of reference moving at velocity $\vec{v}_{ref} = (\vec{v_1} + \vec{v_2})/2$. In this moving frame

of reference, we have that the cilia move with velocity $\vec{v_1}'$ and $\vec{v_2}'$:

$$\vec{v_1}' = \vec{v_1} - \vec{v}_{ref} = (\vec{v_1} - \vec{v_2})/2,$$

$$\vec{v_2}' = \vec{v_2} - \vec{v}_{ref} = -(\vec{v_1} - \vec{v_2})/2.$$

Since $\vec{v_1}' = -\vec{v_2}'$, the two cilia will get closer and closer and eventually collide when their distance is smaller than $2r$, where r is the radius of the cilium. During a collision, the steric (volume exclusion) forces will act to decelerate both cilia up to the point that the two cilia will stop to move (in this frame of reference). The steric forces, and the equilibrium distance between cilia, can be calculated, for example, using a Lennard-Jones Potential [200, 199]. In the low Reynold number regime, null cilia velocity will happen when $\vec{F}_1^{st} = \gamma\vec{v_1'}$, $\vec{F}_2^{st} = -\vec{F}_1^{st} = \gamma\vec{v_2'}$, where γ is the drag coefficient of the cilium and $\vec{F}_1^{st}$ and $\vec{F}_2^{st}$ are the steric forces acting on the first and second cilium, see also Figure B.1. The final velocities of the two cilia are $\vec{v_1^f}' = \vec{v_2^f}' = 0$. Coming back at the original frame of reference at rest, after the collision the two cilia will move at the same velocity $\vec{v_1^f} = \vec{v_2^f} = \vec{v}_{ref}$, that is the average velocity of the two cilia. From this simple example, it is clear that steric interactions can not increase cilia average velocity. By contrast, steric interactions can decrease both cilia velocity (and so average CBF) in the case of cilia moving in the opposite direction. For example, the final velocity is $\vec{v}_{ref} = 0$ for two cilia moving in the opposite direction but with velocities of equal magnitude.

In a more realistic scenario, cilia movement happens in three dimensions. We then expect that cilia can also slip on each other so that the decrease in speed would not be so drastic as we expect from the 1D model for cilia moving in opposite directions. However, it is worth noting that steric forces always act on opposite directions on two colliding cilia (as opposite to hydrodynamic interactions between two cilia moving in the same direction). Thus the final average velocities of the two colliding cilia can never be greater than the initial one, as we showed in this 1D example.

Overall, we can not exclude that steric interactions do not play a role in the emergence of synchronisation, however, we can exclude that steric interactions can explain the observed CBF trend. This argument motivates our assumption that the measured CBF increase in synchronised cilia is only due to hydrodynamic forces.

B.3 Hydrodynamic simulations of cilia bundles

I used the Rotne-Prager method [201, 202] to numerically calculate the hydrodynamic drag coefficients of cilia bundles in bulk. The code was gently provided by Dr S. Bianchi and Prof. R. Di Leonardo [203].

In Rotne-Prager method, rigid bodies are represented as clusters of close-packed small spherical beads. For example, a cilium can be represented by a vertical chain of close-packed beads of radius $r = 0.1$. We indicate the velocities of all these particles with a $6 \times N$ vector $\mathbf{v}_{\text{tot}}$. This vector contains all the translational and rotational velocities of the N beads composing our system. On the other hand, we can define $\mathbf{f}_{\text{tot}}$, the $6 \times N$ vector storing the forces and torques components acting on the beads. The particles interact hydrodynamically through a Rotne-Prager-Yamakawa tensor [204], which takes into account all the hydrodynamic interactions terms up to the $O(r/r_{ij})^3$ in the expansion in the inverse distance between the particles, where r is the beads radius and r_{ij} the distance between the beads i and j. With this approximation, the grand mobility matrix $\mathbf{M}$ can be calculated:

$$\mathbf{v}_{\text{tot}} = \mathbf{M}\mathbf{f}_{\text{tot}} \ . \tag{B.4}$$

For the calculation of the drag coefficient, we assume that the cilia bundle moves as a rigid body. In this situation, it is useful to write all the velocity as a function of the cluster velocity, $\mathbf{v}_c = (v_{cx}, v_{cy}, v_{cz}, \omega_{cx}, \omega_{cy}, \omega_{cz})$ storing the linear and rotational velocity components of the cluster. Successively, we can find the matrix, $\mathbf{C}$, that connects $\mathbf{v}_{\text{tot}}$ with the vector $\mathbf{v}_c$:

$$\mathbf{v}_{\text{tot}} = \mathbf{C}\mathbf{v}_c \ . \tag{B.5}$$

The transpose of $\mathbf{C}$ is the matrix combining all the elements of $\mathbf{f}_{\text{tot}}$ to obtain the vector $\mathbf{f_c} = (f_{cx}, f_{cy}, f_{cz}, T_{cx}, T_{cy}, T_{cz})$, the vector storing the force and torque components of the entire cluster:

$$\mathbf{f}_c = \mathbf{C}^T \mathbf{f}_{\text{tot}}. \tag{B.6}$$

Then, we can combine the Eq. B.4 with the Eq. B.5 and Eq. B.6. In this way, we obtain the following linear relation between $\mathbf{v}_c$ and $\mathbf{f}_c$:

$$\mathbf{f}_c = \mathbf{C}^T \mathbf{M}^{-1} \mathbf{C} \mathbf{v}_c. \tag{B.7}$$

Thus, the drag matrix associated to the rigid cluster of beads is $\mathbf{D}_c = \mathbf{C}^T \mathbf{M}^{-1} \mathbf{C}$.

In these simulations, each cilium is constructed by a vertical rod of length $L = 10\mu$m built up from 0.1 μm radius spheres at a distance of 0.11 μm. A cilia bundle with effective radius r_{eff} is constructed by placing cilia in a square lattice of spacing a, but keeping only the cilia inside a circle of radius r_{eff} (around the origin). This construction method also defines the number of cilia N in a bundle. For representative plots of the cilia bundle construction, see Figure B.2.

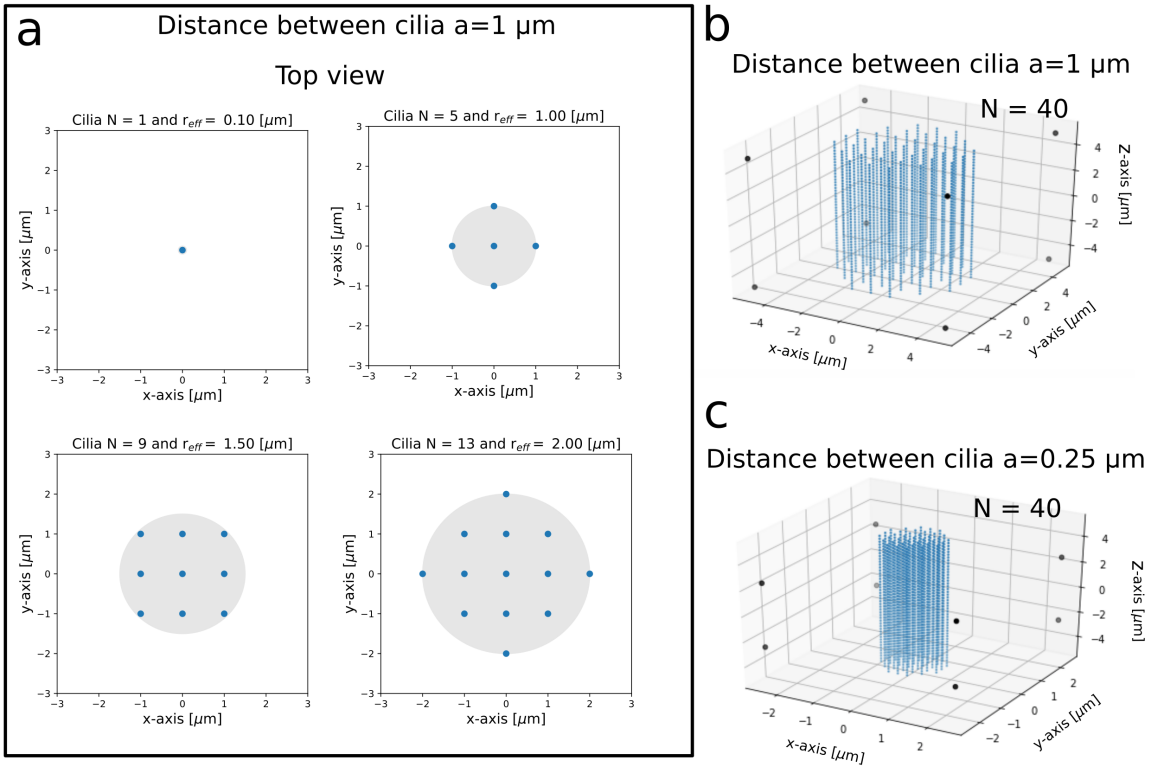

Fig. B.2 Illustration of the cilia bundle construction for the Rotne-Prager simulations. a) Cilia bundle arrangements in a square lattice of spacing $a = 1\mu m$, the area of the circle with effective radius r_{eff} is marked in grey (around the origin). These figures represent the cilia bundle as seen from the top, so that each cilium appears as a point. b) 3-D reconstruction of a cilia bundle with spacing $a = 1\mu m$ (a) and $a = 0.25\mu$m (b). Each cilium is constructed by a rod of length $L = 10\mu$m built up from 0.1 μm radius spheres at a distance of 0.11 μm.

Then, the drag matrix $\mathbf{D}_c(N)$ of the entire cluster of cilia as a function of N is calculated with the Rotne-Prager method. For the aim of my work, I only focused on the drag matrix component associated to the translations of the entire bundle in the directions perpendicular to the axis of the cilia, i.e translations along x and y-direction. This is motivated by the experiments described in Section 3, where external oscillatory flows are applied perpendicular to the cilia axis (parallel to the cell surface). For the symmetry of the bundle construction, the drag matrix coefficients associated to translations along x and y-direction are equal. We

indicate these drag matrix components with $\mathbf{D}_c(\hat{x},\hat{x},N)$.
The average drag coefficient of a cilium (perpendicular to its axis) within the cilia bundle can be obtained by dividing the total drag on the cilia bundle by the number of cilia N:

$$\gamma^{sim}(N) = \mathbf{D}_c(\hat{x},\hat{x},N)/N \tag{B.8}$$

The values obtained from the Rotne-Prager simulations are then compared with the "Impenetrable Effective Rod" model of Section 3. Here, a cluster of cilia is modelled as a single hydrodynamically impenetrable rod. The effective rod has a length L and an effective radius $r_{eff}(N) > r$ that contains all the N cilia from the same cell, [169]. The average drag coefficient of a cilium (i) in the cluster of N is thus:

$$\gamma^{IER}(N) = \frac{1}{N}\frac{4\pi\eta L}{\log\left(L/r_e(N)\right) - 1/2)}. \tag{B.9}$$

Also in this case, the average drag coefficient is respect to translation perpendicular to the cilia axis. Figure B.3 reports the average drag coefficient of a cilium as a function of the number of neighbour cilia N, for cilia spacing $a = 0.25\mu$m and $a = 1\mu m$. The lattice spacing $a = 0.25\mu$m corresponds to the situation where cilia are so densely packed that they are almost in contact. On the other hand, the lattice spacing $a = 1\mu$m corresponds to the one measured experimentally from the centriolar patch areas (see Figure 3.4b-c). These results are compared with the IER model.

In the case of cilia bundle with lattice spacing $a = 0.25\mu$m, the trend with the number of cilia is well-matched by the IER model, Figure B.3b. Here, the cilia are so densely packed that the hydrodynamically impenetrable rod assumption is valid. For a bundle of $N = 21$ cilia, $\gamma^{sim} = 4.31 \times 10^{-8}$ Pa s m, while the IER model predicts $\gamma^{sim} = 5.51 \times 10^{-8}$ Pa s m.

However, in the case of cilia bundle with lattice spacing $a = 1\mu$m, the values from the IER model deviate significantly from the values obtained from the simulations for bundles with a large number of cilia, Figure B.3a. This fact is not surprising since the IER model relies on the slender body assumption, where the effective radius should be $r_{eff} \ll L$, the length of the cilium. Here, the effective radius is $r_{eff} > L/4$ for cilia bundles of $N > 20$, see also insert in Figure B.3a. From the simulations, the average drag coefficient for a cilium in a bundle of $N = 21$ is $\gamma^{sim} = 7.01 \times 10^{-8}$ Pa s m, while the IER model predicts a value that is two times larger $\gamma^{sim} = 1.41 \times 10^{-7}$ Pa s m.

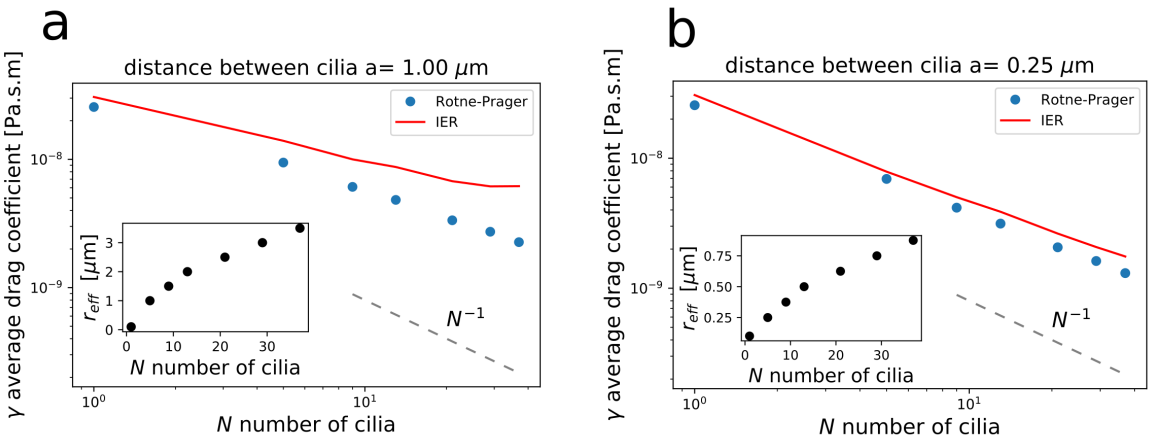

Fig. B.3 The average drag coefficient of a cilium in bundle as a function of the number of cilia N for cilia spacing $a = 1\mu m$ (a) and $a = 0.25\mu$m (b). The drag coefficient is respect to translations perpendicular to the cilium axis The blue dots are the results from the Rotne-Prager simulations, while the solid red line shows the trend of the Impenetrable effective rod (IER) model. The values of effective radius as a function of the number of cilia are reported in the inserts.

References

[1] Peter Satir and Søren T Christensen. Structure and function of mammalian cilia. *Histochemistry and cell biology*, 129(6):687–693, 2008.

[2] Nathalie Spassky and Alice Meunier. The development and functions of multiciliated epithelia. *Nature reviews Molecular cell biology*, 18(7):423, 2017.

[3] Manfred Fliegauf, Thomas Benzing, and Heymut Omran. When cilia go bad: cilia defects and ciliopathies. *Nature reviews Molecular cell biology*, 8(11):880, 2007.

[4] WJ Zhu. Preparation and observation methods can produce misleading artefacts in human sperm ultrastructural morphology. *Andrologia*, 50(7):e13043, 2018.

[5] Don W Fawcett and Keith R Porter. A study of the fine structure of ciliated epithelia. *Journal of Morphology*, 94(2):221–281, 1954.

[6] Denys N Wheatley. Primary cilia in normal and pathological tissues. *Pathobiology*, 63(4):222–238, 1995.

[7] M Delling, A A Indzhykulian, X Liu, Y Li, T Xie, D P Corey, and D E Clapham. Primary cilia are not calcium-responsive mechanosensors. *Nature*, 531(7596):656, 2016.

[8] Shigenori Nonaka, Yosuke Tanaka, Yasushi Okada, Sen Takeda, Akihiro Harada, Yoshimitsu Kanai, Mizuho Kido, and Nobutaka Hirokawa. Randomization of left–right asymmetry due to loss of nodal cilia generating leftward flow of extraembryonic fluid in mice lacking KIF3B motor protein. *Cell*, 95(6):829–837, 1998.

[9] Thomas D Loreng and Elizabeth F Smith. The central apparatus of cilia and eukaryotic flagella. *Cold Spring Harbor perspectives in biology*, 9(2):a028118, 2017.

[10] Eszter K Vladar, Roy D Bayly, Ashvin M Sangoram, Matthew P Scott, and Jeffrey D Axelrod. Microtubules enable the planar cell polarity of airway cilia. *Current Biology*, 22(23):2203–2212, 2012.

[11] Alexia Mahuzier, Asm Shihavuddin, Clémence Fournier, Pauline Lansade, Marion Faucourt, Nikita Menezes, Alice Meunier, Meriem Garfa-Traoré, Marie-France Carlier, Raphael Voituriez, et al. Ependymal cilia beating induces an actin network to protect centrioles against shear stress. *Nature communications*, 9(1):2279, 2018.

[12] E Boisvieux-Ulrich, M C Laine, and D Sandoz. The orientation of ciliary basal bodies in quail oviduct is related to the ciliary beating cycle commencement. *Biology of the Cell*, 55(1-2):147–150, 1985.

[13] Wallace F Marshall and Christopher Kintner. Cilia orientation and the fluid mechanics of development. *Current opinion in cell biology*, 20(1):48–52, 2008.

[14] Mónica Bettencourt-Dias, Friedhelm Hildebrandt, David Pellman, Geoff Woods, and Susana A Godinho. Centrosomes and cilia in human disease. *Trends in Genetics*, 27(8):307–315, 2011.

[15] Pablo Sartori, Veikko F Geyer, Andre Scholich, Frank Jülicher, and Jonathon Howard. Dynamic curvature regulation accounts for the symmetric and asymmetric beats of Chlamydomonas flagella. *Elife*, 5:e13258, 2016.

[16] Peter Satir. How cilia move. *Scientific American*, 231(4):44–54, 1974.

[17] J Blake and A Sleigh. Mechanics of ciliary locomotion. *Biological Review*, 49:85–125, 1974.

[18] E Lauga and T T Powers. The hydrodynamics of swimming microorganisms. *Rep. Prog. Phys.*, 72(0966601), 2009.

[19] Edward M Purcell. Life at low reynolds number. *American journal of physics*, 45(1):3–11, 1977.

[20] Daniela Nicastro, Cindi Schwartz, Jason Pierson, Richard Gaudette, Mary E Porter, and J Richard McIntosh. The molecular architecture of axonemes revealed by cryo-electron tomography. *Science*, 313(5789):944–948, 2006.

[21] Naoki Numata, Takahide Kon, Tomohiro Shima, Kenji Imamula, Toshifumi Mogami, Reiko Ohkura, Keiko Sutoh, and Kazuo Sutoh. Molecular mechanism of force generation by dynein, a molecular motor belonging to the AAA+ family. *Biochemical Society Transactions*, (36):131–135, 2008.

[22] Keith E Summers and I R Gibbons. Adenosine triphosphate-induced sliding of tubules in trypsin-treated flagella of sea-urchin sperm. *Proceedings of the National Academy of Sciences*, 68(12):3092–3096, 1971.

[23] Charles J Brokaw. Direct measurements of sliding between outer doublet microtubules in swimming sperm flagella. *Science*, 243(4898):1593–1596, 1989.

[24] Jianfeng Lin and Daniela Nicastro. Asymmetric distribution and spatial switching of dynein activity generates ciliary motility. *Science*, 360(6387):eaar1968, 2018.

[25] T J Mitchison and H M Mitchison. Cell biology: how cilia beat. *Nature*, 463(7279):308, 2010.

[26] Charles B Lindemann. A" geometric clutch" hypothesis to explain oscillations of the axoneme of cilia and flagella. *Journal of theoretical biology*, 168(2):175–189, 1994.

[27] Ingmar H Riedel-Kruse, Andreas Hilfinger, Jonathon Howard, and Frank Jülicher. How molecular motors shape the flagellar beat. *HFSP journal*, 1(3):192–208, 2007.

[28] Susan S Suarez and A A Pacey. Sperm transport in the female reproductive tract. *Human reproduction update*, 12(1):23–37, 2006.

[29] Marco Polin, Idan Tuval, Knut Drescher, Jerry P Gollub, and Raymond E Goldstein. Chlamydomonas swims with two "gears" in a eukaryotic version of run-and-tumble locomotion. *Science*, 325(5939):487–490, 2009.

[30] Hans Machemer. Ciliary activity and the origin of metachrony in paramecium: effects of increased viscosity. *Journal of Experimental Biology*, 57(1):239–259, 1972.

[31] B A Afzelius. Cilia-related diseases. *The Journal of Pathology: A Journal of the Pathological Society of Great Britain and Ireland*, 204(4):470–477, 2004.

[32] Ann E Tilley, Matthew S Walters, Renat Shaykhiev, and Ronald G Crystal. Cilia dysfunction in lung disease. *Annual review of physiology*, 77:379–406, 2015.

[33] Karl-Ferdinand Lechtreck, Philippe Delmotte, Michael L Robinson, Michael J Sanderson, and George B Witman. Mutations in Hydin impair ciliary motility in mice. *J Cell Biol*, 180(3):633–643, 2008.

[34] S A Halbert, P Y Tam, and R J Blandau. Egg transport in the rabbit oviduct: the roles of cilia and muscle. *Science*, 191(4231):1052–1053, 1976.

[35] Harold G Verhage, Mary L Bareither, Randal C Jaffe, and Maksood Akbar. Cyclic changes in ciliation, secretion and cell height of the oviductal epithelium in women. *American Journal of Anatomy*, 156(4):505–521, 1979.

[36] J T Norwood and Richard G W Anderson. Evidence that adhesive sites on the tips of oviduct cilia membranes are required for ovum pickup in situ. *Biology of reproduction*, 23(4):788–791, 1980.

[37] John V Fahy and Burton F Dickey. Airway mucus function and dysfunction. *New England Journal of Medicine*, 363(23):2233–2247, 2010.

[38] Darryl A Knight and Stephen T Holgate. The airway epithelium: structural and functional properties in health and disease. *Respirology*, 8(4):432–446, 2003.

[39] Regina Faubel, Christian Westendorf, Eberhard Bodenschatz, and Gregor Eichele. Cilia-based flow network in the brain ventricles. *Science*, 353(6295):176–178, 2016.

[40] Elina Toskala, Suzette M Smiley-Jewell, Viviana J Wong, Dustin King, and Charles G Plopper. Temporal and spatial distribution of ciliogenesis in the tracheobronchial airways of mice. *American Journal of Physiology-Lung Cellular and Molecular Physiology*, 289(3):L454–L459, 2005.

[41] Nick Jones. The nose and paranasal sinuses physiology and anatomy. *Advanced drug delivery reviews*, 51(1-3):5–19, 2001.

[42] Daniel T Montoro, Adam L Haber, Moshe Biton, Vladimir Vinarsky, Brian Lin, Susan E Birket, Feng Yuan, Sijia Chen, Hui Min Leung, Jorge Villoria, et al. A revised airway epithelial hierarchy includes cftr-expressing ionocytes. *Nature*, 560(7718):319, 2018.

[43] Brian Button, Li-Heng Cai, Camille Ehre, Mehmet Kesimer, David B Hill, John K Sheehan, Richard C Boucher, and Michael Rubinstein. A periciliary brush promotes the lung health by separating the mucus layer from airway epithelia. *Science*, 337(6097):937–941, 2012.

[44] Michael R Knowles and Richard C Boucher. Mucus clearance as a primary innate defense mechanism for mammalian airways. *The Journal of clinical investigation*, 109(5):571–577, 2002.

[45] Maimoona A Zariwala, Michael R Knowles, and Heymut Omran. Genetic defects in ciliary structure and function. *Annual Review of Physiology*, 69:423–450, 2007.

[46] Peadar G Noone, Margaret W Leigh, Aruna Sannuti, Susan L Minnix, Johnny L Carson, Milan Hazucha, Maimoona A Zariwala, and Michael R Knowles. Primary ciliary dyskinesia: diagnostic and phenotypic features. *American journal of respiratory and critical care medicine*, 169(4):459–467, 2004.

[47] Camille Ehre, Caroline Ridley, and David J Thornton. Cystic fibrosis: an inherited disease affecting mucin-producing organs. *The international journal of biochemistry & cell biology*, 52:136–145, 2014.

[48] Melody P Lun, Edwin S Monuki, and Maria K Lehtinen. Development and functions of the choroid plexus–cerebrospinal fluid system. *Nature Reviews Neuroscience*, 16(8):445, 2015.

[49] Darko Orešković and Marijan Klarica. The formation of cerebrospinal fluid: nearly a hundred years of interpretations and misinterpretations. *Brain research reviews*, 64(2):241–262, 2010.

[50] W Curtis Worthington and Robert S Cathcart. Ciliary currents on ependymal surfaces. *Annals of the New York Academy of Sciences*, 130(3):944–950, 1966.

[51] W Curtis Worthington and Robert S Cathcart. Ependymal cilia: distribution and activity in the adult human brain. *Science*, 139(3551):221–222, 1963.

[52] Marin Bulat and Marijan Klarica. Recent insights into a new hydrodynamics of the cerebrospinal fluid. *Brain research reviews*, 65(2):99–112, 2011.

[53] Bercan Siyahhan, Verena Knobloch, Diane de Zélicourt, Mahdi Asgari, Marianne Schmid Daners, Dimos Poulikakos, and Vartan Kurtcuoglu. Flow induced by ependymal cilia dominates near-wall cerebrospinal fluid dynamics in the lateral ventricles. *Journal of the Royal Society Interface*, 11(94):20131189, 2014.

[54] P Picco, L Leveratto, A Cama, M A Vigliarolo, G L Levato, M Gattorno, E Zammarchi, and M A Donati. Immotile cilia syndrome associated with hydrocephalus and precocious puberty: a case report. *European Journal of Pediatric Surgery*, 3(SUPPL. 1):20–21, 1993.

[55] Marja W Wessels, Nicolette S den Hollander, and Patrick J Willems. Mild fetal cerebral ventriculomegaly as a prenatal sonographic marker for Kartagener syndrome. *Prenatal diagnosis*, 23(3):239–242, 2003.

[56] Y Roth, G L Baum, and R Tadmor. Brain dysfunction in primary ciliary dyskinesia? *Acta neurologica scandinavica*, 78(5):353–357, 1988.

[57] George Paxinos and Keith BJ Franklin. *Paxinos and Franklin's the mouse brain in stereotaxic coordinates*. Academic press, 2019.

[58] Zaman Mirzadeh, Florian T Merkle, Mario Soriano-Navarro, Jose Manuel Garcia-Verdugo, and Arturo Alvarez-Buylla. Neural stem cells confer unique pinwheel architecture to the ventricular surface in neurogenic regions of the adult brain. *Cell stem cell*, 3(3):265–278, 2008.

[59] Kazunobu Sawamoto, Hynek Wichterle, Oscar Gonzalez-Perez, Jeremy A Cholfin, Masayuki Yamada, Nathalie Spassky, Noel S Murcia, Jose Manuel Garcia-Verdugo, Oscar Marin, John L R Rubenstein, Mm Tessier-Lavigne, H Okano, and A Alvarez-Buylla. New neurons follow the flow of cerebrospinal fluid in the adult brain. *Science*, 311(5761):629–632, 2006.

[60] Arkady Pikovsky, Michael Rosenblum, and Jürgen Kurths. *Synchronization: a universal concept in nonlinear sciences*, volume 12. Cambridge university press, 2003.

[61] John Buck and Elisabeth Buck. Synchronous fireflies. *Scientific American*, 234(5):74–85, 1976.

[62] Zoltán Néda, Erzsébet Ravasz, Yves Brechet, Tamás Vicsek, and A-L Barabási. Self-organizing processes: The sound of many hands clapping. *Nature*, 403(6772):849, 2000.

[63] Ido Nitsan, Stavit Drori, Yair E Lewis, Shlomi Cohen, and Shelly Tzlil. Mechanical communication in cardiac cell synchronized beating. *Nature Physics*, 12(5):472, 2016.

[64] Leon Glass. Synchronization and rhythmic processes in physiology. *Nature*, 410(6825):277, 2001.

[65] Greta Quaranta, Marie-Eve Aubin-Tam, and Daniel Tam. Hydrodynamics Versus Intracellular Coupling in the Synchronization of Eukaryotic Flagella. *Physical Review Letters*, 115:238101, 2015.

[66] John R Blake and Michael A Sleigh. Mechanics of ciliary locomotion. *Biological Reviews*, 49(1):85–125, 1974.

[67] E W Knight-Jones. Relations between metachronism and the direction of ciliary beat in Metazoa. *Journal of Cell Science*, 3(32):503–521, 1954.

[68] Jens Elgeti and Gerhard Gompper. Emergence of Metachronal waves in cilia array. *Proceedings of the National Academy of Sciences*, 110(12):4470–4475, 2013.

[69] D R Brumley, M Polin, T J Pedley, and R E Goldstein. Hydrodynamic synchronization and Metachronal waves on the surface of the colonial Alga Volvox Carteri. *Physical Review Letters*, 109(268102), 2012.

[70] Sidney L Tamm, T M Sonneborn, and Ruth V Dippell. The role of cortical orientation in the control of direction of ciliary beat in Paramecium. *Journal of Cell Biology*, 64(1):98–112, 1975.

[71] M J Sanderson and M A Sleigh. Ciliary activity of cultured rabbit tracheal epithelium: beat pattern and metachrony. *Journal of Cell Science*, 47(1):331–347, 1981.

[72] Manuel Ryser, Andy Burn, TH Wessel, Martin Frenz, and J Rička. Functional imaging of mucociliary phenomena. *European Biophysics Journal*, 37(1):35–54, 2007.

[73] Steven J Lieberman, Toshikazu Hamasaki, and Peter Satir. Ultrastructure and motion analysis of permeabilized Paramecium capable of motility and regulation of motility. *Cell motility and the cytoskeleton*, 9(1):73–84, 1988.

[74] Henrique M Oliveira and Luís V Melo. Huygens synchronization of two clocks. *Scientific reports*, 5:11548, 2015.

[75] Shay Gueron and Konstantin Levit-Gurevich. Energetic considerations of ciliary beating and the advantage of metachronal coordination. *Proceedings of the National Academy of Sciences*, 96(22):12240–12245, 1999.

[76] Andreas Schmid and Matthias Salathe. Ciliary beat co-ordination by calcium. 103:159–169, 2011.

[77] Geoffrey Ingram Taylor. Analysis of the swimming of microscopic organisms. *Proceedings of the Royal Society of London.*, 209(1099):447–461, 1951.

[78] Rothschild. Measurement of sperm activity before artificial insemination. *Nature*, 163(4140):358–359, 1949.

[79] Andrej Vilfan and Frank Jülicher. Hydrodynamic flow patterns and synchronization of beating cilia. *Physical review letters*, 96(5):058102, 2006.

[80] Boris Guirao and Jean-François Joanny. Spontaneous creation of macroscopic flow and metachronal waves in an array of cilia. *Biophysical journal*, 92(6):1900–1917, 2007.

[81] Thomas Niedermayer, Bruno Eckhardt, and Peter Lenz. Synchronization, phase locking, and metachronal wave formation in ciliary chains. *Chaos*, 18(3):37128, 2008.

[82] Jurij Kotar, Marco Leoni, Bruno Bassetti, Marco Cosentino Lagomarsino, and Pietro Cicuta. Hydrodynamic synchronization of colloidal oscillators. *Proceedings of the National Academy of Sciences*, 107(17):7669–7673, 2010.

[83] Nicolas Bruot and Pietro Cicuta. Realizing the physics of motile cilia synchronization with driven colloids. *Annual Review of Condensed Matter Physics*, 7:323–348, 2016.

[84] Roberto Di Leonardo, András Búzás, Lóránd Kelemen, Gaszton Vizsnyiczai, László Oroszi, and Pál Ormos. Hydrodynamic synchronization of light driven microrotors. *Physical review letters*, 109(3):34104, 2012.

[85] Douglas R Brumley, Kirsty Y Wan, Marco Polin, and Raymond E Goldstein. Flagellar synchronization through direct hydrodynamic interactions. *eLife*, 3:e02750, 2014.

[86] Douglas R Brumley, Marco Polin, Timothy J Pedley, and Raymond E Goldstein. Metachronal waves in the flagellar beating of Volvox and their hydrodynamic origin. *Journal of the Royal Society Interface*, 12(108):20141358, 2015.

[87] Kirsty Y Wan and Raymond E Goldstein. Coordinated beating of algal flagella is mediated by basal coupling. *Proceedings of the National Academy of Sciences*, 113:2784–2793, 2016.

[88] Kyriacos C Leptos, Kirsty Y Wan, Marco Polin, Idan Tuval, Adriana I Pesci, and Raymond E Goldstein. Antiphase synchronization in a flagellar-dominance mutant of Chlamydomonas. *Physical Review Letters*, 111(15):158101, 2013.

[89] Yujie Liu, Rory Claydon, Marco Polin, and Douglas R Brumley. Transitions in synchronization states of model cilia through basal-connection coupling. *Journal of The Royal Society Interface*, 15(147):20180450, 2018.

[90] Gary S Klindt, Christian Ruloff, Christian Wagner, and Benjamin M Friedrich. In-phase and anti-phase flagellar synchronization by waveform compliance and basal coupling. *New Journal of Physics*, 19(11):113052, 2017.

[91] Natan Osterman and Andrej Vilfan. Finding the ciliary beating pattern with optimal efficiency. *Proceedings of the National Academy of Sciences*, 108(38):15727–15732, 2011.

[92] Bian Qian, Hongyuan Jiang, David A Gagnon, Kenneth S Breuer, and Thomas R Powers. Minimal model for synchronization induced by hydrodynamic interactions. *Physical Review E*, 80(6):61919, 2009.

[93] Jurij Kotar, Luke Debono, Nicolas Bruot, Stuart Box, David Phillips, Stephen Simpson, Simon Hanna, and Pietro Cicuta. Optimal hydrodynamic synchronization of colloidal rotors. *Physical Review Letters*, 111(22):228103, 2013.

[94] Knut Drescher, Nicolas Goldstein Raymond Eand Michel, Marco Polin, and Idan Tuval. Direct measurement of the flow field around swimming microorganisms. *Physical Review Letters*, 105(16):168101, 2010.

[95] Evelyn Hamilton, Nicolas Bruot, and Pietro Cicuta. The chimera state in colloidal phase oscillators with hydrodynamic interaction. *Chaos*, 27(12):123108, 2017.

[96] Evelyn Hamilton and Pietro Cicuta. Interpreting the synchronisation of driven colloidal oscillators via the mean pair interaction. *New Journal of Physics*, 20(9):93028, 2018.

[97] Nariya Uchida and Ramin Golestanian. Generic conditions for hydrodynamic synchronization. *Physical Review Letters*, 106(5):58104, 2011.

[98] M Cosentino Lagomarsino, Patrizia Jona, and B Bassetti. Metachronal waves for deterministic switching two-state oscillators with hydrodynamic interaction. *Physical Review E*, 68(2):21908, 2003.

[99] Christopher Wollin and Holger Stark. Metachronal waves in a chain of rowers with hydrodynamic interactions. *The European Physical Journal E*, 34(4):42, 2011.

[100] Elizabeth H Harris. Chlamydomonas as a model organism. *Annual review of plant biology*, 52(1):363–406, 2001.

[101] Howard C Berg. *Random walks in biology*. Princeton University Press, 1993.

[102] Raymond E Goldstein, Marco Polin, and Idan Tuval. Emergence of synchronized beating during the regrowth of eukaryotic flagella. *Physical Review Letters*, 107(14):148103, 2011.

[103] Veikko F Geyer, Frank Jülicher, Jonathon Howard, and Benjamin M Friedrich. Cell-body rocking is a dominant mechanism for flagellar synchronization in a swimming alga. *Proceedings of the National Academy of Sciences*, 110(45):18058–18063, 2013.

[104] Benjamin M Friedrich and Frank Jülicher. Flagellar synchronization independent of hydrodynamic interactions. *Physical Review Letters*, 109(13):138102, 2012.

[105] Rui Ma, Gary S. Klindt, Ingmar H. Riedel-Kruse, Frank Jülicher, and Benjamin M. Friedrich. Active phase and amplitude fluctuations of flagellar beating. *Physical Review Letters*, 113(4):1–5, 2014.

[106] Gary S Klindt, Christian Ruloff, Christian Wagner, and Benjamin M Friedrich. Load response of the flagellar beat. *Physical review letters*, 117(25):258101, 2016.

[107] Gary S. Klindt, Christian Ruloff, Christian Wagner, and Benjamin M. Friedrich. In-phase and anti-phase flagellar synchronization by waveform compliance and basal coupling. *New Journal of Physics*, 19(11), 2017.

[108] David L Kirk. Volvox. *Current biology*, 14(15):R599–R600, 2004.

[109] Maurizio Chioccioli, Luigi Feriani, Quynh Nguyen, Jurij Kotar, Sharon D Dell, Vito Mennella, Israel Amirav, and Pietro Cicuta. Quantitative high-speed video profiling discriminates between dnah11 and hydin variants of primary ciliary dyskinesia. *American Journal of Respiratory and Critical Care Medicine*, 199(11):1436–1438, 2019.

[110] Michael E Werner, Peter Hwang, Fawn Huisman, Peter Taborek, C Yu Clare, and Brian J Mitchell. Actin and microtubules drive differential aspects of planar cell polarity in multiciliated cells. *Journal of Cell Biology*, 195(1):19–26, 2011.

[111] Supravat Dey, Gladys Massiera, and Estelle Pitard. Role of spatial heterogeneity in the collective dynamics of cilia beating in a minimal one-dimensional model. *Physical Review E*, 97(1):012403, 2018.

[112] Guillermina R Ramirez-San Juan, Arnold J T M Mathijssen, Mu He, Lily Jan, Wallace Marshall, and Manu Prakash. Multi-scale spatial heterogeneity enhances particle clearance in airway ciliary arrays. *bioRxiv*, page 665125, 2019.

[113] Mustapha-Kamel Khelloufi, Etienne Loiseau, Marc Jaeger, Nicolas Molinari, Pascal Chanez, Delphine Gras, and Annie Viallat. Spatiotemporal organization of cilia drives multiscale mucus swirls in model human bronchial epithelium. *Scientific reports*, 8(1):2447, 2018.

[114] Luigi Feriani, Maya Juenet, Cedar J Fowler, Nicolas Bruot, Maurizio Chioccioli, Steven M Holland, Clare E Bryant, and Pietro Cicuta. Assessing the Collective Dynamics of Motile Cilia in Cultures of Human Airway Cells by Multiscale DDM. *Biophysical journal*, 113(1):109–119, 2017.

[115] Jonathan Rutland and Robbert U De Iongh. Random ciliary orientation: a cause of respiratory tract disease. *New England Journal of Medicine*, 323(24):1681–1684, 1990.

[116] Hermes C Grillo. Development of tracheal surgery: a historical review. Part 2: treatment of tracheal diseases. *The Annals of thoracic surgery*, 75(3):1039–1047, 2003.

[117] Paolo Macchiarini, Philipp Jungebluth, Tetsuhiko Go, M Adelaide Asnaghi, Louisa E Rees, Tristan A Cogan, Amanda Dodson, Jaume Martorell, Silvia Bellini, Pier Paolo Parnigotto, and Others. Clinical transplantation of a tissue-engineered airway. *The Lancet*, 372(9655):2023–2030, 2008.

[118] Christiane Knoop and Marc Estenne. Chronic allograft dysfunction. *Clinics in chest medicine*, 32(2):311–326, 2011.

[119] Hirotoshi Matsui, Scott H Randell, Steven W Peretti, C William Davis, and Richard C Boucher. Coordinated clearance of periciliary liquid and mucus from airway surfaces. *The Journal of clinical investigation*, 102(6):1125–1131, 1998.

[120] Biju Thomas, Paul Aurora, Helen Spencer, Martin Elliott, Andrew Rutman, Robert A Hirst, and Christopher O'Callaghan. Persistent disruption of ciliated epithelium following paediatric lung transplantation. *European Respiratory Journal*, 40(5):1245–1252, 2012.

[121] Eszter K Vladar, Dragana Antic, and Jeffrey D Axelrod. Planar cell polarity signaling: the developing cell's compass. *Cold Spring Harbor perspectives in biology*, 1(3):a002964, 2009.

[122] Thomas J Klein and Marek Mlodzik. Planar cell polarization: an emerging model points in the right direction. *Annu. Rev. Cell Dev. Biol.*, 21:155–176, 2005.

[123] Brian Mitchell, Richard Jacobs, Julie Li, Shu Chien, and Chris Kintner. A positive feedback mechanism governs the polarity and motion of motile cilia. *Nature*, 447(7140):97, 2007.

[124] Brian Mitchell, Jennifer L Stubbs, Fawn Huisman, Peter Taborek, Clare Yu, and Chris Kintner. The PCP pathway instructs the planar orientation of ciliated cells in the Xenopus larval skin. *Current biology*, 19(11):924–929, 2009.

[125] Boris Guirao, Alice Meunier, Stéphane Mortaud, Andrea Aguilar, Jean-Marc Corsi, Laetitia Strehl, Yuki Hirota, Angélique Desoeuvre, Camille Boutin, Young-Goo Han, Zaman Mirzadeh, Harold Cremer, Mireille Montcouquiol, Kazunobu Sawamoto, and Nathalie Spassky. Coupling between hydrodynamic forces and planar cell polarity orients mammalian motile cilia. *Nature Cell Biol.*, 12:341–350, 2010.

[126] Paul N Adler. Planar signaling and morphogenesis in Drosophila. *Developmental cell*, 2(5):525–535, 2002.

[127] David I Strutt. Asymmetric localization of frizzled and the establishment of cell polarity in the Drosophila wing. *Molecular cell*, 7(2):367–375, 2001.

[128] Jun Wu and Marek Mlodzik. A quest for the mechanism regulating global planar cell polarity of tissues. *Trends in cell biology*, 19(7):295–305, 2009.

[129] Yanshu Wang and Jeremy Nathans. Tissue/planar cell polarity in vertebrates: new insights and new questions. *Development*, 134(4):647–658, 2007.

[130] Camille Boutin, Paul Labedan, Jordane Dimidschstein, Fabrice Richard, Harold Cremer, Philipp André, Yingzi Yang, Mireille Montcouquiol, Andre M Goffinet, and Fadel Tissir. A dual role for planar cell polarity genes in ciliated cells. *Proceedings of the National Academy of Sciences*, 111(30):E3129–E3138, 2014.

[131] Mitchell T Butler and John B Wallingford. Planar cell polarity in development and disease. *Nature reviews Molecular cell biology*, 18(6):375, 2017.

[132] Danelle Devenport. Tissue morphodynamics: Translating planar polarity cues into polarized cell behaviors. In *Seminars in cell & developmental biology*, volume 55, pages 99–110. Elsevier, 2016.

[133] Moe Matsuo, Atsuko Shimada, Sumito Koshida, Yumiko Saga, and Hiroyuki Takeda. The establishment of rotational polarity in the airway and ependymal cilia: analysis with a novel cilium motility mutant mouse. *American Journal of Physiology-Lung Cellular and Molecular Physiology*, 304(11):L736–L745, 2013.

[134] Yuan-Hung Chien, Ray Keller, Chris Kintner, and David R Shook. Mechanical strain determines the axis of planar polarity in ciliated epithelia. *Current Biology*, 25(21):2774–2784, 2015.

[135] Benoît Aigouy, Reza Farhadifar, Douglas B Staple, Andreas Sagner, Jens-Christian Röper, Frank Jülicher, and Suzanne Eaton. Cell flow reorients the axis of planar polarity in the wing epithelium of drosophila. *Cell*, 142(5):773–786, 2010.

[136] Wen Yih Aw, Bryan W Heck, Bradley Joyce, and Danelle Devenport. Transient tissue-scale deformation coordinates alignment of planar cell polarity junctions in the mammalian skin. *Current Biology*, 26(16):2090–2100, 2016.

[137] Dennis Trieu, Thomas K Waddell, and Alison P McGuigan. A microfluidic device to apply shear stresses to polarizing ciliated airway epithelium using air flow. *Biomicrofluidics*, 8(6):64104, 2014.

[138] Takuya Tsuji, Ryosuke Nakamura, Tatsuya Katsuno, Yo Kishimoto, Atsushi Suehiro, Masaru Yamashita, Ryuji Uozumi, Tatsuo Nakamura, Ichiro Tateya, and Koichi Omori. Long-term preservation of planar cell polarity in reversed tracheal epithelium. *Respiratory research*, 19(1):22, 2018.

[139] Zoran B Redzic, Jane E Preston, John A Duncan, Adam Chodobski, and Joanna Szmydynger-Chodobska. The choroid plexus-cerebrospinal fluid system: from development to aging. *Current topics in developmental biology*, 71:1–52, 2005.

[140] Boyang Zhang, Anastasia Korolj, Benjamin Fook Lun Lai, and Milica Radisic. Advances in organ-on-a-chip engineering. *Nature Reviews Materials*, page 1, 2018.

[141] Dongeun Huh, Benjamin D Matthews, Akiko Mammoto, Martín Montoya-Zavala, Hong Yuan Hsin, and Donald E Ingber. Supporting Online Material for Reconstituting Organ-Level Lung Functions on a Chip Materials and Methods. *Published Science*, 25(328), 2010.

[142] J H-C Wang and B P Thampatty. An introductory review of cell mechanobiology. *Biomechanics and modeling in mechanobiology*, 5(1):1–16, 2006.

[143] CF Dewey, SR Bussolari, MA Gimbrone, and Ps F Davies. The dynamic response of vascular endothelial cells to fluid shear stress. *Journal of biomechanical engineering*, 103(3):177–185, 1981.

[144] Benjamin J Gerovac, Monica Valencia, Nathalie Baumlin, Matthias Salathe, Gregory E Conner, and Nevis L Fregien. Submersion and hypoxia inhibit ciliated cell differentiation in a notch-dependent manner. *American journal of respiratory cell and molecular biology*, 51(4):516–525, 2014.

[145] Katelyn L Sellgren, Elizabeth J Butala, Brian P Gilmour, Scott H Randell, and Sonia Grego. A biomimetic multicellular model of the airways using primary human cells. *Lab on a Chip*, 14(17):3349–3358, 2014.

[146] Dongeun Huh, Hideki Fujioka, Yi-Chung Tung, Nobuyuki Futai, Robert Paine, James B Grotberg, and Shuichi Takayama. Acoustically detectable cellular-level lung injury induced by fluid mechanical stresses in microfluidic airway systems. *Proceedings of the National Academy of Sciences*, 104(48):18886–18891, 2007.

[147] Kambez H Benam, Remi Villenave, Carolina Lucchesi, Antonio Varone, Cedric Hubeau, Hyun-Hee Lee, Stephen E Alves, Michael Salmon, Thomas C Ferrante, James C Weaver, et al. Small airway-on-a-chip enables analysis of human lung inflammation and drug responses in vitro. *Nature methods*, 13(2):151, 2016.

[148] Kambez H Benam, Remi Villenave, Carolina Lucchesi, Antonio Varone, Cedric Hubeau, Hyun-Hee Lee, Stephen E Alves, Michael Salmon, Thomas C Ferrante, James C Weaver, A Bahinski, G A Hamilton, and D E Ingber. Small airway-on-a-chip enables analysis of human lung inflammation and drug responses in vitro. *Nature methods*, 13(2):151, 2015.

[149] Anna Tourovskaia, Xavier Figueroa-Masot, and Albert Folch. Differentiation-on-a-chip: a microfluidic platform for long-term cell culture studies. *Lab Chip*, 5(1):14–19, 2005.

[150] Bor-han Chueh, Dongeun Huh, Christina R Kyrtsos, Timothée Houssin, Nobuyuki Futai, and Shuichi Takayama. Leakage-free bonding of porous membranes into layered microfluidic array systems. *Analytical chemistry*, 79(9):3504–3508, 2007.

[151] Nathalie Delgehyr, Alice Meunier, Marion Faucourt, Montserrat Bosch Grau, Laetitia Strehl, Carsten Janke, and Nathalie Spassky. Ependymal cell differentiation, from monociliated to multiciliated cells. In *Methods in Cell Biology*, volume 127, pages 19–35. Elsevier, 2015.

[152] Hongmei Mou, Vladimir Vinarsky, Purushothama Rao Tata, Karissa Brazauskas, Soon H Choi, Adrianne K Crooke, Bing Zhang, George M Solomon, Brett Turner, Hermann Bihler, et al. Dual smad signaling inhibition enables long-term expansion of diverse epithelial basal cells. *Cell stem cell*, 19(2):217–231, 2016.

[153] Philip H Karp, Thomas O Moninger, S Pary Weber, Tamara S Nesselhauf, Janice L Launspach, Joseph Zabner, and Michael J Welsh. An in vitro model of differentiated human airway epithelia. In *Epithelial cell culture protocols*, pages 115–137. Springer, 2002.

[154] Lucia L Correia, Jo-Anne Johnson, Peter McErlean, Julien Bauer, Hassan Farah, Doris M Rassl, Robert C Rintoul, Tariq Sethi, Paul Lavender, Emma L Rawlins, et al. Sox2 drives bronchial dysplasia in a novel organotypic model of early human squamous lung cancer. *American journal of respiratory and critical care medicine*, 195(11):1494–1508, 2017.

[155] Kyren A Lazarus, Fazal Hadi, Elisabetta Zambon, Karsten Bach, Maria-Francesca Santolla, Julie K Watson, Lucia L Correia, Madhumita Das, Rosemary Ugur, Sara Pensa, et al. Bcl11a interacts with sox2 to control the expression of epigenetic regulators in lung squamous carcinoma. *Nature communications*, 9(1):3327, 2018.

[156] Ruben D Ramirez, Shelley Sheridan, Luc Girard, Mitsuo Sato, Young Kim, Jon Pollack, Michael Peyton, Ying Zou, Jonathan M Kurie, J Michael DiMaio, et al. Immortalization of human bronchial epithelial cells in the absence of viral oncoproteins. *Cancer research*, 64(24):9027–9034, 2004.

[157] Deborah Huber, Ali Oskooei, Xavier Casadevall i Solvas, Andrew Demello, and Govind V Kaigala. Hydrodynamics in cell studies. *Chemical reviews*, 118(4):2042–2079, 2018.

[158] Cx K Batchelor and GK Batchelor. *An introduction to fluid dynamics*. Cambridge university press, 2000.

[159] Frank M White and Isla Corfield. *Viscous fluid flow*, volume 3. McGraw-Hill New York, 2006.

[160] Henrik Bruus. *Theoretical microfluidics*, volume 18. Oxford university press Oxford, 2008.

[161] Lily Kim, Yi-Chin Toh, Joel Voldman, and Hanry Yu. A practical guide to microfluidic perfusion culture of adherent mammalian cells. *Lab Chip*, 7(6):681–694, 2007.

[162] Francis Patton Bretherton. The motion of long bubbles in tubes. *Journal of Fluid Mechanics*, 10(2):166–188, 1961.

[163] K Mukundakrishnan, PS Ayyaswamy, and DM Eckmann. Bubble motion in a blood vessel: shear stress induced endothelial cell injury. *Journal of biomechanical engineering*, 131(7):074516, 2009.

[164] Mojca Vilfan, Gašper Kokot, Andrej Vilfan, Natan Osterman, Blaž Kav, Igor Poberaj, and Dušan Babi. Analysis of fluid flow around a beating artificial cilium. pages 163–171, 2012.

[165] Joseph H Sisson, J A Stoner, B A Ammons, and T A Wyatt. All-digital image capture and whole-field analysis of ciliary beat frequency. *Journal of Microscopy*, 211(2):103–111, 2003.

[166] Svetlana Dimova, Frederik Maes, Marcus E Brewster, Mark Jorissen, Mark Noppe, and Patrick Augustijns. High-speed digital imaging method for ciliary beat frequency measurement. *Journal of Pharmacy and Pharmacology*, 57(4):521–526, 2005.

[167] Nicolas Bruot, Loïc Damet, Jurij Kotar, Pietro Cicuta, and Marco Cosentino Lagomarsino. Noise and synchronization of a single active colloid. *Physical Review Letters*, 107(9):094101, 2011.

[168] Eric Lauga and Thomas R Powers. The hydrodynamics of swimming microorganisms. *Reports on Progress in Physics*, 72(9):096601, 2009.

[169] C Allain and M Cloitre. The effects of gravity on the aggregation and the gelation of colloids. *Advances in colloid and interface science*, 46:129–138, 1993.

[170] Holden Higginbotham, Stephanie Bielas, Teruyuki Tanaka, and Joseph G Gleeson. Transgenic mouse line with green-fluorescent protein-labeled centrin 2 allows visualization of the centrosome in living cells. *Transgenic research*, 13(2):155–164, 2004.

[171] Alan J Hunt, Frederick Gittes, and Jonathon Howard. The force exerted by a single kinesin molecule against a viscous load. *Biophysical journal*, 67(2):766–781, 1994.

[172] Nicolas Bruot and Pietro Cicuta. Emergence of polar order and cooperativity in hydrodynamically coupled model cilia. *Journal of The Royal Society Interface*, 10(87):20130571, 2013.

[173] Benjamin M Friedrich. Load response of shape-changing microswimmers scales with their swimming efficiency. *Physical Review E*, 97(4):042416, 2018.

[174] C. J. Brokaw. Adenosine triphosphate usage by flagella. *Science*, 156(3771):76–78, 1967.

[175] Shang Yik Reigh, Roland G Winkler, and Gerhard Gompper. Synchronization and bundling of anchored bacterial flagella. *Soft Matter*, 8(16):4363–4372, 2012.

[176] Yuriko Sassa, Shuhei Shibata, Yasutaka Iwashita, and Yasuyuki Kimura. Hydrodynamically induced rhythmic motion of optically driven colloidal particles on a ring. *Phys. Rev. E*, 85:061402, Jun 2012.

[177] Evelyn Alexandra Waterhouse Hamilton. *Controlling the collective dynamics in systems of active oscillators through geometry and hydrodynamic entrainment*. PhD thesis, Department of Physics University of Cambridge, April 2019.

[178] Anthony J Kim, Vinothan N Manoharan, and John C Crocker. Swelling-based method for preparing stable, functionalized polymer colloids. *Journal of the American Chemical Society*, 127(6):1592–1593, 2005.

[179] William Thielicke and Eize Stamhuis. PIVlab–towards user-friendly, affordable and accurate digital particle image velocimetry in MATLAB. *Journal of Open Research Software*, 2(1), 2014.

[180] Massimiliano Rossi, Ralph Lindken, Beerend P Hierck, and Jerry Westerweel. Tapered microfluidic chip for the study of biochemical and mechanical response at subcellular level of endothelial cells to shear flow. *Lab on a Chip*, 9(10):1403–1411, 2009.

[181] M Rautiainen, Y Collan, J Nuutinen, and B A Afzelius. Ciliary orientation in the immotile cilia syndrome. *European Archives of Oto-Rhino-Laryngology*, 247(2):100–103, 1990.

[182] Andrea Cavagna, Alessio Cimarelli, Irene Giardina, Giorgio Parisi, Raffaele Santagati, Fabio Stefanini, and Massimiliano Viale. Scale-free correlations in starling flocks. *Proceedings of the National Academy of Sciences*, 107(26):11865–11870, 2010.

[183] Roberto Cerbino and Veronique Trappe. Differential dynamic microscopy: Probing wave vector dependent dynamics with a microscope. *Physical Review Letters*, 2008.

[184] Roberto Cerbino and Pietro Cicuta. Perspective : Differential dynamic microscopy extracts multi-scale activity in complex fluids and biological systems Perspective : Differential dynamic microscopy extracts multi-scale activity in complex fluids and biological systems. *The Journal of chemical physics*, 147(11):110901, 2017.

[185] Larisa Gheber, Alon Korngreen, and Zvi Priel. Effect of viscosity on metachrony in mucus propelling cilia. *Cell motility and the cytoskeleton*, 39(1):9–20, 1998.

[186] Larisa Gheber and Zvi Priel. On metachronism in ciliary systems: a model describing the dependence of the metachronal wave properties on the intrinsic ciliary parameters. *Cell motility and the cytoskeleton*, 16(3):167–181, 1990.

[187] R Cerbino, L Peverini, M A C Potenza, A Robert, P Osecke, Giglio, and M. X-ray-scattering information obtained from near-field speckle. 2008.

[188] Richard JB Francis, Bishwanath Chatterjee, Niki T Loges, Hanswalter Zentgraf, Heymut Omran, and Cecilia W Lo. Initiation and maturation of cilia-generated flow in newborn and postnatal mouse airway. *American Journal of Physiology-Lung Cellular and Molecular Physiology*, 296(6):L1067–L1075, 2009.

[189] Mingyao Liu and Martin Post. Invited review: mechanochemical signal transduction in the fetal lung. *Journal of Applied physiology*, 89(5):2078–2084, 2000.

[190] Guohua Xia, Merryn H Tawhai, Eric A Hoffman, and Ching-Long Lin. Airway wall stiffening increases peak wall shear stress: a fluid–structure interaction study in rigid and compliant airways. *Annals of biomedical engineering*, 38(5):1836–1853, 2010.

[191] Brian Button, Richard C Boucher, University of North Carolina Virtual Lung Group, et al. Role of mechanical stress in regulating airway surface hydration and mucus clearance rates. *Respiratory physiology & neurobiology*, 163(1-3):189–201, 2008.

[192] Robert Tarran, Brian Button, Maryse Picher, Anthony M Paradiso, Carla M Ribeiro, Eduardo R Lazarowski, Liqun Zhang, Peter L Collins, Raymond J Pickles, Jeffrey J Fredberg, et al. Normal and cystic fibrosis airway surface liquid homeostasis the effects of phasic shear stress and viral infections. *Journal of Biological Chemistry*, 280(42):35751–35759, 2005.

[193] Nurit Even-Tzur, Yoel Kloog, Michael Wolf, and David Elad. Mucus secretion and cytoskeletal modifications in cultured nasal epithelial cells exposed to wall shear stresses. *Biophysical journal*, 95(6):2998–3008, 2008.

[194] Eszter K Vladar, Jayakar V Nayak, Carlos E Milla, and Jeffrey D Axelrod. Airway epithelial homeostasis and planar cell polarity signaling depend on multiciliated cell differentiation. *JCI insight*, 1(13), 2016.

[195] Robert L Keith and York E Miller. Lung cancer chemoprevention: current status and future prospects. *Nature reviews Clinical oncology*, 10(6):334, 2013.

[196] Ramon Rami-Porta, John J Crowley, and Peter Goldstraw. Review the revised tnm staging system for lung cancer. *Ann Thorac Cardiovasc Surg*, 15(1):5, 2009.

[197] SM Gordon, JP Szidon, BK Krotoszynski, RD Gibbons, and HJ O'Neill. Volatile organic compounds in exhaled air from patients with lung cancer. *Clinical chemistry*, 31(8):1278–1282, 1985.

[198] Yannick Saalberg and Marcus Wolff. Voc breath biomarkers in lung cancer. *Clinica Chimica Acta*, 459:5–9, 2016.

[199] Yingzi Yang, Vincent Marceau, and Gerhard Gompper. Swarm behavior of self-propelled rods and swimming flagella. *Physical Review E*, 82(3):031904, 2010.

[200] Shang Yik Reigh, Roland G Winkler, and Gerhard Gompper. Synchronization, slippage, and unbundling of driven helical flagella. *PloS one*, 8(8):e70868, 2013.

[201] Christian Holm and Kurt Kremer. *Advanced computer simulation approaches for soft matter sciences III*, volume 221. Springer, 2008.

[202] Michael Reichert. *Hydrodynamic Interactions in Colloidal and Biological Systems*. PhD thesis, Universitat Konstanz, Konstanz, 2006.

[203] Silvio Bianchi, Gaszton Vizsnyiczai, Stefano Ferretti, Claudio Maggi, and Roberto Di Leonardo. An optical reaction micro-turbine. *Nature communications*, 9(1):1–6, 2018.

[204] Jens Rotne and Stephen Prager. Variational treatment of hydrodynamic interaction in polymers. *The Journal of Chemical Physics*, 50(11):4831–4837, 1969.